TECHNISCHE UNIVERSITÄT MÜNCHEN

PHYSIK-DEPARTMENT E17

Investigation of the Cu^{2+} Binding Site of Full-Length Human Prion Protein

Pablo del Pino González de la Higuera

Vollständiger Abdruck der von der Fakultät für Physik der Technischen Universität München zur Erlangung des akademischen Grades eines

Doktors der Naturwissenschaften

genehmigten Dissertation.

Vorsitzender: Univ.-Prof. Dr. P. Vogl

Prüfer der Dissertation:

    1.   Univ.-Prof. Dr. F. G. Parak, i.R.

    2.   Univ.-Prof. Dr. J. Friedrich

Die Dissertation wurde am 12.02.2007 bei der Technischen Universität München eingereicht und durch die Fakultät für Physik am 13.03.2007 angenommen.

Dedicado a mi padre, espejo donde intento reconocerme todos los días.

Table of contents

Zusammenfassung

Transmissible spongiforme Enzephalopathien (TSE) sind neurodegenerative Krankheiten in Säugetieren, die durch einen infektiösen Erreger mit dem Namen Prion verursacht werden. Im Gegensatz zu anderen infektiösen Erregern bestehen, Prionen nur aus Protein, der krankheits-assoziierten Isoform PrP^{Sc} des zellulären Prionen-Proteins PrP^C. Die biologische Relevanz der Bindung von Cu^{2+} an PrP^C gilt mittlerweile als gesichert. PrP^C kann bis zu vier Cu^{2+} Ionen mit hoher Affinität in seiner so genannten "octarepeat" Region binden, die aus vier Wiederholungen der Sequenz PHGGGWGQ besteht. Die vererbbare Erhöhung der Anzahl dieser "octarepeat" Wiederholungen in mutierten Formen des Proteins konnte mit gehäuftem Auftreten von TSE in einigen Familien in Verbindung gebracht werden. Die "octarepeat" Region des Proteins spielen daher eine wichtige Rolle in TSE. Neben der Bindung von Cu^{2+} an Bindungsstellen der "octarepeat" Region gibt es auch Vermutungen über die Existenz einer oder zweier weiterer Bindungsstellen für Cu^{2+} Ionen in dem unstrukturierten Bereich zwischen der "octarepeat" Domäne und dem strukturierten C-Terminus von PrP^C.

Das Hauptziel dieser Arbeit ist die Bestimmung der Struktur der Bindungsstellen für Cu^{2+} Ionen des rekombinanten menschlichen Proteins PrP(23–231) in voller Länge. Zum Vergleich wurden einzelne Peptidsequenzen aus PrP in verschiedenen Umgebungen untersucht, unter anderem die "octarepeat" Domäne und rekombinantes PrP(23–231) mit der Punkt mutation H→G aus Mäusen in voller Länge. Dazu wurden spektroskopische Daten mit Electron Paramagnetic Resonance (EPR), Electron Nuclear Double Resonance (ENDOR), und Extended X-ray Absorption Fine Spectroscopy (EXAFS) aufgenommen. Mit Moleculardynamik (MD) Simulationen wurden sterisch mögliche Strukturen ausgewählt.

Es wurden drei klar unterscheidbare Peptid/Cu^{2+} Konfigurationen nachgewiesen, die im Folgenden als Spezies I, II und III bezeichnet werden. Die experimentell an

rekombinanten hPrP(23–231) aufgenommenen Daten sind konsistent mit dem Vorhandensein essentiell eines Cu^{2+} Konfigurations-Typs, Spezies II. Zusammen mit den spektroskopischen Daten und den MD Simulationen wurde ein zuverlässiges Model für den Kupfer-Bindungsplatz in der "octarepeat" Domäne von PrP entwickelt. Für eine Stöchiometrie von zwei "octarepeats" pro Cu^{2+} Ion besteht das resultierende kupferbindende Zentrum aus einer vierfachen rechtecksförmigen ebenen Stickstoff-Koordination. Zwei Stickstoffe gehören dabei zu den Imidazol-Ringen von Histidin-Resten. Weitere Liganden sind zwei deprotonierte Stickstoffe aus dem Amid-Rückgrat von benachbarten Glyzin Resten, und ein axiales Sauerstoff-Atom eines Wassermoleküls. Dieses Modell für die Kupferbindung an PrP unterscheidet sich in signifikanter Weise von früher vorgeschlagenen Modellen die an von PrP abgeleiteten Peptiden erzeugt wurden. Es ist hierbei zu betonen, dass sich das vorgeschlagene Model auf die Kupferbindung an PrP unter physiologischem pH (6.0 oder 7.0) unter nicht saturierender Kupfer-Konzentration bezieht. Aufgrund der relativ geringen Cu^{2+} Konzentration in extrazellulärer Umgebung scheint das hier vorgeschlagenes Modell für die Kupfer-Bindungsstelle durchaus die *in vivo* Realität zu beschreiben.

Die von Maus abstammende Mutante mPrP Cu^{2+} bindet in der Form von Spezies III, wohingegen unter einigen Bedingungen in von PrP abgeleiteten Peptides ein Gleichgewicht zwischen Molekülen vorliegt, die den Spezies I und II zugeordnet werden können. Dieses Gleichgewicht hängt sehr stark von der Beladung mit Cu^{2+}, dem pH Wert und dem Puffersystem ab.

Abstract

Transmissible spongiform encephalopathies (TSEs) in mammals are neurodegenerative diseases caused by an infectious agent called prion. In contrast to other known infectious agents, prions seem to consist solely of protein, the disease-related isoform PrP^{Sc} of the cellular prion protein PrP^C. The biological relevance of Cu^{2+} binding to PrP^C is nowadays certain. PrP^C can bind up to four Cu^{2+} ions with high affinity in the octarepeat region, which consists of four tandem repeat of the sequence PHGGGWGQ. Inherited amplification of the number of octapeptide repeats in mutant forms has been linked to several familial cases of human TSEs. The octarepeat region has been proven to play an important role in TSEs. In addition to the octarepeat Cu^{2+} sites, coordination of one or two additional Cu^{2+} ions has been contemplated in the unstructured region between the octarepeat domain and the structured C-terminal part of PrP^C.

The main goal of this work is the structure determination of the Cu^{2+} binding sites of recombinant full-length human PrP(23–231). For comparison, various PrP-derived peptides spanning residues from the octarepeat domain and a mutant form of recombinant full-length murine PrP(23–231) were investigated in different environments. The spectroscopic data were collected by means of electron paramagnetic resonance (EPR), electron nuclear double resonance (ENDOR), and extended X-ray absorption fine spectroscopy (EXAFS). Molecular Dynamics (MD) calculations were used to select sterically possible structures.

The presence of three clearly distinguishable peptide/Cu^{2+} configurations, referred to as species I, II, and III, were found. The experimental data of the recombinant hPrP(23–231) are consistent with the presence of essentially a Cu^{2+} configuration type, species II. Using the spectroscopic results together with MD calculations a reliable model for the copper binding place of the octarepeat domain of PrP is presented. For a stoichiometry of two octarepeats per Cu^{2+} ion, the resulting Cu^{2+}-

binding motif consists of a square planar four nitrogen coordination. Two nitrogens belong to imidazole rings of histidine residues. Further ligands are two deprotonated backbone amide nitrogens of the adjacent glycine residues and an axial oxygen of a water molecule. This model of copper binding to PrP differs significantly from those previously obtained in the context of PrP-derived peptides. It must be stressed that we proposed a model of copper binding to PrP at physiological pH (6.0 or 7.0) with non-saturated copper concentration. Indeed, due to the low availability of Cu^{2+} in the extracellular environment, this novel Cu^{2+} binding arrangement might be more likely to exist *in vivo*.

On the other hand, the mutant form of murine PrP binds Cu^{2+} as species III whereas in PrP-derived peptides, an equilibrium of molecules belonging to species I and II is present at several conditions. This equilibrium strongly depends upon the Cu^{2+} load, pH value and buffer system.

Symbols and Abbreviations

Abbreviations

BSE	Bovine Spongiform Encephalopathy
CJD	Creutzfeldt-Jakob Disease
CNS	Central Nervous System
CW	Continuous Wave
CWD	Chronic Wasting Disease
ENDOR	Electron Nuclear Double Resonance
EPR	Electron Paramagnetic Resonance
ESEEM	Electron Spin Echo Envelope Modulation
EXAFS	Extended X-ray Absorption Fine Structure
fCJD	Familial Creutzfeldt-Jakob Disease
FFI	Fatal Familiar Insomnia
GSS	Gerstmann-Sträussler-Scheinker Disease
Gly	Glycine
His	Histidin
iCJD	Iatrogenic Creutzfeldt-Jakob Disease
NMR	Nuclear Magnetic resoncance
MBM	Meat and Bone Meal
MD	Molecular Dynamics
MES	2-morpholinoethanesulfonic acid
MM	Molecular Mechanics
MOPS	3-N-morpholinopropanesulfonic acid
NEM	N-ethylmorpholin
nvCJD	New variant Creutzfeldt-Jakob Disease
Prpm	Prion protein gene
PrP27–30	Protease-resistant core of PrP^{Sc}
PrP	Prion protein
PrP^c	Cellular prion protein
PrP^{sc}	Scrapie prion protein
sCJD	Sporadic Creutzfeldt-Jakob Disease
Trp	Tryptophan
TSE	Transmissible Spongiform Encephalopathy
TME	Transmissible Mink Encephalopathy

Symbols

$\vec{\vec{A}}_{HF}$	Nuclear hyperfine coupling tensor
$\vec{\vec{A}}_{SHF}$	Nuclear superhyperfine coupling tensor
A_{eff}	Effective hyperfine coupling factor
A_o	Isotropic hyperfine coupling factor
$\vec{B}_o$	External magnetic field
$\vec{\varepsilon}$	Polarization vector of the electron field
$\left\| f_j(k) \right\| \cdot e^{i\phi_j(k)}$	Backscattering amplitude
δ_{ij}	Kronecker symbol
$\vec{\vec{g}}$	g tensor of the electron spin
g_{eff}	Effective g factor
g_N	g factor of the nuclear spin
g_{xx}, g_{yy}, g_{zz}	Components of the g tensor
h	Planck´s constant
$\vec{\vec{H}}_S$	Spin Hamiltonian (Operator)
$\vec{\vec{H}}_{HF,i}$	Nuclear Hypefine Hamiltonian of a nucleus i
$\vec{\vec{H}}_{Q,i}$	Nuclear Quadrupole Hamiltonian of a nucleus i
$\vec{\vec{H}}_{NZ,i}$	Nuclear Zeeman Hamiltonian of a nucleus i
θ_i	Angle between g_z and $\vec{r}$ (see Figure. 2.7)
θ	Angle between g_z and $\vec{B}_o$ (see Figure 2.7)
φ_i	Angle between g_x and xy-projected $\vec{r}$ (see Figure 2.7)
φ	Angle between g_x and xy-projected $\vec{B}_o$ (see Figure 2.7)
$\vec{\vec{I}}$	Nuclear spin operator
$\vec{\vec{I}}$	z-component of the nuclear spin operator
$\vec{\vec{I}}_+, \vec{\vec{I}}_-$	Ladder operators
k_B	Boltzmann factor
μ_B	Bohr´s magneton
μ_N	Nuclear magneton
m_I	Nuclear magnetic quantum number
m_s	Electron magnetic quantum number
N_j	Coordination number, Eq.(2.32)
ν_0	Larmor frequency
R_j	Average coordination distance, Eq.(2.32)

$\vec{r}$	Vector which defines the position of a nucleus i (Figure 2.7)
$\vec{\vec{S}}$	Electron spin operator
$\vec{\vec{S}}_z$	z-component of the electron spin operator
S_o^2	Empirical parameter, many body losses in the photo-absorption processes
σ_j^2	Mean square relative displacement, Eq.(2.32)
δ_c	Absorber phase shift, Eq.(2.32)
$\mu(E)$	Measured absorption coefficient, Eq.(2.30)
$\mu_o(E)$	Smooth background function, Eq.(2.30)
$\chi(k)$	EXAFS oscillation, Eq.(2.32)
$\Delta\mu_o(E)$	Measured jump in $\mu(E)$ at the threshold energy E_o, Eq.(2.30)

Introduction

1.1. Prions and TSEs

Proteinaceous infectious particles, or prions as they are more commonly known, are a unique type of infectious agents. Unlike other infectious agents, prions seem to consist solely of protein. Although the exact mechanisms of their pathogenesis and propagation remain unclear, it is widely accepted that prions are responsible for a group of neurodegenerative diseases in mammals classified as transmissible spongiform encephalopathies (TSEs). Table 1.1 summarizes TSEs for humans and other mammals (Prusiner, 1997). Typically these diseases are characterized by symptoms such as loss of motor control and dementia, ultimately resulting in the death of the infected organism. Although there is currently no cure for TSE infection, researchers have recently developed a vaccine for TSEs in mice that may lead to better understanding of the infection mechanism and ultimately provide the means to develop a treatment (Goñi et al., 2005).

The nature of the infectious agent responsible for TSEs is still debated. However, the most widely accepted proposal, the protein-only hypothesis, as its name implies, states that the infectious agent is a protein. TSEs show an extraordinary accumulation of the disease-associated isoform PrP^{Sc} of the cellular prion protein PrP^C, a host encoded glycoprotein which is mainly found in neurons within the central nervous system (CNS). The earliest idea that the infectious agent responsible for TSEs consists of protein was first postulated by Griffith (Griffith, 1967). The protein-only hypothesis was later formulated in detail by Prusiner (Prusiner, 1982). The protein-only hypothesis gained great acceptance after Prusiner and co-workers were able to purify the disease-related protein PrP27–30 (Prusiner, 1982). This protein, with a molecular weight of 27-30 kDa, is the protease-resistant core of PrP^{Sc} (Figure 1.1). It has been shown that genetic ablation of PrnP, the gene that encodes the prion protein,

protects mice from experimentally induced scrapie when exposed to prion, as predicted by the protein-only hypothesis (Weissmann, 1999). Alternative hypotheses about the nature of the infectious agent responsible for TSEs include the virus theory (Diringer et al., 1994) or the virino theory (Dickinson and Outram, 1988). However, these theories fail to explain many aspects of prion diseases and have lost support from the scientific community.

Disease	Mechanism of pathogenesis
Human Diseases	
Kuru (Fore people)	Infection though ritualistic cannibalism
Iatrogenic Creutzfeld-Jakob disease (iCJD)	Infection from prion-contaminated HGH, dura mater grafts, and so forth
Variant Creutzfeld-Jakob disease (vCJD)	Infection from bovine prions?
Familial Creutzfeld-Jakob disease (fCJD)	Germline mutation in PrP gene
Gerstmann-Sträussler-Scheinker disease (GSS)	Germline mutation in PrP gene
Fatal familial insommia (FFI)	Germline mutation in PrP gene (D178N and M129V)
Sporadic Creutzfeld-Jakob disease (sCJD)	Somatic mutation or spontaneous conversion of PrP^C into PrP^{Sc}?
Animal Diseases	
Scrapie in sheep	Infection in generally susceptible sheep
Bovine spongiform encephalopathy (BSE) in cattle	Infection with prion-contaminated meat and bone meal (MBM)
Transmissible mink encephalopathy (TME) in mink	Infection with prions from sheep or cattle
Chronic wasting disease (CWD) in mule deer, elk.	Unknown
Exotic ungulate encephalopathy in greater kudu, nyala, onyx	Infection with prion-contaminated MBM

Table 1.1: Prion diseases in mammals (Prusiner, 1997).
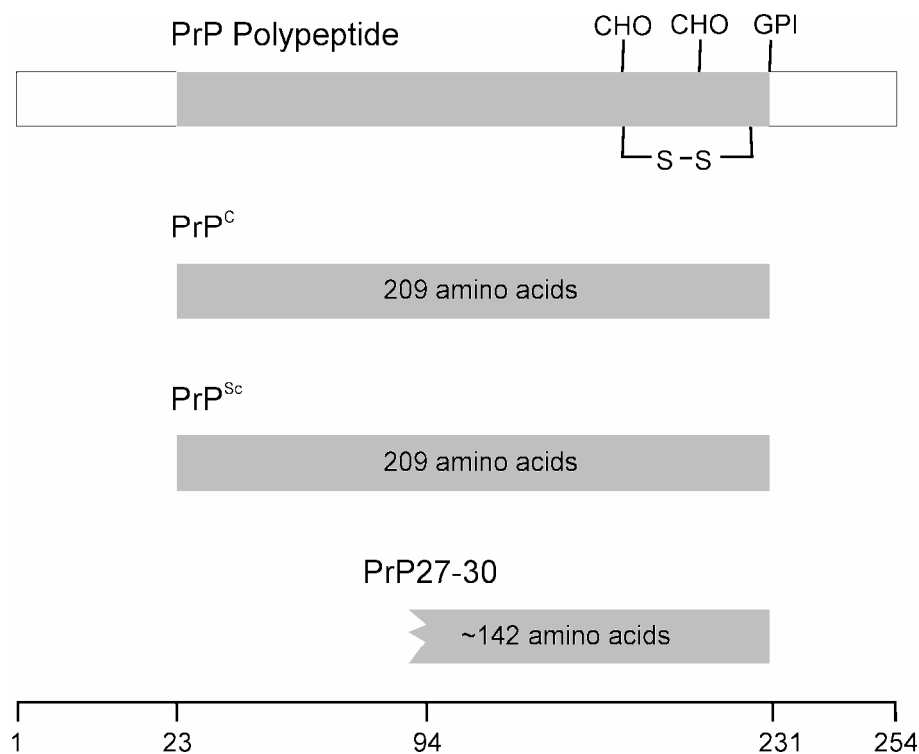
Figure 1.1: Bar diagram of Syriam hamster PrP which consists of 254 amino acids. After processing of the NH_2– and COOH–termini, both PrP^C and PrP^{Sc} consist of 209 residues. After limited proteolysis, the N-terminal domain of PrP^{Sc} is truncated to form PrP27–30, which is composed of approximately 142 amino acids (reproduced from (Prusiner, 1997)).

Prion diseases may present themselves as infectious, sporadic or genetic disorders. Typically, infectious agents like viroids or viruses transport genetic material that encodes strain-specific properties in genes of the host organism. In contrast, prions encipher these properties in the tertiary structure of PrP^{Sc}. The revolutionary concept of prions explicitly bears how a disease can manifest itself as heritable as well as an infectious illness. Although most of human prion diseases develop either as a consequence of transmission or sporadically, about 10% are familial and associated with mutations in the PrP gene. Genetic studies of over 200 cases of CJD, GSS, FFI, and kuru demonstrate that the familial forms of CJD and all the known cases of GSS and FFI are linked to mutation of the prion protein gene, either point mutations or expansion of the number of the repeat units in the so-called octarepeat region of the N-terminal domain of PrP (Goldfarb et al., 1994). The octarepeat region includes four consecutive repeats of the sequence PHGGGWGQ. Inherited amplification of the number of octarepeat units by sporadic mutations in the PrP gene has been found

to affect the pathogenesis of CJD in different families (Nicholl et al., 1995; Skworc et al., 1999; Windl et al., 1996). Goldfarb studied the effect of having an expanded number of octarepeat units in a group of 532 individuals (Goldfarb et al., 1994). The resulting data identified members of five families with CJD, a family with GSS, and a non-neurological control patient showing an amplification of octarepeat units (Table 1.2).

number of repeats	medical condition
4	normal
6	CJD
8	cirrhosis[1]
9	CJD
10	CJD
11	CJD
12	GSS
13	dement illness

Table 1.2: Number of octarepeat units in CJD, GSS and non-neurological control patients (adapted from (Goldfarb et al., 1994)).

This finding suggests that the octarepeat region plays an important role in the pathological mechanism of prion diseases. However, Flechsig showed that PrP devoid of the octarepeat region still sustains scrapie infection in mice, although the disease presentation and development are different than in wild-type mice (Flechsig et al., 2000). Therefore, the octarepeat region modulates the extent and presentation of disease.

1.2. Propagation Mechanisms

PrP^{Sc}, the so-called scrapie isoform, is derived from its cellular precursor PrP^{C} through a conformational change. The mechanism that triggers the transformation of the PrP^{C} into its misfolded isoform PrP^{Sc} is still unclear. All prions that have been discovered are believed to infect and propagate by formation of an amyloid fold, in

---

[1] The non-neurological patient, who died at age 63 of cirrhosis, had no family history of neurological disease, no clinical or pathological signs of spongiform encephalopathy, and the iatrogenic introduction of the patient's brain tissue did not transmit disease to experimental primates.

which PrP^{Sc} polymerizes into a fiber with a core consisting of tightly packed β–sheets. There are at least two different propagation models of PrP^{Sc} currently being considered. The first is referred to as the "template-directed refolding" hypothesis. According to this model, one PrP^{Sc} molecule would be able to impart its conformation onto monomeric PrP^{C}, resulting in two molecules of PrP^{Sc} (Prusiner, 1996). The second model, the "seeded nucleation" hypothesis, states that PrP^{Sc} and PrP^{C} coexist in equilibrium (Jarrett and Lansbury, 1993). According to this hypothesis, highly ordered aggregates of PrP^{Sc} molecules are the infectious agent and would be able to recruit monomeric PrP^{Sc} molecules into the infectious aggregate. Figure 1.2 shows these two conversion reactions (reproduced from (Cohen et al., 1994)). Experimental evidence favors the "seeded nucleation" hypothesis, particularly when considering prion replication using a yeast model (King and Diaz-Avalos, 2004; Tanaka et al., 2004).
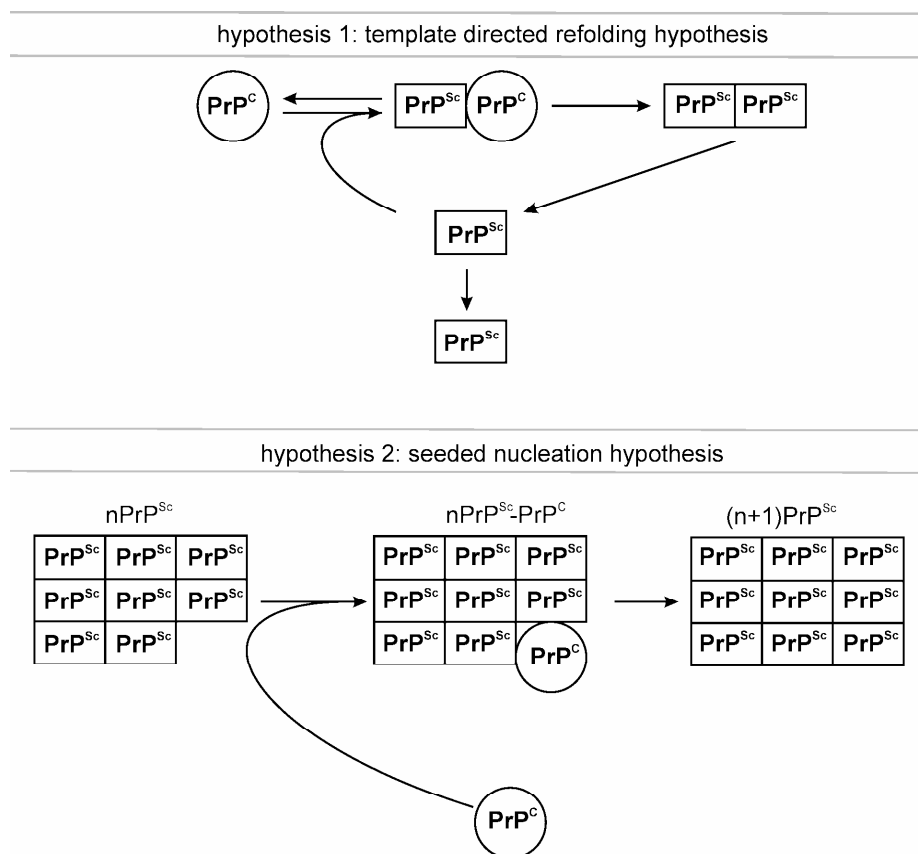
Figure 1.2: Alternative methods for the conversion of PrP^{C} to PrP^{Sc}. In hypothesis 1 PrP^{Sc} acts as catalyst for the conversion of PrP^{C} to further PrP^{Sc}, while in hypothesis 2 a polymerization reaction of PrP^{Sc} occurs with new monomers being recruited from PrP^{C}.

1.3. Function and Structure of Prion Protein

PrP^{C} is a glycoprotein which is attached to the cell surface via a glycosilphosphatidylinositol (GPI) anchor. Genetic ablation of the PrnP gene in mice results in animals that appear to develop and behave normally (Büeler et al., 1992), although a more detailed study found that PrP^{C} is necessary for normal synaptic function (Collinge et al., 1994). Different possible functions of PrP^{C} have been considered, including PrP^{C} involvement in signal transduction (Mouillet-Richard et al., 2000), Cu^{2+} transport or sequestration (Brown, 1999), and in antioxidant activity (Brown et al., 1999; Rachidi et al., 2003). However, the physiological function of PrP^{C}, and therefore the link between function and misfolding remains unclear.

A three-dimensional structural characterization of the prion protein may yield additional insights into the function of the prion protein and the misfolding of PrP^{C} to PrP^{Sc}.

NMR spectroscopy is the most appropriate spectroscopic method for the structure determination of biological samples in solution. This method has been used to determine the structure of the monomeric cellular forms of the mouse and Syrian hamster prion protein (Donne et al., 1997; Riek et al., 1997), as well as the structure of the recombinant human prion protein, hPrP(23–230) (Zahn et al., 2000). The resulting model is depicted in Figure 1.3. The model contains a globular domain that extends from residues 125–228, a flexibly extended N-terminal tail of residues 23–124, and a short flexible chain end of residues 229–230. This model basically shows the same features of the previously published structure of MoPrP (23–231) (Riek et al., 1997) and SHaPrP(29–231) (Donne et al., 1997).

The large flexibility of the N-terminal domain of PrP^{C} so far impedes a full structure characterization by NMR spectroscopy. One should also note that the previously-discussed NMR studies were made under acidic conditions, ranging from pH 4.5 (López García et al., 2000; Riek et al., 1997; Zahn et al., 2000) to 5.5 (Donne et al., 1997). In contrast, at pH values between 6.5 and 7.8, NMR spectroscopy indicated some structuring of the N-terminal part of the human prion protein, and suggests that

the N-terminal domain constitutes a pH-dependent folding site (Zahn, 2003).
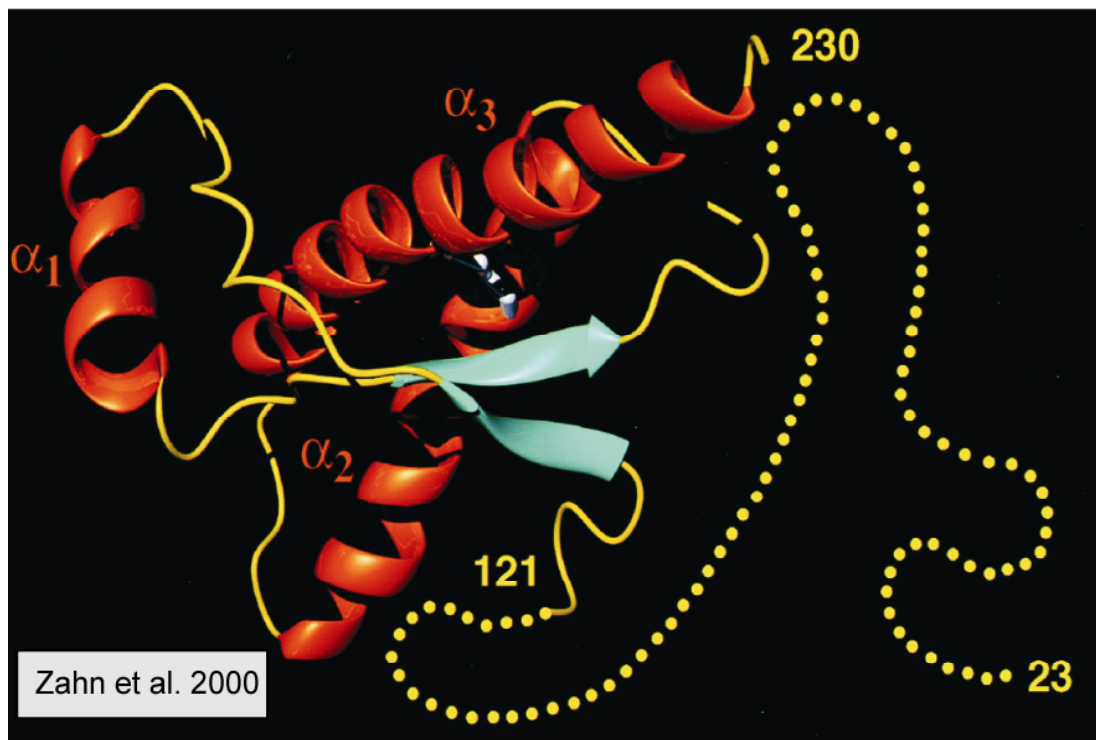
Figure 1.3: NMR structure of the recombinant human PrP(23-231). This structure contains a globular domain with 3 α-helix and two β-sheet domains. The dotted line ranging from residue 23 to 121 represents the unstructured N-terminal domain.

The crystal structure of the recombinant human PrP(90–231) reveals a dimeric conformation (Figure 1.4a) that suggests a mechanism for oligomerization (Knaus et al., 2001). Comparison with the NMR structure of the monomeric form of human prion protein (Zahn et al., 2000) reveals that the structural features that differ the greatest are helix 3 (α_3 in Figure 1.3 and 1.4). In the NMR structure, α_3 is placed between α_1 and α_2, whereas in the crystal dimer, α_3 packs between α_1^* and α_2^* of the second component of the dimer (Figure 1.4).
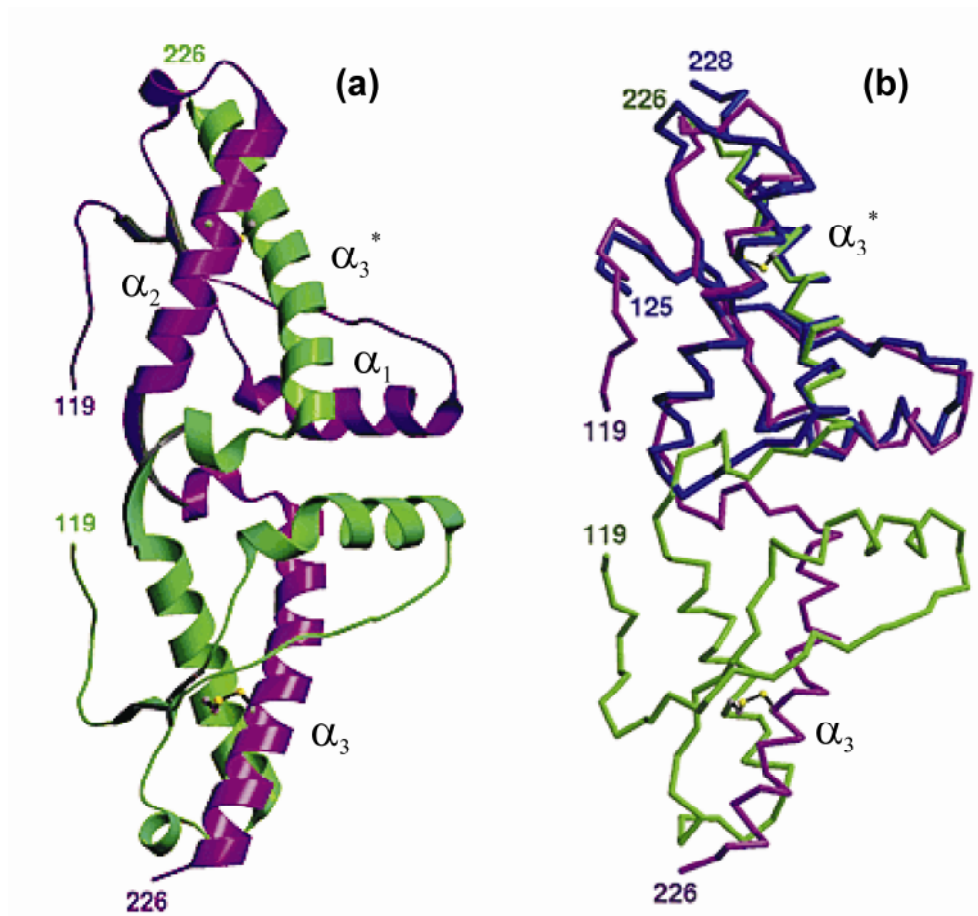
Figure 1.4: (a) Crystal structure of the human prion protein dimer. The two peptide chains are shown in green and violet; (b) View superposition of the monomeric solution NMR structure (blue chain) on the dimeric crystal structure (reproduced from (Knaus et al., 2001)).

Due to the unavailability of a crystallographic structure characterization of the full-length prion protein, a complete structural model with atomic resolution has yet to be completed.

PrP^C and PrP^{Sc} share the identical amino acid sequence. However, their tertiary structures differ from each other. PrP^C is rich in α-helical structure, whereas the folding structure of PrP^{Sc} seems to be formed mainly of β-sheets. Figure 1.5 shows two drawings of the PrP^C (a) and the putative PrP27–30 (b), protease-resistant core of PrP^{Sc}, where the folding differences can be observed.
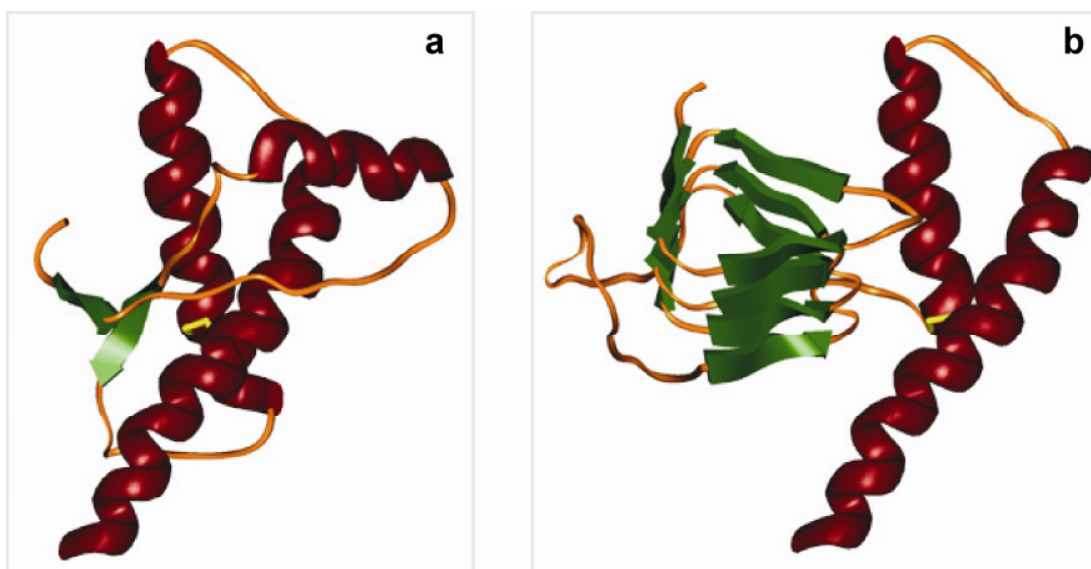
Figure 1.5: (a) Drawing of the NMR structure of Syrian hamster PrP(90–231) (PDB ID code 1b10, (Liu et al., 1999)). Residues 90–115 are not shown. (b) Model of the monomer of PrP27–30. The α–helical region (residues 177-227) as determined by NMR spectroscopy (PDB ID code 1QM0) was linked to the putative structure of the β–sheet region.

Detailed information about the structure of PrP^{Sc} is important for an understanding of the prion propagation and the pathogenesis of neurodegeneration. Unfortunately, due to the inability to isolate individual PrP^{Sc}, X-ray crystallography and NMR spectroscopy have failed to assist in determining the structure of the PrP^{Sc} with atomic resolution. Despite this limitation, electron crystallography has been able to create low resolution models of two infectious variants of the prion protein: the N-terminally truncated PrP^{Sc} (PrP27–30) and a miniprion (PrP^{Sc}106) (Wille et al., 2002).

1.4. Copper Binding to Prion Protein

The prion protein is a copper-metalloprotein that binds Cu^{2+} with high affinity (Hornshaw et al., 1995a; Hornshaw et al., 1995b). A number of studies have addressed the biological relevance of the Cu^{2+} binding in PrP^{C}, including involvement of the PrP^{C} in the copper uptake from extracellular environments to endosomes and the inverse release process (Brown et al., 1997; Kramer et al., 2001),

and reduction of Cu^{2+} prior to their transfer to Cu^+-specific trafficking proteins (Miura et al., 2005). Brown demonstrated that mice with genetic ablation of the PrP^C gene exhibit severe reductions in the copper content of membrane-enriched brain extracts and similar reductions in synaptosomal and endosome-enriched subcellular fractions (Brown et al., 1997). These findings indicate that PrP^C can bind Cu^{2+} *in vivo* and link the Cu^{2+} binding with the function of PrP^C. Later studies from Kretzschmar´s institute indicate that the N-terminal part of the full-length human PrP(23-231) binds cooperatively up to 5 Cu^{2+} at physiological pH value (Kramer et al., 2001).

A considerable number of biophysical and biochemical investigations on both recombinant PrP and PrP-derived peptides have focused on identifying the Cu^{2+} binding sites, their affinities and coordination (see e.g. (Burns et al., 2003; Chattopadhyay et al., 2005; Jackson et al., 2001; Viles et al., 1999)). The current consensus about the Cu^{2+} binding sites to PrP^C states that at pH 7.4 PrP^C binds up to four Cu^{2+} ions with high affinity in the octarepeat region, and one or two additional Cu^{2+} ions in the unstructured region between the octarepeat domain and the structured C-terminal part of PrP^C (Figure 1.6). This region, which corresponds to residues 90–120 of the human PrP, is considered essential for amyloid formation and infection in prion diseases (Muramoto et al., 1996). Coordination of one or two additional Cu^{2+} has been contemplated at sites involving histidine residues corresponding to the positions 96 and 111 of recombinant human PrP(23-231). However, there is disagreement in literature about these additional binding sites. The reported affinities and coordinating ligands of these additional sites have varied greatly (Brown, 1999; Burns et al., 2003; Hasnain et al., 2001; Jackson et al., 2001; Jones et al., 2004; Kramer et al., 2001). Copper binding to this region has been shown to induce a β-sheet-like conformation, suggesting that Cu^{2+} binding might play an important role in amyloidogenesis and misfolding of PrP (Jones et al., 2004).

It should be emphasized that most of studies dealing with the characterization of the Cu^{2+} binding to PrP^C were carried out in synthetic PrP-derived peptides representing the octarepeat domain. It is questionable whether these synthetic peptides can be considered a complete model for Cu^{2+} binding to the prion protein or if the C-

terminal domain plays a role in the folding of the N-terminal domain when it binds Cu^{2+}. The study of copper binding is easier in PrP-derived peptides than in recombinant PrP, since copper binds most readily at pH 7.0 where the PrP-derived peptides are more soluble than the recombinant PrP. As a result, the structure determination of the fully Cu^{2+} binding side of PrP in solution remains uncertain.
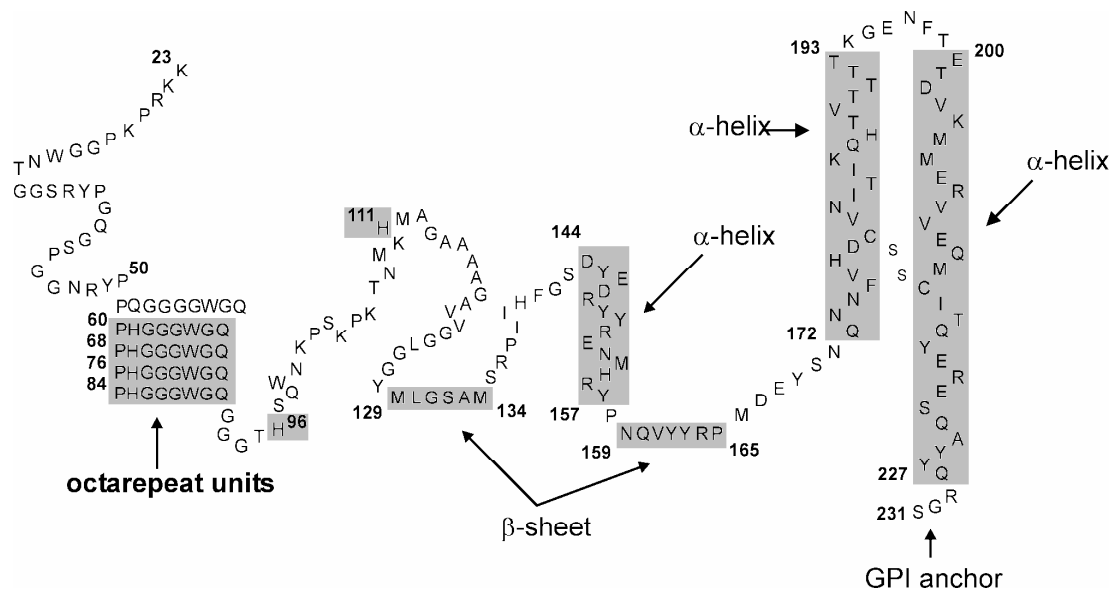
Figure 1.6: Schematic of the human prion protein, hPrP(23-231). The figure shows the location of the three α-helix and two β-sheet. In addition, the octapeptide units and histidine residues corresponding to the positions 96 and 111 of recombinant human PrP(23-231) are highlighted.

1.5. Motivation

The main aim of this work is to characterize the three-dimensional structure of the recombinant full-length human PrP(23-231) in complex with Cu^{2+}. For this purpose, a combination of spectroscopic methods together with molecular mechanics calculations are performed on the copper complexes formed by recombinant human PrP(23-231) and PrP-derived peptides. The results are compared with existing models addressing the Cu^{2+} binding to PrP. A novel structural model for the entire octarepeat domain of PrP^C in the presence of two Cu^{2+} ions is presented. Given the low availability of Cu^{2+} in the extracellular environment, this novel Cu^{2+} binding mode might be more likely to exist *in vivo*.

Theoretical Principles

2

2.1. Electron Paramagnetic Resonance (EPR)

2.1.1. Electron Zeeman Interaction

For the discussion of the basic principles of EPR, the simple case of a paramagnetic center with an unpaired electron and therefore, two spin states, shall be examined first. In the absence of a magnetic field, the magnetic moment associated with the electron spin is randomly oriented and the two spin states are degenerated. In this particular case, the application of a magnetic field $\vec{B}_o$ results in a splitting of the energy levels of the two spin states. The electron Zeeman interaction describes the splitting of the energy levels caused by a magnetic field $\vec{B}_o$. The quantum mechanical description of the electron Zeeman interaction is represented by the spin Hamilton operator

$$\hat{H}_s = \mu_B \vec{B}_o \ddot{g}_{eff} \hat{S}_z, \tag{2.1}$$

where $\ddot{g}_{eff}$ is the effective g tensor which takes the value 2.0023 in the case of the free electron, μ_B the Bohr magneton and $\hat{S}_z$ the z component of the electron spin operator.

A spin system characterized by a spin S has associated $2S+1$ wave functions $|\psi\rangle_i$, where i ranges from 1 to $2S+1$. Each wave function $|\psi\rangle_i$ is defined by a spin quantum number m_S. The allowed values of m_S range in unit increments from $-S$ to $+S$. The wave funtions $|\psi\rangle_i$ fulfill the Eq. (2.2) as

$$\hat{H}_s |\psi\rangle_i = \mu_B \vec{B}_o \vec{g}_{eff} |\psi\rangle_i . \qquad (2.2)$$

The energy of the spin states is then given by the eigenvalues of $\hat{H}_s$ in Eq. (2.2) and it is characterized by the spin quantum numbers m_S,

$$E(m_s) = g_{eff} \mu_B B_0 m_s , \qquad (2.3)$$

where g_{eff} is a dimensionless g factor, generalized to the effective $\vec{g}_{eff}$ tensor. Thus, the energy difference between the states spin up and down is given by:

$$\Delta E = E(+\frac{1}{2}) - E(-\frac{1}{2}) = g_{eff} \mu_B B_o . \qquad (2.4)$$

Transitions between the two spin states can be induced by electromagnetic radiation of frequency v if it matches the energy difference between spin states and then, the resonance condition is fulfilled when

$$\Delta E = hv = g_{eff} \mu_B B_o . \qquad (2.5)$$

The transitions fulfilling the resonance condition imply the following selection rule for the magnetic quantum number:

$$\Delta m_S = \pm 1 . \qquad (2.6)$$

In continuous wave EPR, spectra are usually measured at a fixed frequency and the magnetic field is varied. Then, transitions are detected when the applied magnetic field B_o fulfills the resonance condition as shown in Eq. (2.5). For the simple case of a two level system, Figure 2.1 illustrates the EPR transition at a fixed frequency v.
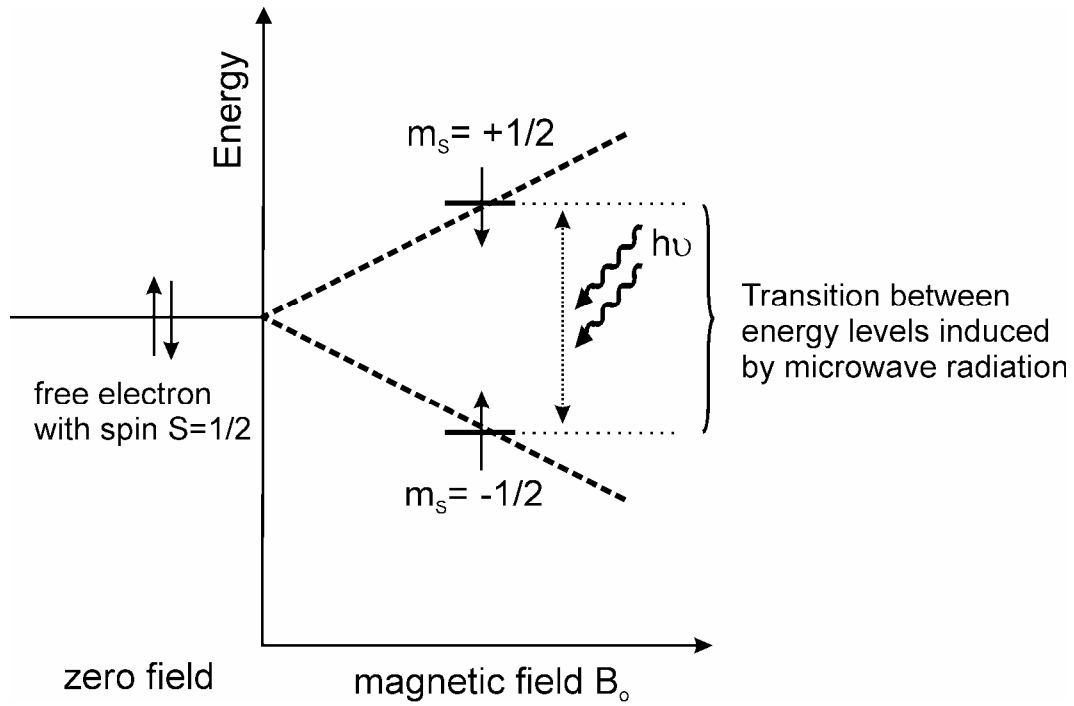
Figure 2.1: Illustration of the Zeeman splitting for a $S = 1/2$ system with one unpaired electron in a external magnetic field $\vec{B}_o$. Transitions between the energy levels of an unpaired electron are induced by application of microfrequency radiation.

In thermal equilibrium, the population distribution of spin states of a paramagnetic system follows the Boltzmann distribution. Therefore, the number of paramagnetic ions in the spin up and down states of Figure 2.1 fulfills the following formula:

$$\frac{N_{+1/2}}{N_{-1/2}} = e^{\frac{-\Delta E}{k_B T}} = e^{\frac{-g_{eff}\mu_B B}{k_B T}} \, , \tag{2.7}$$

where $N_{+1/2}$ and $N_{-1/2}$ represent the population of spin up and down respectively, k_B is the Boltzmann factor and T the temperature.

For a system with values of ΔE and T such as

$$g_{eff}\mu_B B \ll k_B T \, , \tag{2.8}$$

the expression shown in Eq. (2.7) can be simplified as

$$\frac{N_{+1/2}}{N_{-1/2}} \approx 1 - \frac{g_{eff}\mu_B B_o}{k_B T}, \tag{2.9}$$

and then, the population difference between the two energy levels results in:

$$N_{-1/2} - N_{+1/2} = N_{-1/2}\left[1 - \left(1 - \frac{g_{eff}\mu_B B_o}{k_B T}\right)\right] \approx \frac{N g_{eff}\mu_B B_o}{2 k_B T}, \tag{2.10}$$

where N is the sum of spin states up and down,

$$N = N_{-1/2} + N_{+1/2}. \tag{2.11}$$

Eq. (2.10) shows that an excess population exists in the lower state which depends upon temperature. Therefore, the EPR signal strength must depend on this Boltzmann population difference and consequently, upon temperature.

2.1.2. Anisotropy of the Electron Zeeman Interaction

In contrast to the case of the free electron, an unpaired electron in a molecule experiences additional magnetic and electric fields depending on its particular environment. If the interactions between the different magnetic moments, electric moments, and fields are smaller than the electron Zeeman term, they can be described by additional terms in the spin Hamiltonian shown in Eq. (2.1), and will lead to further splitting of the energy levels.

For transition metal ions in the condensed phase, the interactions responsible of the additional splitting of the EPR signal are the crystal-field and the spin-orbit coupling. The combined effect of these two interactions removes the orbital degeneracy of the energy levels for most transition metal ions. These additional interactions leave a non-degenerate ground state. In most of the cases, this ground state has zero orbital angular momentum (quenching of the orbital angular momentum). Thus, one might expect that in these cases the g factor would have precisely the free-electron value. However, the interaction of the ground state with certain excited states admixes small

amounts of orbital angular momentum to the ground state. The electron spin then couples to the molecular ground state and becomes sensitive to the electronic environment. As a result, the g factor is no longer isotropic and the splitting of the Zeeman levels depends on the symmetry of the ligand field and the orientation of the system in the external magnetic field.

Due to the orientation dependence of the paramagnetic system, g_{eff} becomes a tensor and it has a unique axis system called the principal axis system. For a single crystal sample, the EPR spectrum depends on the orientation of the sample with respect to the magnetic field. In the case of a powder sample, the EPR spectrum represents the weighted average of all possible orientations of a crystal with respect to the magnetic field. In a liquid, however, the anisotropy may be averaged out by the rotational and translational motion of the molecules and then, the EPR signal gets much narrower and appears at the isotropic part of the $\vec{g}_{eff}$ tensor (Wertz and Bolton, 1972). Note that at low temperatures the molecular motion is "frozen" and then, frozen solution and powder samples exhibit equivalent EPR spectra.

The orientation dependence of the Zeeman interaction is expressed by the $\vec{g}_{eff}$ tensor as an orthorhombic 3x3 matrix which can be expressed in its principal axis system by

$$\vec{g}_{eff} = \begin{bmatrix} g_{xx} & 0 & 0 \\ 0 & g_{yy} & 0 \\ 0 & 0 & g_{zz} \end{bmatrix}.$$

For an arbitrary orientation of $\vec{B}_o$ the expression for the resonant field is obtained by insertion of the following expression

$$g_{eff}^2 = g_{xx}^2 l_{xx}^2 + g_{yy}^2 l_{yy}^2 + g_{zz}^2 l_{zz}^2 \tag{2.12}$$

into the resonance condition described by Eq. (2.5). Where l_{xx}, l_{yy} and l_{zz} are the direction cosines between $\vec{B}_o$ and the principal axis of the $\vec{g}_{eff}$ tensor. The direction cosines are defined as:

$$l_{xx}^2 = \sin^2 \theta \cdot \cos^2 \phi \; ; \; l_{yy}^2 = \sin^2 \theta \cdot \sin^2 \phi \; ; \; l_{zz}^2 = \cos^2 \phi,$$

where (θ, ϕ) are the polar angles describing the orientation between $\vec{B}_o$ and the principal axis of the $\vec{g}_{eff}$ matrix.

For an isotropic Zeeman interaction where $g_{xx} = g_{yy} = g_{zz} = g_{eff}$, the expression $\vec{B}_o \cdot \vec{g}_{eff}$ can be written as:

$$\vec{B}_o \cdot \vec{g}_{eff} = B_o \cdot (l_{xx} \quad l_{yy} \quad l_{zz}) \begin{bmatrix} g_{xx} & 0 & 0 \\ 0 & g_{yy} & 0 \\ 0 & 0 & g_{zz} \end{bmatrix} = B_o \cdot g_{eff}. \qquad (2.13)$$

2.1.3. Nuclear Effects on EPR

If the electron Zeeman interaction were the sole process taking place in a paramagnetic system sited in an external magnetic field, all the EPR spectra would consist of one line which may be broadened due to the anisotropy of the $\vec{g}_{eff}$ tensor. However, the information content of an EPR spectrum is substantially enhanced if nuclei with a spin quantum number I greater than zero are found in the vicinity of the unpaired electron.

In analogy to the electron spin, the nuclear spin I is quantized in a magnetic field resulting in the nuclear Zeeman splitting of the nuclear spin states. Moreover, we have to consider the interaction of the electron spin with the nuclear spins in its vicinity. The term nuclear hyperfine interaction makes reference to the interaction of the unpaired electron with the surrounding nuclei. Usually, it is called hyperfine if the nucleus and the unpaired electron belongs to the same atom, and superhyperfine if it results from the interaction with other neighboring nuclei in the vicinity of the unpaired electron. The magnitude of the hyperfine interaction is considerably larger than the superhyperfine interaction, which is often not resolved in continues wave EPR.

In order to analyze and describe the EPR signal, the nuclear interactions have to be added to the spin Hamiltonian of Eq. (2.1) as follows:

$$\hat{H}_S = \mu_B \vec{B}_o \vec{g}_{eff} \hat{S}_z - \mu_N \vec{B}_o \vec{g}_N \hat{I}_z + \hat{\vec{I}}\vec{A}_{HF}\hat{S} + \hat{\vec{I}}\vec{A}_{SHF}\hat{S} \,, \qquad (2.14)$$

where $\vec{g}_N$ is the nuclear g tensor, $\vec{A}_{HF}$ is the nuclear hyperfine coupling tensor, $\vec{A}_{SHF}$ is the nuclear superhyperfine coupling tensor, $\hat{I}_z$ is the $z-$component of the nucleus spin operator $\hat{I}$, and μ_N is the nuclear magneton. Eq. (2.14) sums up the nuclear interactions to the spin Hamiltonian. The second term of Eq. (2.14) represents the nuclear Zeeman interaction, whereas the third and fourth correspond to the hyperfine and superhyperfine interactions respectively.

The nuclear Zeeman interaction is much smaller than the electron Zeeman interaction and its small anisotropy is usually neglected in EPR. Note for instance that the ratio $\dfrac{\mu_B g_e}{\mu_N g_N}$ takes the value 660 for an unpaired electron with $g_e = 2$ and a proton with $g_N = 5.58$.

The nuclear hyperfine interaction at the electron spin depends on the orientation of the nuclear spins with respect to the applied magnetic field. For a given nuclear quantum number I, a splitting into $2I+1$ energy levels is expected. Each of these states is characterized by a nuclear magnetic spin quantum number m_I. The allowed values of m_I range in unit increments from $-I$ to $+I$.

For simplification, let us assume an isotropic interaction where superhyperfine contributions are negligible. Then, $\vec{g}_{eff}$ and $\vec{A}_{HF}$ become diagonal matrices with elements g_{eff} and A_o. Regarding the perturbation theory, the Hamiltonian of Eq. (2.1) may be separated into two parts

$$\hat{H}_S = \hat{H}_o + \hat{H}' \,, \qquad (2.15)$$

where

$$\hat{H}_o = g_{eff}\mu_B\vec{B}_o\hat{S}_z + \hat{S}_z A_o \hat{I}_Z - g_N\mu_N\vec{B}_o\hat{I}_z \tag{2.16}$$

and

$$\hat{H}' = \frac{A_o}{2}(\hat{S}_+\hat{I}_- + \hat{S}_-\hat{I}_+). \tag{2.17}$$

Where the terms $\hat{I}_+$ and $\hat{I}_-$ are the so-called "ladder" operators, which are linear combinations of the $x-$ and $y-$ components of the tensors $\hat{I}$, $\hat{I}_x$ and $\hat{I}_y$:

$$\hat{I}_+ = \hat{I}_x + i\hat{I}_y \text{ and } \hat{I}_- = \hat{I}_x - i\hat{I}_y.$$

If we consider the reasonable assumption that $\hat{H}_o >> \hat{H}'$ then, in the context of the perturbation theory, one can use the eigenfunctions of $\hat{H}_o$ as a basis set for determining the energy corrections due to $\hat{H}'$ (Wertz and Bolton, 1972). Thus, the energies of the different states can be obtained by evaluating Eq. (2.15) for each state:

$$E_{m_S,m_I} = \langle m_S, m_I | \hat{H}_S | m_S, m_I \rangle, \tag{2.18}$$

where each state is characterized by the quantum numbers m_S and m_I.

Let us now consider a more specific system with one unpaired electron and a paramagnetic center with nucleus spin $I = 3/2$, which is for instance the case for the copper isotope $^{63}Cu^{2+}$. The possible combinations of m_S and m_I lead us to eight states $|m_S, m_I\rangle$. Regarding a sufficiently small A_o value, one can neglect the Hamilton matrix elements out of the diagonal and thereby, the energy for each state $|m_S, m_I\rangle$ is in good approximation:

$$E_{m_S,m_I} = m_S g_{eff}\mu_B B_o + \frac{m_I}{2}A_o - g_N\mu_N B_o m_I, \tag{2.19}$$

where the latest term, the nuclear Zeeman interaction, might be omitted because it

does not affect the transition energies as shown in Figure 2.2.

The application of electromagnetic radiation of frequency υ to a paramagnetic system will cause transitions along the non-degenerate levels. As already mentioned, for an electron spin transition, the magnetic quantum number must fulfill the selection rule $\Delta m_S = \pm 1$. Such transitions correspond to a change in spin of $\pm \hbar$. A photon has an intrinsic angular momentum equal to $\hbar$. Hence, if the condition $\Delta m_S = +1$ is fulfilled when a photon is absorbed then, m_I must remain unchanged to conserve the total angular momentum. Therefore, resonance occurs for transitions which fulfill the selection rules $\Delta m_S = \pm 1$ and $\Delta m_I = 0$.

(a) Zero Field   (b) Electron Zeeman   (c) Hyperfine   (d) Nuclear Zeeman
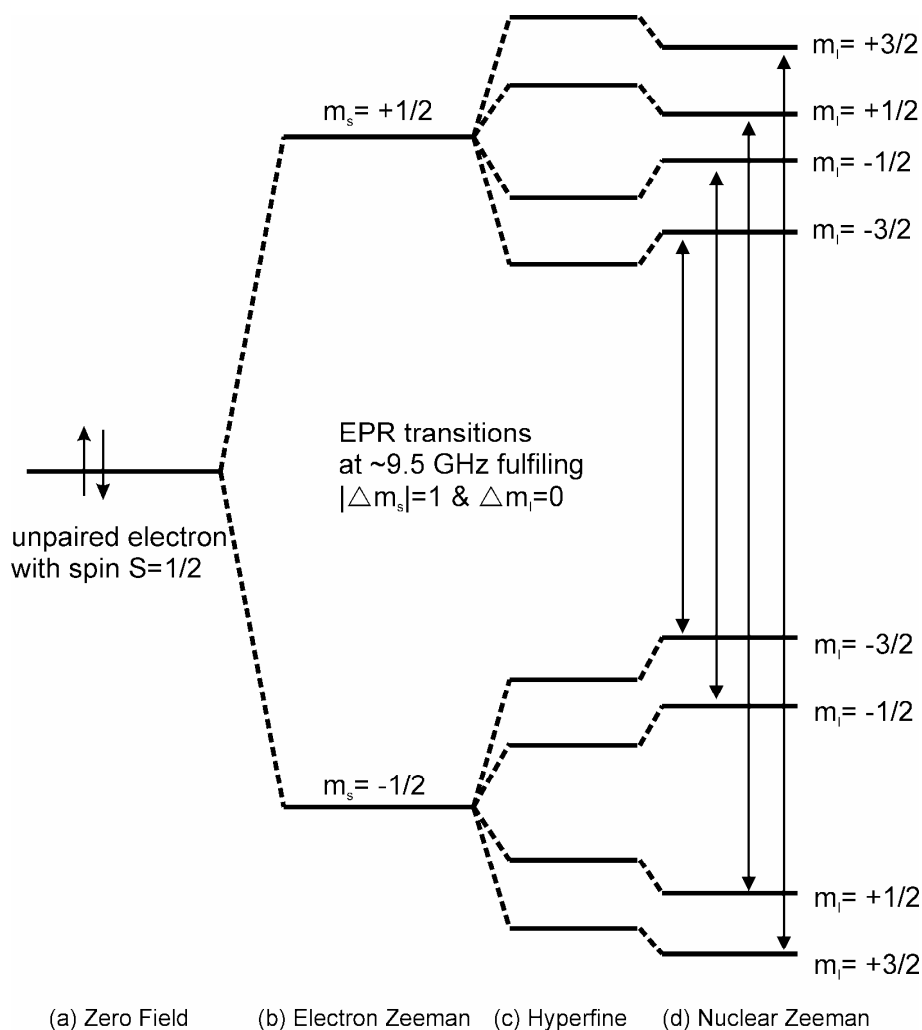
Figure 2.2: EPR transitions in a Cu^{2+} system. According to the EPR selection rules, four absorption lines are expected for a system with $S = 1/2$ and $I = 3/2$.

2.1.4. Copper Complexes in Frozen Solution

EPR spectra of paramagnetic systems in frozen solution include all possible orientations of an analogous single crystal with respect to the magnetic field. The electron Zeeman interaction is much larger than the copper hyperfine coupling. Assuming that the nuclear Zeeman interaction and superhyperfine interaction are negligible, one can treat the copper hyperfine interaction by second order perturbation theory. In the context of this approximation, one often assumes that $\vec{\vec{g}}_{eff}$ and $\vec{A}^{Cu}$ are coaxial with axially symmetric matrices. Then, one can consider the following simplifications: $g_{xx} = g_{yy} = g_{\perp}$, $g_{zz} = g_{\parallel}$, and $A_{xx} = A_{yy} = A_{\perp}$, $A_{zz} = A_{\parallel}$, and subsequently, one can write the following $\vec{\vec{g}}_{eff}$ and $\vec{A}^{Cu}$ matrices:

$$\vec{\vec{g}}_{eff} = \begin{bmatrix} g_{\perp} & 0 & 0 \\ 0 & g_{\perp} & 0 \\ 0 & 0 & g_{\parallel} \end{bmatrix} \text{ and } \vec{\vec{A}}^{Cu} = \begin{bmatrix} A_{\perp Cu} & 0 & 0 \\ 0 & A_{\perp Cu} & 0 \\ 0 & 0 & A_{\parallel Cu} \end{bmatrix}.$$

The orientation of the copper complex with respect to the external magnetic field $\vec{B}_{o}$ is given exclusively by the angle θ. Therefore, the contribution of molecules with the same angle θ to the EPR spectrum averages over the angle φ as depicted in Figure 2.3. In analogy to the $g - factor$, A_{eff} can be depicted in the same fashion as g_{eff}.
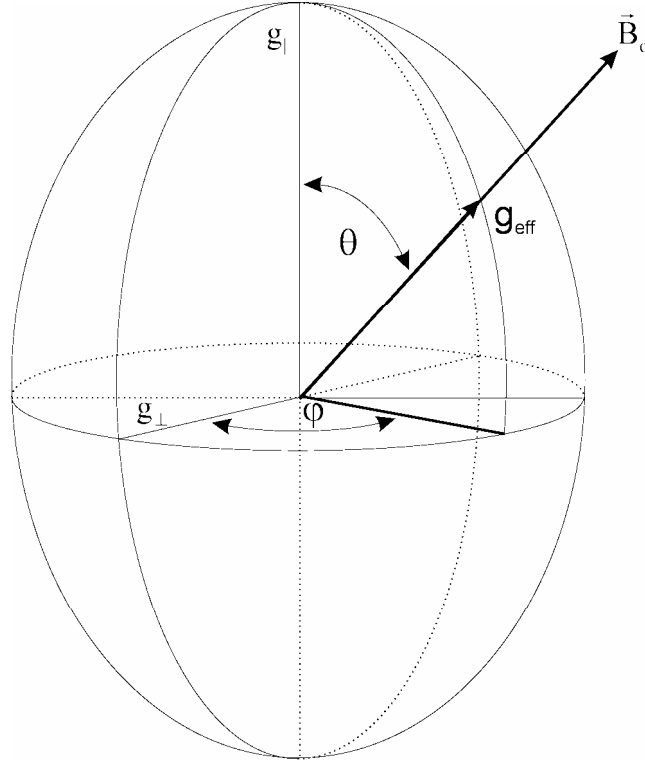
Figure 2.3: $g-$ ellipsoid for a complex with axial symmetry in which $g_\perp < g_\parallel$.

In copper complexes with axial symmetry in frozen solution, one expects that all orientations of the symmetry axis will be equally probable. Let us consider a sphere of radius r fixed in the magnetic field $\vec{B}_o$. Thus, a solid angle Ω is defined to be the ratio of a surface area A to the total area of the sphere:

$$\Omega = \frac{A}{4\pi \cdot r^2}.$$

The EPR parameters g_{eff} and A_{eff} remain about constant on the infinitesimal element of area defined by $\delta\Omega$. Due to the axial symmetry of the system, $\delta\Omega$ depends solely of the angle θ as:

$$\delta\Omega = \frac{\delta\varphi \cdot \delta\theta}{r^2} \propto \theta.$$

As already mentioned, all orientations of the symmetry axis will be equally probable and then, the number of copper complexes contributing to the EPR spectrum with about the same parameters is proportional to the area of $\delta\Omega$ (Wertz and Bolton,

1972). Figure 2.4 illustrates θ dependence of the solid angle $\delta\Omega$ by showing their magnitudes at $\theta = 10°$ and $\theta = 90°$. More molecules perpendicularly oriented (i.e $\theta = 90°$) to the magnetic field contribute in $\delta\Omega$ than molecules parallel oriented (i.e $\theta = 10°$).
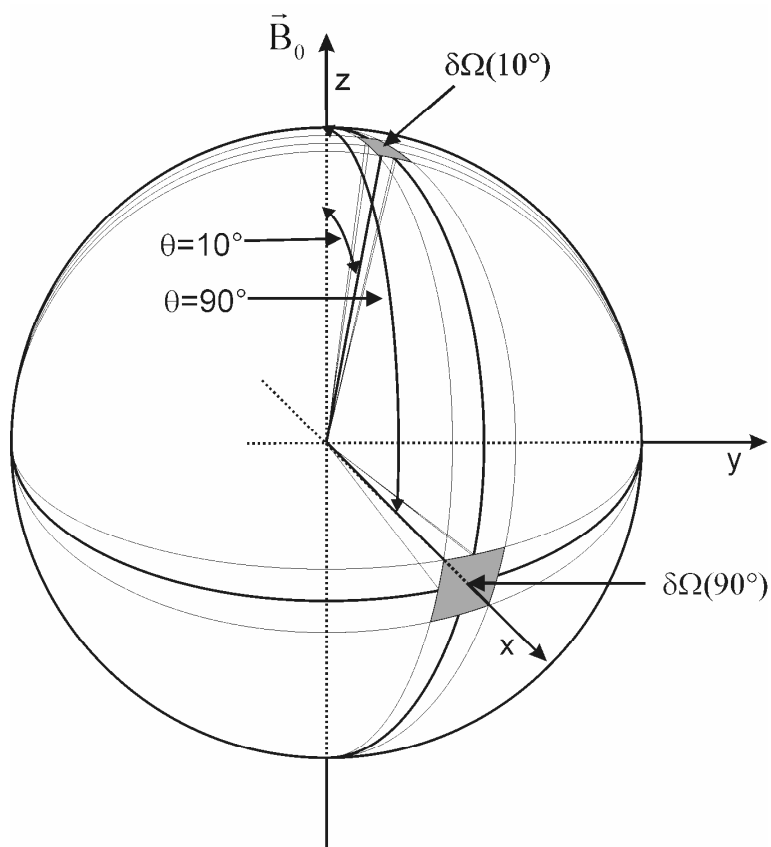
Figure 2.4: θ dependence of $\delta\Omega$. The enclosed area by $\delta\theta$ and $\delta\varphi$ is greater at $\theta = 90°$ than at $\theta = 10°$.

Typically, Cu^{2+} complexes with axial symmetry exhibit EPR spectra with a line shape very asymmetric. Figure 2.5 shows how the copper complexes contribute differently to the EPR spectrum depending on their relative orientation with respect to the external magnetic field $\vec{B}_o$. The molecules with symmetry axis perpendicular oriented to the magnetic field overlap in the high field region of the EPR spectrum.
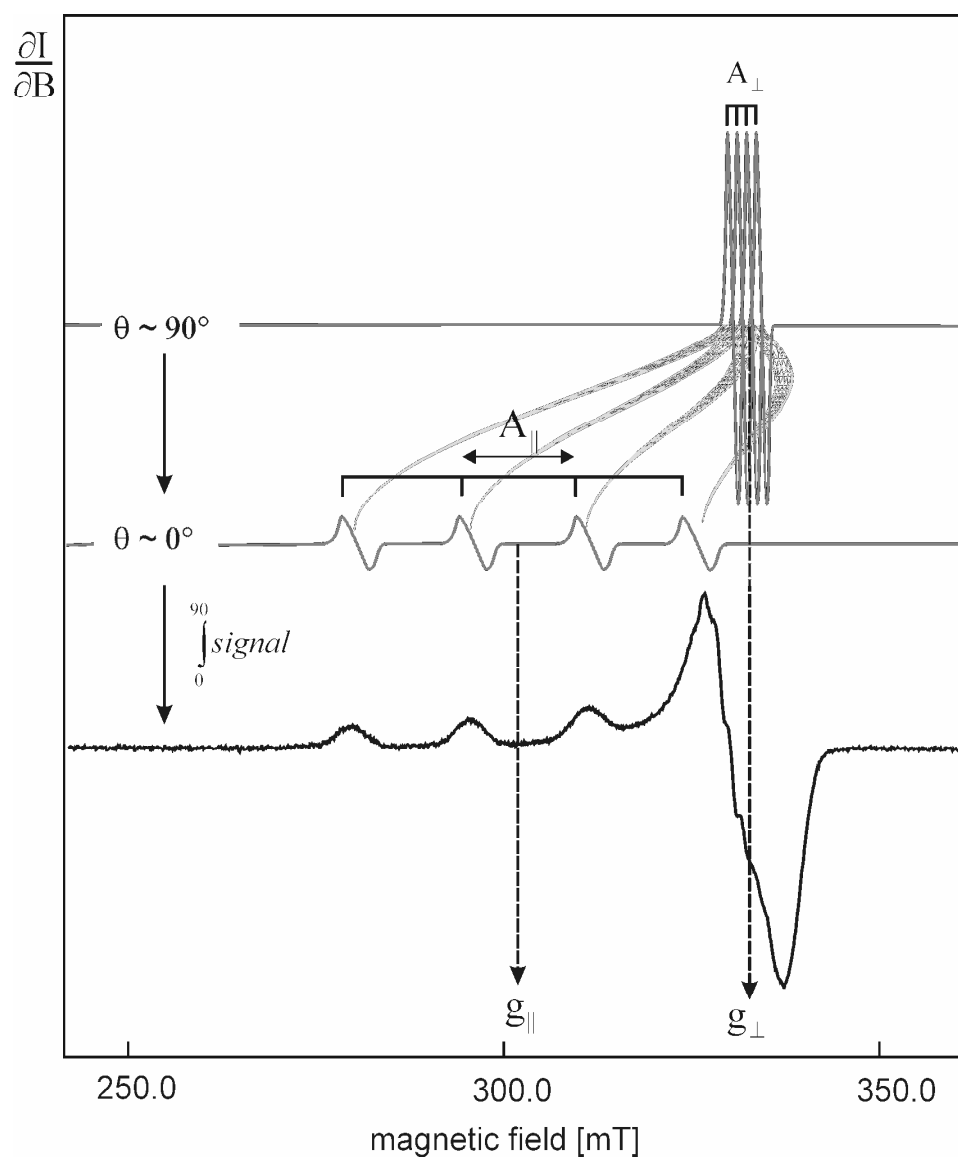
Figure 2.5: Experimental EPR spectrum of a Cu^{2+} complex with axial symmetry. The contribution of molecules in which the symmetry axis points perpendicular ($g_\perp$) and parallel ($g_\parallel$) to the magnetic field are shown separately.

2.2. Electron Nuclear Double Resonance (ENDOR)

2.2.1. ENDOR Phenomenon

As already mentioned, nuclear spins with $I > 0$ can interact with the unpaired electron spin, and cause further splitting of the energy levels. Unfortunately, in a continuous wave EPR spectrum, the observation of nuclear contributions is rather limited to the nucleus where the unpaired electron originates. However, in a continuous wave ENDOR experiment, nuclear magnetic resonance (NMR) transitions are observed via the intensity change of partially saturated EPR transitions, by sweeping radiofrequency radiation through NMR transitions. If nuclei such as e.g. protons ^1H ($I = 1/2$) or nitrogens ^{14}N ($I = 1$) are found in the environment of the unpaired electron then, ENDOR spectroscopy can give valuable information about the neighboring nuclei such as nuclear positions.

For the discussion of the ENDOR process, let us consider a simple system with one unpaired electron and a paramagnetic center with nuclear spin $I = 1/2$ (Figure 2.6). The possible combinations of m_S and m_I lead us to four states $|m_S, m_I\rangle$ (letters A, B, C and D in Figure 2.6). An EPR experiment involves only the spin-lattice relaxation time T_{1e} which governs the EPR transitions $D \rightarrow A$ and $C \rightarrow B$. As already mentioned, these transitions fulfill the selection rules $\Delta m_S = \pm 1$ and $\Delta m_I = 0$. During a continuous wave ENDOR experiment, an EPR transition (let us consider a magnetic field that selects the path $D \rightarrow A$ in Figure 2.6) is driven at resonance and saturated while simultaneously variable radiofrequency radiation is applied. If the radiofrequency field is in resonance with the particular NMR transition that connects the states A and B, then, the respective relaxation path will be short circuited. Therefore, the level A gets depopulated. This leads to desaturation of the EPR transitions resulting in an increase of the EPR signal which is detected as the ENDOR signal.

Here, it should be emphasized that in an ENDOR experiment, the absorption of radiofrequency radiation is not directly observed. Instead, one observes the change of

the EPR signal resulting from the redistribution of population of different levels. The magnitude of the EPR response depends clearly on the electron relaxation rates (T_{1e}), the nuclear relaxation rates (T_{1n}), and the cross relaxation rates (T_{xx} and T_x). Relaxation rates also dictate the required experimental conditions such as temperature. In the absence of microwave or RF fields, the reciprocal of these times represent the rates of transition between the levels which they connect. T_{1e} is the electron spin relaxation time, T_{1n} is the nuclear spin-lattice relaxation time that is associated with the transitions $\Delta m_S = \pm 1$ and $\Delta m_I = 0$. T_x is a cross relaxation time associated with mutual "spin flips" for processes where $\Delta(m_I + m_S) = 0$. T_{xx} is the cross relaxation time for $\Delta(m_I + m_S) = 2$.
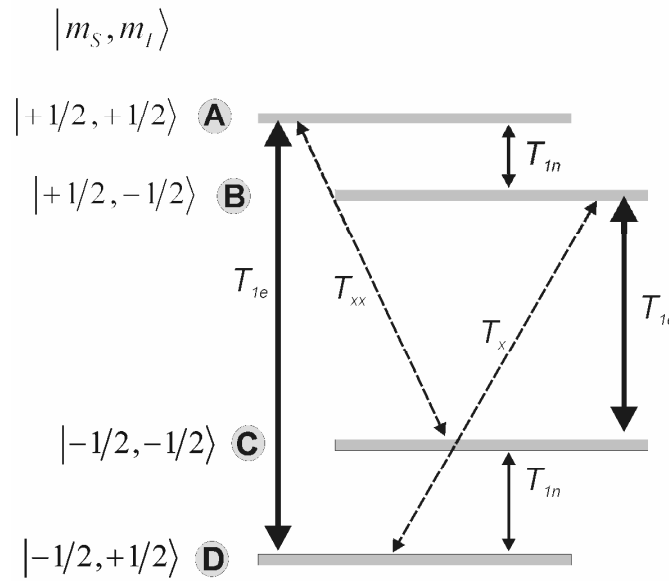
Figure 2.6: The ENDOR relaxation times T_{1e}, T_{1n}, T_x, and T_{xx} connecting the energy levels A, B, C and D during an ENDOR process for a system with one unpaired electron and a nucleus with $I = 1/2$.

Neglecting the cross relaxation times, optimum ENDOR signals are observed when $T_{1e} = T_{1n}$ (Murphy and Farley, 2006). However, typically $T_{1n} \gg T_{1e}$. These rates can be tuned by altering the temperature and viscosity of the solvent. As the temperature decreases and viscosity increases, then T_{1n} becomes smaller and T_{1e} larger. For most solid-state systems, one requires temperatures ranging from 4 K to 20 K to do a

successful ENDOR experiment. At these temperatures one can often achieve microwave saturation with modest power because T_{1e} is relatively long.

2.2.2. Nuclear Hamiltonian of a Nucleus i

The interaction of the electron spin with a particular nucleus i in its vicinity is described by the nuclear Hamiltonian $\hat{H}_{N,i}$. It consists of the sum of the three terms shown in Eq. (2.20), namely the nuclear Zeeman interaction $\hat{H}_{NZ,i}$, the hyperfine[2] interaction $\hat{H}_{HF,i}$, and the nuclear quadrupole interaction $\hat{H}_{Q,i}$.

$$\hat{H}_{N,i} = \hat{H}_{NZ,i} + \hat{H}_{HF,i} + \hat{H}_{Q,i}. \tag{2.20}$$

The contribution of these terms to the nuclear Hamiltonian $\hat{H}_{N,i}$, and consequently to the ENDOR spectrum, depends on the particular kind of nucleus i, and thereby its nuclear spin I has to be considered.

Nuclear Zeeman Interaction: As already mentioned, the nuclear spin I is quantized in a magnetic field resulting in the nuclear Zeeman splitting of the nuclear spin states as

$$\hat{H}_{NZ,i} = -\mu_N \vec{B}_o \ddot{g}_{N,i} \hat{I}_i, \tag{2.21}$$

The local magnetic fields set up by the nuclear spins depend on the orientation of the nuclear magnetic moment with respect to the external magnetic field. For a given nuclear quantum number I a splitting into $2I+1$ energy levels is observed. Each level is characterized by a nuclear magnetic spin quantum number $m_I = I, I-1,...,-I$.

Hyperfine Interaction: Two mechanisms with different physical origin can contribute to the hyperfine interaction, namely the ***Isotropic Fermi Contact***

---

[2] In EPR this term is called hyperfine if the nucleus and the unpaired electron belongs to the same atom, and superhyperfine if it results from the interaction with other neighboring nuclei. However, in ENDOR, this interaction is typically referred to as hyperfine in all the cases.

interaction and the ***dipole-dipole*** interaction.

The ***Isotropic Fermi Contact*** interaction is proportional to the density of unpaired electron spin at a given nucleus. Therefore, the isotropic Fermi contact interaction plays a role if there is $s-$orbital contribution to the molecular orbital that the unpaired electron spin occupies. It can be significant when the unpaired spin resides in a $p-$, $d-$ or $f-$orbital. Spin density at the nucleus is then induced by configuration interaction or spin polarization.

The ***dipole-dipole*** interaction is caused by the interaction between the magnetic moments of the electron and nuclear spin in analogy to the classical dipolar interaction between magnetic moments. This interaction is responsible of the anisotropic component of the hyperfine interaction.

The hyperfine interaction for a nucleus i is described by the following Hamiltonian:

$$\hat{H}_{HF,i} = \hat{I}_i \vec{A}_{HF,i} \hat{S} , \qquad (2.22)$$

where $\vec{A}_{HF,i}$ is the hyperfine coupling tensor for the nucleus i.

Assuming that the electron $\vec{g}_{eff}$ tensor is diagonal and using its principal unit axis as a frame of reference, the explicit values for the components of $\vec{A}_{HF}$ taking into account both interactions, the *dipole-dipole* interaction and the *Isotropic Fermi Contact* interaction, are:

$$A_{ij} = \frac{-\mu_B \mu_N g_N}{r^3} g_i \left(3r_i r_j - \delta_{ij}\right) + A_{iso}\delta_{ij} , \qquad (2.23)$$

where r is the distance between the metal ion and the neighboring hydrogen or nitrogen atoms, r_i and r_j are components of the unit vector pointing in the direction of the electron-nuclear connecting vector, and A_{iso} is the *Isotropic Fermi Contact* constant.

Nuclear Quadrupole Interaction: The nuclear quadrupole interaction plays a role for nuclei with a nuclear spin quantum number $I > 1/2$. The physical origin of this term is the interaction of the electric quadrupole moment of these nuclei with the electric field gradient. This gradient arises from asymmetric distributions of electric charges around the nucleus. The interaction is given in the Hamiltonian by

$$\hat{H}_{Q,i} = \hat{I}_i \vec{Q}_i \hat{S} \tag{2.24}$$

where $\vec{Q}_i$ is the nuclear quadrupole tensor. In the present work, we consider only ^1H-ENDOR lines. Due to the fact that ^{14}N-ENDOR lines could not be resolved, the quadrupole interaction is neglected in the following.

2.2.3. ENDOR Spectrum of Cu^{2+} Complexes

Figure 2.7 introduces the geometry of a Cu^{2+} complex characterized by an unpaired electron spin $S = 1/2$ and a nuclear spin $I_{Cu} = 3/2$. The position of a nucleus i with respect to the Cu^{2+} complex can be described in a reference frame with principal axis of the $\vec{g}$ tensor. The magnetic field is fixed and then, the position of the nucleus i can be unambiguously determined in this frame by the angles θ_i and φ_i, and the distance r to the metal center.
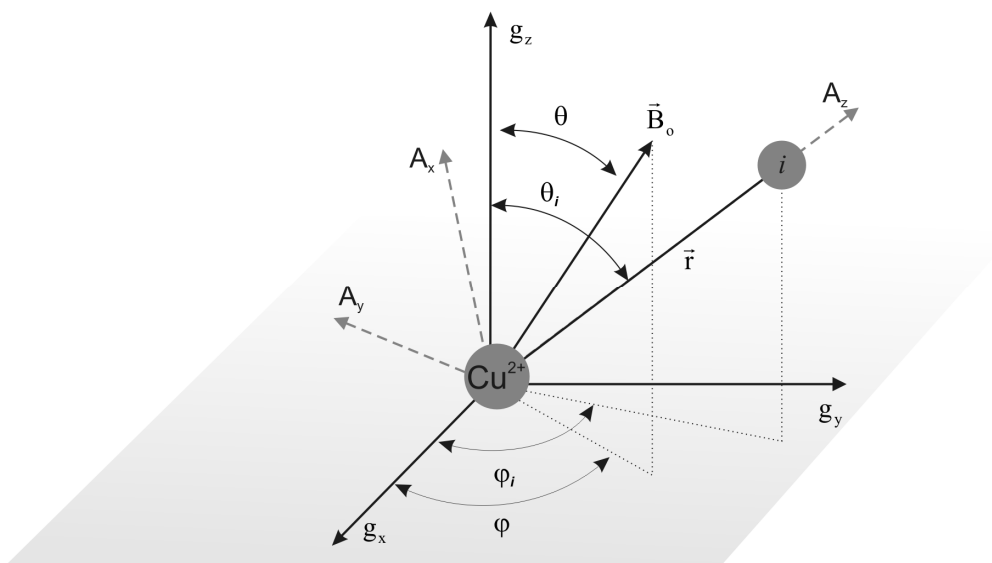
Figure 2.7: Polar coordinates of a nucleus i with respect to the Cu^{2+} complex. The position of the nucleus i can be unambiguously determined by the angles θ_i and φ_i, and the distance r to the metal center.

In the presence of an external magnetic field, the energy levels split in eight levels (shown in Figure 2.2). According to the EPR selection rules, four EPR lines are then expected for such a system. If we now consider a ^1H ($I = 1/2$) in this Cu^{2+} system, the energy levels will split further in sixteen levels as shown in Figure 2.8. NMR transitions can be induced by sweeping radiofrequency radiation through nuclear resonance transitions at a fixed magnetic field.
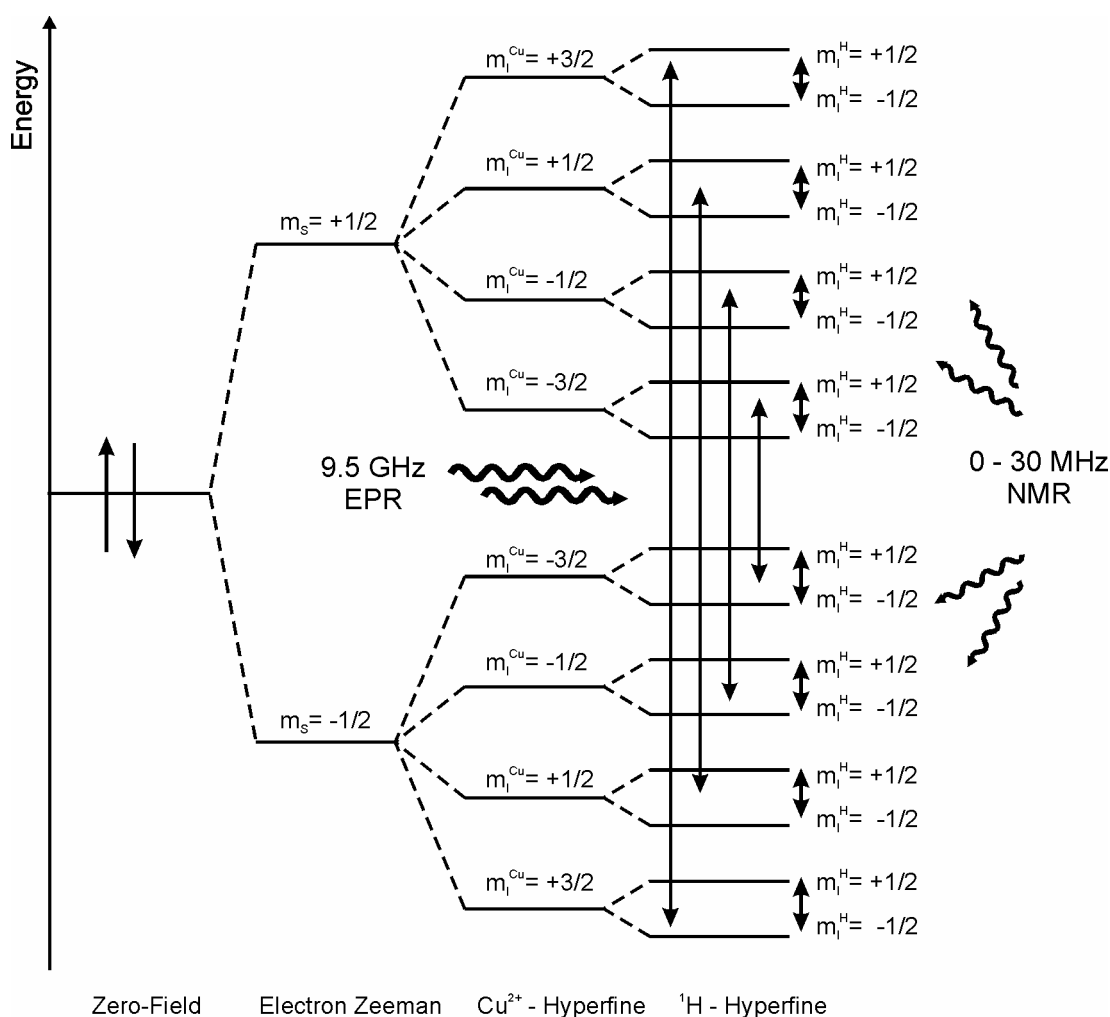
Figure 2.8: Energy scheme for the splitting of the paramagnetic spin. In an ENDOR experiment the EPR transition is saturated with 9.5 GHz radiation. Simultaneously radiofrequency radiation (0-30 MHz) excites the nuclear transitions.

EPR spectra of frozen solutions reflect an average of all molecular orientations with respect to the magnetic field. Thereby, once the magnetic field setting in an ENDOR experiment is fixed, a set of discrete molecular orientations is selected. Let us regard a Cu^{2+} complex in frozen solution, exhibiting an EPR spectrum like in Figure 2.9.

This EPR spectrum resembles typical characteristics of Cu^{2+} complex with axial symmetry and coincident axis for the $\vec{g}$ tensor and copper $\vec{A}_{Cu}$ tensor. For a fixed B_o value, which also fixes a g_{eff} value (Figure 2.3), one selects those molecules which fulfill the resonance condition in an EPR experiment.

Due to the ***dipole-dipole*** interaction, an ENDOR spectrum reflects the angular dependence of the hyperfine energies of close nuclei, like ^1H or ^{14}N. Therefore, the geometric location of a ligand nucleus can be determined. Here we consider interaction with ^1H, where the nuclear Zeeman interaction dominates the hyperfine interaction. Therefore ENDOR lines occur centered at the ^1H Larmor frequency which ranges from 12 to 14 MHz, depending upon the fixed magnetic field. In the case of ^1H resonances, the ENDOR lines are splitted exclusively by the hyperfine interaction.

Figure 2.9 shows an EPR spectrum of a Cu^{2+} complex and subsequently, the selection of an angle by the application of a magnetic field. This figure illustrates how a given field selects groups of molecules with specific molecular orientations with respect to the applied field direction.

For a Cu^{2+} complex in frozen solution with axial symmetry, the maximum hyperfine splitting occurs for a field pointing along the metal-nucleus vector (A_z axis) and the minimum when the field is near the $A_x - A_y$ plane (Hurst et al., 1985). An interpretation of ENDOR resonances at one magnetic field must be consistent with all working points, placing rigorous conditions on peak assignment and nuclear coordinates. Our ENDOR analysis only takes ^1H nuclei interactions into account. ^{14}N nuclear interactions are not taken into consideration due to their broad signal and bad signal-to-noise ratio in our experiments.
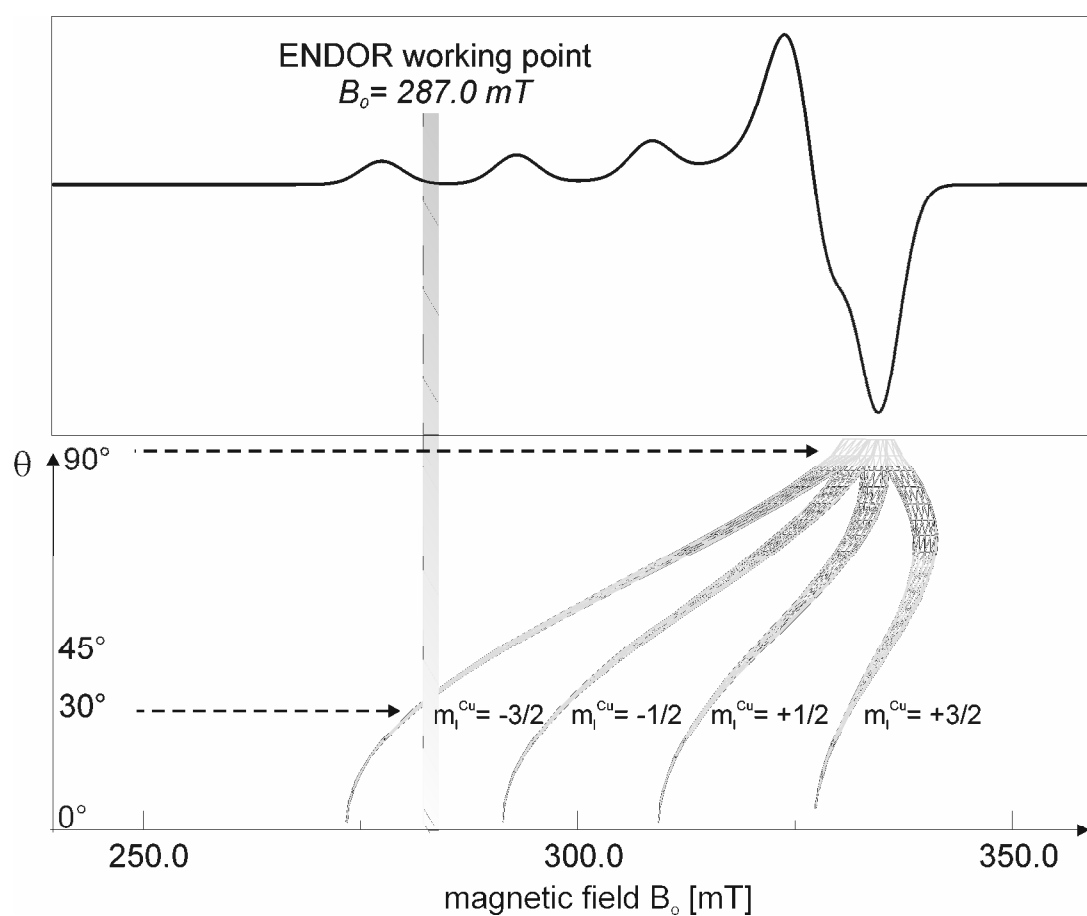
Figure 2.9: Selection of molecules according to their orientation θ to the magnetic field. The magnetic field value, for instance $B_o = 287.0$ mT, determines an ENDOR working point. In this case only molecules with θ=30° contribute to the ENDOR spectrum.

2.3. Extended X-ray Absorption Fine Spectroscopy

2.3.1. Absorption of X-rays in Matter

At the energy regime of X-rays, radiation is absorbed by all matter via the photoelectric effect. During this process, an X-ray photon can be absorbed by a core electron of an atom if the photon energy is greater than the binding energy. If absorption of the X-ray photon occurs then, the energy excess of the electronic binding energy is given to a photo-electron that is ejected from the atom.

X-ray absorption is usually expressed in terms of the absorption coefficient μ which manifests the attenuation of X-ray upon their passage through matter according to Beer's Law:

$$I = I_o \, \mathrm{e}^{-\mu \cdot t}, \tag{2.25}$$

where I_o is the X-ray intensity incident on a sample, t is the sample thickness, and I is the intensity transmitted through the sample.

The absorption coefficient μ is a decreasing function of energy which depends upon the sample density ρ, the atomic number Z, the atomic mass A and the X-ray energy E as

$$\mu \approx \frac{\rho Z^4}{AE^3}. \tag{2.26}$$

Since synchrotron facilities allow us to control the energy of X-rays, it is possible to tune the incident radiation at about the binding energy of certain electronic core level of an atom. The absorption coefficient varies as a decreasing function of the photon energy of the X-ray following Eq. (2.26) unless an absorption edge occurs where the photon energy is just sufficient to excite a core electron of the absorbing atom to the continuum and then, a sharp rise in absorption occurs. In the Sommerfeld's notation, the absorption edges are labelled by K, L_I, L_{II}, etc., corresponding to the excitation

of an electron from the $1s$, $2s$, $2p$, etc., orbitals respectively. A schematic illustration of this process is shown in Figure 2.10.
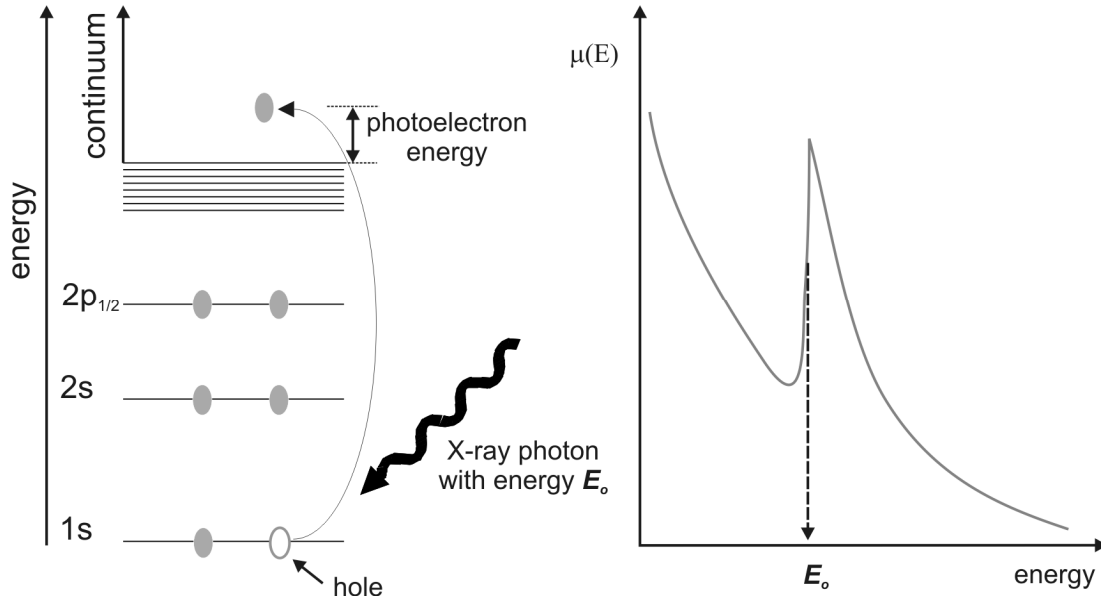
Figure 2.10: Excitation of a core electron due to the absorption of an X-ray photon with energy E_o. The corresponding absorption coefficient function is shown in the right side of the figure.

Following an absorption event, the atom is said to be in an excited state, with a core hole and a photo-electron. The excited state will decay through two main mechanisms: either X-ray fluorescence or Auger effect. In the first process, a core electron from a higher energy level than the core hole fills the vacant emitting fluorescent radiation with a well defined energy corresponding to the energy difference of the core levels where it originates. If Auger effect occurs, an electron drops from a higher electron level and a second electron is promoted into the continuum. Either of these processes can be used to measure the absorption coefficient μ, though X-ray fluorescence dominates in the hard X-ray regime with energies greater that 2 keV.

The energy dependence of the absorption coefficient μ can be determined either in transmission, regarding Eq. (2.25), as

$$\mu(E) = \frac{1}{t}\ln\left(\frac{I_o}{I}\right) \tag{2.27}$$

or in X-ray fluorescence (or Auger emission) mode as

$$\mu(E) \propto \frac{I_f}{I_o} \tag{2.28}$$

where I_f is the intensity of the fluorescence line (or electron emission in the case of Auger effect) associated with the absorption process. Figure 2.11 shows a schematic representation of the transmission and fluorescence experiments where the intensities involved are shown.
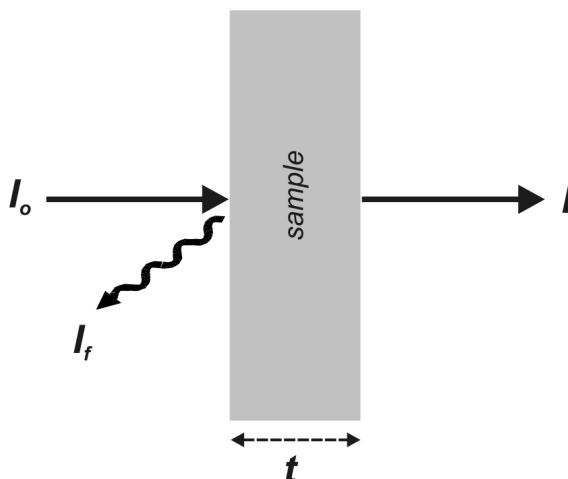
Figure 2.11: Simplified drawing of the transmission and fluorescence experiments in a sample of thickness *t*.

In the case of an isolated atom, the coefficient μ decreases monotonically as a function of the energy beyond the edge. However, atoms embedded in a molecule or in a condensed phase exhibit an oscillation in the absorption coefficient which depends on the environment of the absorbing atom. The X-ray absorption process generates photoelectrons that in good approximation can be considered as spherical waves. Thus, the ongoing photoelectron wave can be backscattered from the surrounding atoms as shown in Figure 2.12. As the kinetic energy of the ejected photoelectron increases, the outgoing and backscattered photoelectron wave will interfere. This interference will induce variations in the electron density of the absorbing atom, which depends on the energy of the ejected photoelectron.

Constructive interference will increase the electron density and increase the provability of the photon to be absorbed. Therefore, a change in interference from destructive to constructive will give rise to the oscillations in the absorption after the edge.
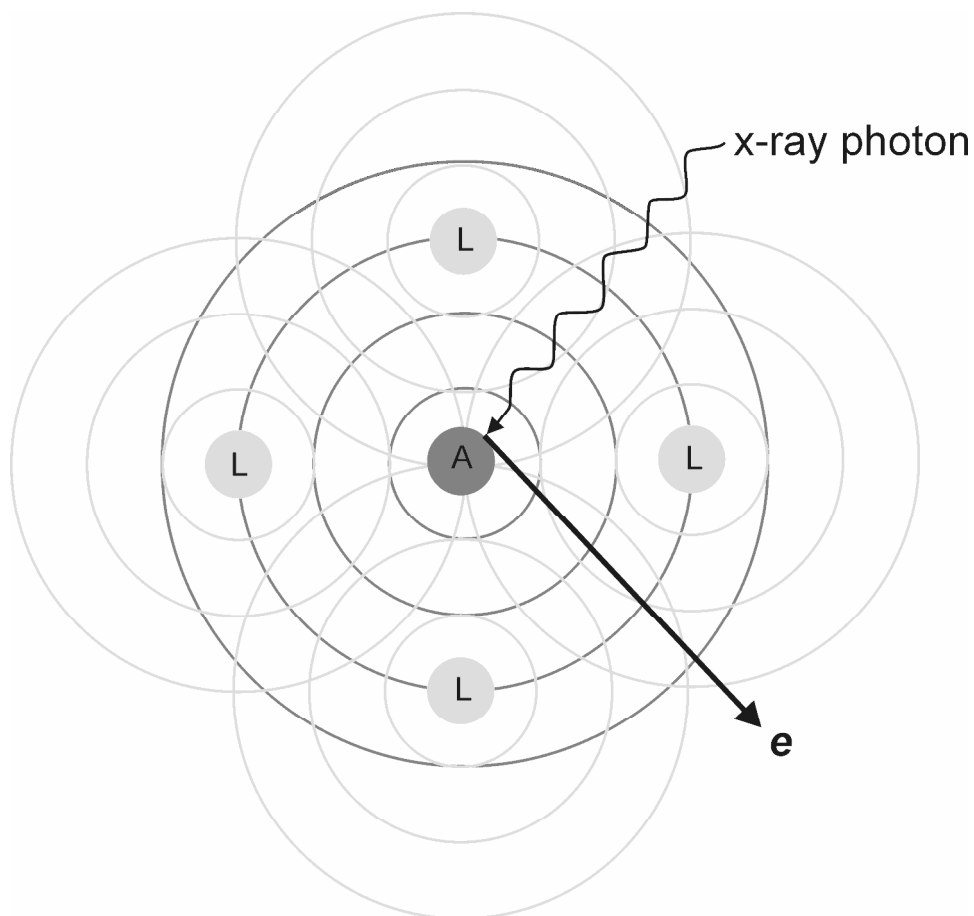
Figure 2.12: Schematic representation of the absorption of a X-ray photon by an absorber **A.** An electron ***e*** is ejected from the core absorbing level. The outgoing and backscattered waves (due to the four neighbors **L**) interfere, and produce the modulation of the absorption coefficient μ.

2.3.2. Absorption Edge Structure

X-ray absorption spectra can be divided into two major regions with respect to its relative position to the edge, specifically to the threshold energy E_o. They are traditionally referred to as X-ray Absorption Near Edge Structure (XANES) and

Extended X-ray Fine Structure (EXAFS). For the particular case of the K_α edge of a biological sample with Cu^{2+}, Figure 2.13 displays the XANES and EXAFS regimes.
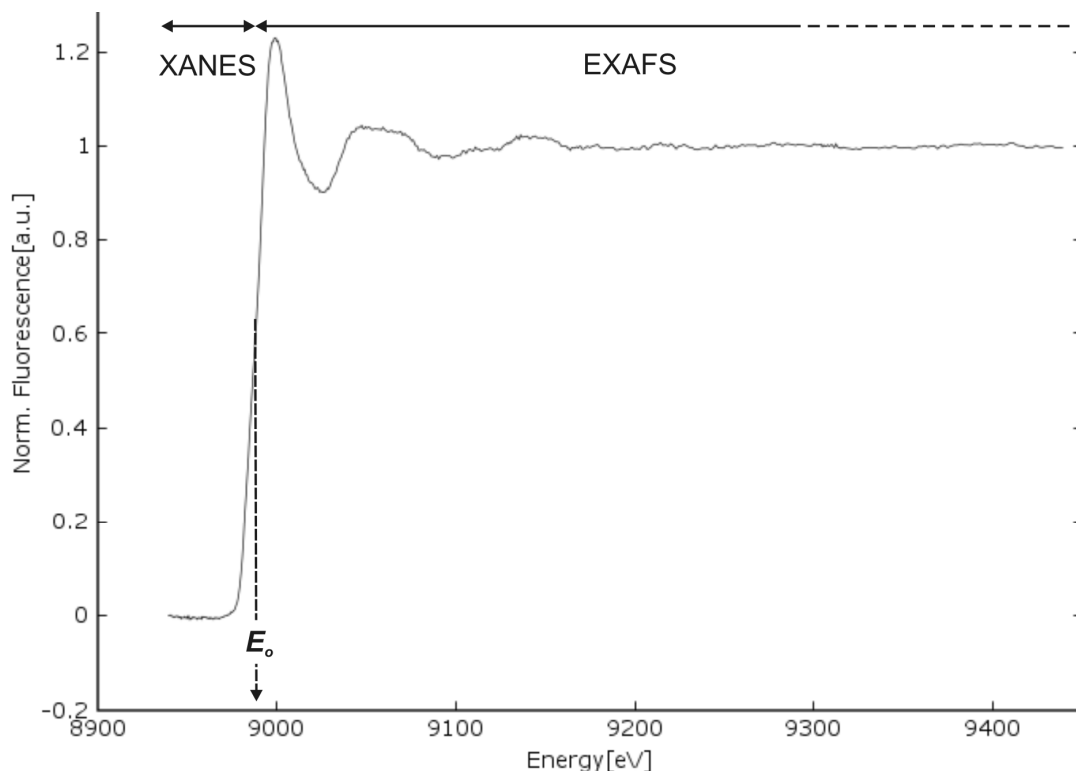
Figure 2.13: Normalized absorption edge in fluorescence mode of a Cu^{2+} biological sample. The XANES and EXAFS regimes are delimited by arrows.

Within the XANES regime, the absorption coefficient μ is sensitive to oxidation state and coordination geometry (e.g., octahedral, tetrahedral coordination). Electronic transitions from a core level to unoccupied states give rise to a series of pre-edge features up to the top of the absorption edge where frequently, there is a sharp line due to transitions to states near the continuum. Since these energy levels are closely spaced, the probability of absorption will increase. The pre-edge features can give information about the coordination geometry of the absorbing atom that is influenced by the energy levels in the valence shell. The edge position is influenced by the oxidation state of the absorbing atom because changes of the oxidation state affect the potential energy of the electron. After the top of the edge up to about 50 eV above E_o, intense spectral features appear due to scattering of photoelectrons ejected with relatively low kinetic energy. In this region multiple scattering and relatively

long pathways involving tightly bonded atoms beyond the first shell can give significant contributions.

The EXAFS regime extends from energies about 50 eV up to more than 1000 eV above E_o. The EXAFS region usually exhibits weak oscillations of the absorption coefficient μ which arise from backscattering of high energy photoelectrons, mostly in single backscattering processes. The EXAFS features can be used to determine distances, coordination number, and species of the neighbours of the absorbing atom.

Nowadays, XANES and EXAFS have become a powerful and versatile structural probe, especially for structural analyses of chemical and biological systems where diffraction methods are not applicable. Note that crystals are not required for such as X-ray absorption techniques, making them one of the few structural probes available for noncrystalline and highly disordered material, including solutions.

In the course of this work, EXAFS spectroscopy has been extensively used in a number of biological samples. However, XANES analyses were restricted to inspection of the oxidation state and edge consistency.

2.3.3. EXAFS formula

X-ray absorption involves the photo-induced transition of a core electron from an initial state $|i\rangle$ to a final state $|f\rangle$ where a core hole and a photoelectron are generated. The theoretical calculations of X-ray absorption are based on the Fermi's golden rule within the dipole approximation and thus, the absorption coefficient $\mu(E)$ can be described as follows:

$$\mu(E) \propto \left| \left\langle f \left| \vec{\varepsilon} \cdot \vec{r} \right| i \right\rangle \right|^2 \tag{2.29}$$

where $\vec{\varepsilon}$ is the polarization vector of the electron field and $\vec{r}$ represents the electron coordinates. The condition for the validity of the dipole approximation is that the wavelength of the photons must be greater than the size of the initial core electron. This condition is well satisfied even for light atoms and less tight bound core electrons.

The oscillations responsible of the EXAFS can be defined as an energy function as

$$\chi(E) = \frac{\mu(E) - \mu_o(E)}{\Delta\mu_o(E)}$$ (2.30)

where $\mu(E)$ is the measured absorption coefficient, $\mu_o(E)$ is a smooth background function representing the absorption of an isolated atom, and $\Delta\mu_o(E)$ is the measured jump in the absorption $\mu(E)$ at the threshold energy E_o.

The EXAFS manifests the wave behaviour of the ejected photoelectron and therefore, it is commonly expressed in terms of the wave number of the photoelectron k which is defined as

$$k = \sqrt{\frac{2m(E - E_o)}{\hbar^2}}$$ (2.31)

where m refers to the electron mass.

The EXAFS oscillation $\chi(k)$ decays very fast with k and therefore, $\chi(k)$ is often multiplied by a power of k to emphasize the oscillations. A number of frequencies can be deciphered from the $\chi(k)$ oscillations corresponding to different neighbour coordination shells. Then, the distances, coordination number, and species of the neighbours of the absorbing atom can be described and modelled according to the standard EXAFS formula (Sayers et al., 1971) as follows:

$$\chi(k) = S_o^2 \sum_j N_j \frac{|f_j(k)|}{kR_j^2} \sin\left[2kR_j + \phi_j(k) + 2\delta_c\right] \cdot e^{2R_j/\lambda(k)} e^{-2\sigma_j^2 k^2}$$ (2.32)

in which the sum runs over a number of j atoms around the absorber. For each shell, N_j, R_j, and σ_j^2 represent the coordination number, the average coordination distance, and the mean square relative displacement which accounts for thermal vibration and static disorder respectively. The parameters $\left|f_j(k)\right| \cdot e^{i\phi_j(k)}$ and δ_c are the backscattering amplitude and the absorber phase shift of the final state. Since the backscattering amplitude depends on the atomic number Z of the neighboring atom

j, EXAFS is also sensitive to the atomic species surrounding the absorbing atom. The parameter $\lambda(k)$ represents the photoelectron mean free path. The overall amplitude factor S_o^2 is a many-body effect due to the relaxation of the system in response to the creation of the core hole. Although S_o^2 is weakly energy dependent, it is usually approximated by a constant.

In Eq. (2.32), the dependence of EXAFS oscillations on interatomic distances and energy is clearly reflected by the term $\sin(2kR)$. The term $e^{-2R/\lambda(k)}$ contemplates the general decay of the wave due to the mean free path or finite lifetime of the photoelectron. This factor is largely responsible for the relatively short range of EXAFS spectroscopy. The strength of the reflected interfering waves depends on the type and number of neighbouring atoms through the backscattering amplitude $\left|f_j(k)\right|$, and hence is primarily responsible for the magnitude of the EXAFS signal. The $1/kR_j^2$ and $\lambda(k)$ factors are secondary but also important for the quantitative behavior of the EXAFS amplitude. The effect of the term $e^{-2\sigma^2 k^2}$, usually referred as Debye-Waller factor, is more pronounced at large values of the photoelectron energy and hence, it cuts off the the EXAFS at about $k \approx 1/\sigma$ beyond the edge. Moreover, since σ^2 generally increases with temperature, the EXAFS oscillation tends to become less intense at high temperatures. Therefore, the EXAFS is confined to successively lower regions of energy with increasing temperatures.

The standard EXAFS formula described by Eq. (2.32) contains all the elements that a plausible theory of EXAFS should include and also provides a convenient parameterization for fitting the local atomic structure around the absorbing atom to the experimental data. Furthermore, the formula shown in Eq. (2.32) can be generalized for multiple scattering processes (Rehr and Albers, 1990), although the original EXAFS formula referred only to single scattering processes. For multiple scattering processes, some parameters have to be reformulated such as R_j, σ_j^2, $\left|f_j(k)\right|$, $\phi_j(k)$ and δ_c. Therefore, R_j represents the full length of the multiple scattering path, σ_j^2 additionally holds effects of the distribution of scattering angles,

and the backscattering amplitude and phase shifts are now more complicated expressions describing each scattering event along the multiple scattering path.

Experimental Setup

3

3.1. EPR and ENDOR Instrumentation

Continuous wave EPR and ENDOR measurements at X-band (frequencies around 9.5 GHz) were performed on an EleXsys580 spectrometer. The different components of this spectrometer are given in Table 3.1.

Components	Description of components
Bruker ESP 380-1010	Microwave bridge up to maximum 200 mW, X-band
Bruker Elexys	Electronic control system
Bruker ER083CS	Transformer for the operation of the magnets
ENI A-500RF Power Amplifier	0.3-35 MHz radiofrequency amplifier
Bruker 4102 ST 9717	EPR standart resonator
Bruker EN 801	ENDOR resonator
Oxford ESR 910	Cryostat for Bruker 4102 ST 9717 and Bruker EN 801
Xepr	Bruker software for data acquisition

Table 3.1: Components of the spectrometer EleXsys580 for EPR and ENDOR measurements.

EPR spectra were acquired using a standard resonator Bruker 4102 ST 9717 equipped with a TE_{102} cavity (Bruker). Unless otherwise specified, all EPR measurements were collected at 77 K, within a sweep width of 1200 G, modulation amplitude of 3 G and microwave power of 0.2001 mW. The temperature was measured by a thermocouple against liquid nitrogen 77 K and controlled by an ITC 4 temperature controller from Oxford Instruments. The program package Xemr was used to simulate EPR spectra (compare: http://www.epr.chem.jyu.fi/xemr/).

For the ENDOR measurements the spectrometer was equipped with Bruker EN 801 resonator with a radiofrequency (RF) coil fixed within the cavity on the outer wall of

a doubly walled quartz Dewar flask. In order to reduce contributions to the fields from mixing frequencies, the RF field produced by the coil is chosen perpendicular to the microwave field in the resonator. ENDOR spectra were recorded at 17 K with a microwave power of 6.006 mW, a radio frequency power of 1dB at a maximum power output of 500W, and a RF modulation amplitude of 300 KHz. The equipment for temperature adjustment and control is equivalent to the one used in EPR measurements.

Figure 3.1 shows schematically the setup for an EleXsys580 spectrometer (Brucker) where the components of Table 3.1 are depicted as blocks.
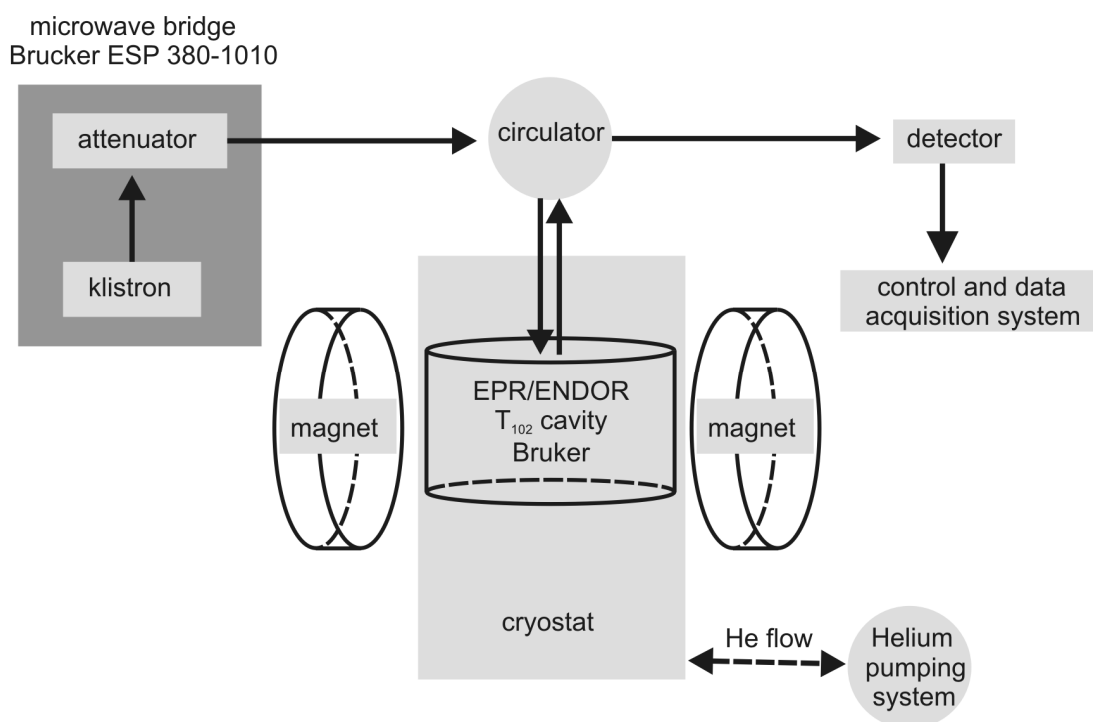
Figure 3.1: Schematic representation of the EPR/ENDOR setup.

In an EPR experiment the microwave source, or Klystron, produces approximately 200 mW of microwave power. These microwaves propagate inside of the waveguide to an attenuator and then, continue to a circulator. Then the microwaves are directed to the microwave cavity, which is located between the pole faces of a large magnet. The reflected microwaves return to the circulator toward the detector.

During an ENDOR experiment, an EPR transition is driven at resonance and saturated and therefore, the EPR setup shown in Figure 3.1 can be used. However, a RF coil must be placed inside the microwave cavity to excite NMR transitions.

Regarding the samples studied in the present work, data acquisition of one EPR spectrum takes about three hours. In this period of time, the parameters for data acquisition and the tuning of the spectrometer remain about constant. However, for ENDOR measurements data acquisition takes much longer time, specially for working points at the low magnetic field region where the signal to noise ratio is very weak. Therefore, in order to collect an acceptable ENDOR spectrum, several scans have to be taken, and the cavity tuning must be periodically inspected. In these cases, data acquisition of one single spectrum takes about 12 hours.

3.2. EXAFS Instrumentation

EXAFS experiments were performed with synchrotron radiation at the D2 bending magnet beam line of the European Molecular Biology Laboratory (EMBL) Outstation Hamburg at Deutsches Elektronen Synchrotron (DESY). Figure 3.2 shows a schematic representation of this experimental setup. This spectrometer is specifically suited for X-ray absorption measurements on biological and other dilute systems. The storage ring DORIS was operating at an energy of 4.5 GeV with a positron current between 90 to 145 mA. A Si[111] double monochromator with focussing mirrors selected energies around the copper K-edge. Bragg-reflections of a Si[220] crystal were used for the energy calibration (Pettifer and Hermes, 1985). The measurements were performed at 35 K. A Canberra 13-element fluorescence detector was used to collect the copper K_α-fluorescence. All the constituent elements of the EXAFS setup are listed in Table 3.2.

Instrument Specification

Source [4.5 GeV]	Bending magnet Ec = 16.6 keV Beam size1.3 x 4.4 mm at full-width half-maximum (FWHM) Vertical electron beam divergence 0.06 mrad FWHM
Monochromator	Si[111] double crystal monochromator, temperature controlled, harmonic rejection by detuning and active feedback control. Relative energy resolution $\delta E/E = 14\cdot10^{-5}$
Mirror	Toroidal, 4 segments, total length 1800 mm, gold coated, angle of incidence = 3.8 mrad, cut-off energy = 21.5 keV
Beam size at sample	5.0 mm x 1.5 mm
Energy range	5.0 keV to 30.0 keV unfocused; 5.0 keV to 21.0 keV focused
Detectors	2 ionization chambers, 13 element solid state detector
Cryostat	2-stage Displex, T_{min} = 17K, with He exchange gas
Energy calibrator	Static Si[220] crystal and detectors to record Bragg peaks in back reflection geometry (precision ~ 0.1 eV)

Table 3.2: Instrument specification of the D2 beam line at EMBL-Hamburg (reproduced from: http://www.embl-hamburg.de/services/xas).

The total measuring time was divided into several scans taking between 30 and 45 min. The standard procedures of the EMBL were used for the data reduction (Nolting and Hermes, 1992). The k^3-weighted Cu^{2+} EXAFS spectra $\chi(k)$ were refined with software package EXCURV 9.262 (Binsted et al., 1992). Phase shifts and scattering amplitudes were computed according to (Rehr and Albers, 1990).
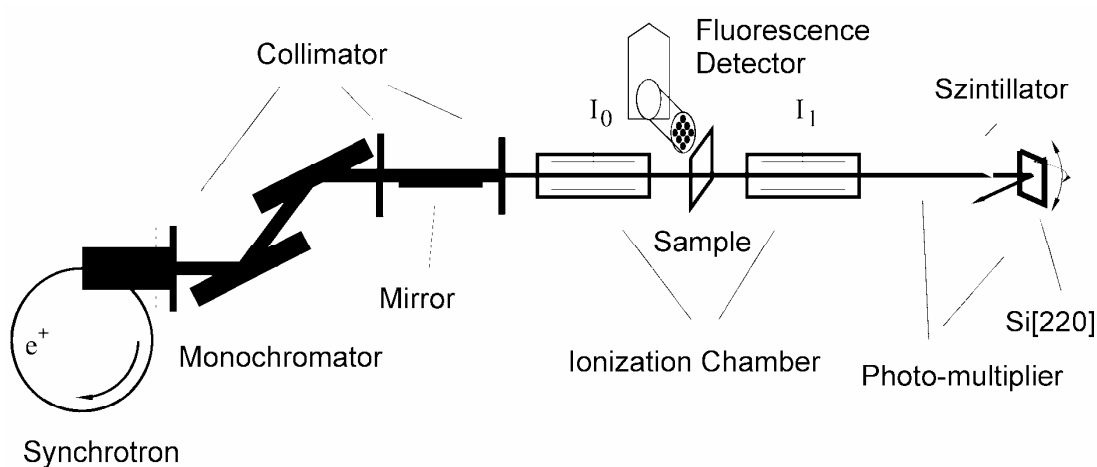
Figure 3.2: Schematic representation of the D2 beam line at EMBL-Hamburg.

Sample Preparation

4

Table 1 summarizes the main characteristics of all the sample preparations investigated in the current work. In addition, for each of these samples, the applied spectroscopic methods are specified.

sample	peptide	Cu^{2+}equiv.	buffer	pH	EPR	ENDOR	EXAFS
pentapeptide	hPrP(61–65)	1.0	*a*	6.5	✓	✗	✗
pentapeptide	hPrP(61–65)	1.0	*a*	7.0	✓	✗	✗
pentapeptide	hPrP(61–65)	1.0	*a*	7.5	✓	✓	✗
octapeptide	hPrP(60–67)	1.0	*a*	6.5	✓	✗	✗
octapeptide	hPrP(60–67)	1.0	*a*	7.2	✓	✓	✓
tetraoctapeptide	hPrP(60–91)	1.0–4.0	*a*	7.5	✓	✗	✗
tetraoctapeptide	hPrP(60–91)	1.0	*b*	7.5	✓	✓	✗
tetraoctapeptide	hPrP(60–91)	2.0–3.0	*b*	7.5	✓	✗	✗
tetraoctapeptide	hPrP(60–91)	1.0–4.0	*c*	7.5	✓	✗	✗
tetraoctapeptide	hPrP(60–91)	1.0–3.0	*d*	7.5	✓	✗	✗
tetraoctapeptide	hPrP(60–91)	4.0	*d*	7.5	✓	✓	✓
hPrP	hPrP(23–231)	1.3	*e*	6.0	✗	✗	✓
hPrP	hPrP(23–231)	1.7	*e*	6.0	✓	✗	✓
hPrP	hPrP(23–231)	2.7	*f*	7.0	✓	✓	✓
mut-HG MmPrP	MmPrP(23–231)[3]	1	*d*	7.5	✓	✓	✗

Table 4.1: Cu^{2+} equivalents, pH values, buffer and applied spectroscopic methods are given for each sample. The different buffers are identified by letters *a* through *f*, where *a*: 25mM N-ethyl-morpholine (NEM), 150 mM KCl, 20 % glycerol; *b*: 100 mM ammonium acetate buffer containing dodecylphosphocholine (DPC) micelles at a peptide/detergent ratio of 1:100; *c*: 10 mM sodium phosphate buffer containing DPC micelles at a peptide/detergent ratio of 1:100; *d*: 10 mM 3-N-morpholinopropanesulfonic acid (MOPS), 20% glycerol *e*: 10mM 2-morpholinoethanesulfonic acid (MES); *f*: 10 mM 3-N-morpholinopropanesulfonic acid (MOPS).

---

[3] mutant of the recombinant murine PrP(23-231) where the histidine residues from the octarepeat domain were substituted with glycine residues.

4.1. PrP-derived Peptides

Peptide synthesis

The pentapeptide, octapeptide and tetraoctapeptide corresponding respectively to the sequences 61-65, 60-67 and 60-91 of the recombinant human PrP^C were synthesised in the N-acetylated and C-amidated form to avoid end group effects and thus, to properly mimic this sequence portion in the intact protein as described previously (Renner et al., 2004).

Sample preparation

^{63}CuO from Chemotrade was stirred in 6 M HCl for 3 h at room temperature. Then, the solution was filtered on Millex-GV 0.45 μm and the aqueous layer was lyophilized to yield ^{63}CuCl$_2$ in quantitative amounts. During the sample preparation process, suitable amounts of ^{63}CuCl$_2$ were added to assure the corresponding peptide/Cu^{2+} ratio. Note that the pure isotope ^{63}Cu was used to avoid inhomogeneous broadening of the EPR lines that would otherwise be present with the mixture of naturally occurring isotopes ^{63}Cu and ^{65}Cu.

For all the following preparations, concentrations of PrP-derived peptides were determined by weight and peptide content. The pH adjustments were performed by addition of 0.5 M NaOH or 0.5 M HCl and equilibration of the solutions for 24 h.

Samples of 1 mM **pentapeptide** and **octapeptide**, and their corresponding 1:1 Cu^{2+} complexes, were prepared in 25mM N-ethyl-morpholine (NEM), 150mM KCl and 20% glycerol (*buffer a*).

Samples of **tetraoctapeptide** were prepared in four different buffer systems, identified by letters *a* to *d*. Within each kind of buffer preparation, the Cu^{2+} contents were as follows:

- *Buffer a*: Samples of 0.106 mM tetraoctapeptide and their 1:(1−4) peptide-Cu^{2+} complexes were prepared in 25 mM N-ethyl-morpholine (NEM), 150mM KCl and 20% glycerol.

- *Buffer b:* Samples of 0.80 or 0.35 mM tetraoctapeptide and their 1:1 or 1:(2−

3) peptide–Cu^{2+} complexes were prepared in 100 mM ammonium acetate buffer containing DPC-d_{38} (Eurisotop, France) at a peptide/detergent ratio of 1:100.

- *Buffer c:* Samples of 0.35 mM tetraoctapeptide and their 1:(1–4) peptide–Cu^{2+} complexes were prepared in 10 mM phosphate buffer containing 35 mM DPC-d_{38} (Eurisotop, France) resulting in a peptide/detergent ratio of 1:100.

- *Buffer d:* Samples of 0.8, 0.6, 0.4, 0.2 mM tetraoctapeptide and respectively, their 1:(1–4) peptide–Cu^{2+} complexes, were prepared in 10 mM 3-N-morpholinopropanesulfonic acid (MOPS) and 20% glycerol.

4.2. Recombinant Human PrP(23–231)

Sample preparation

Recombinant PrP(23–231) was produced and purified essentially as described previously by Giese (Giese et al., 2004). Fractions containing purified PrP were pooled, concentrated with a centriprep device and finally diluted 1:50 for refolding into 10 mM MES at pH 6.0. Solutions of refolded PrP were stirred at 4 °C for 4 to 12 hours and aggregates removed by centrifugation for 30 min at 17000 rpm in a Beckmann JA-17 rotor at 4 °C. Supernatants were concentrated again using centriprep YM10 ultrafiltration cells and cleared from aggregates by centrifugation at 16000 x g for 30 min at 4 °C. PrP was finally dialysed against 2 mM MES (pH 6.0) to remove traces of urea and imidazole. The native fold of purified PrP was confirmed by CD spectroscopy using a Jasco 750 CD-spectrophotometer. Absence of chelators like EDTA and imidazole was confirmed by NMR spectroscopy.

Dialyzed solutions of 50-100 µM PrP at pH 6.0 were supplemented with crystalline $^{63}CuCl_2$ to yield a molar ratio of 5:1 of $^{63}Cu^{2+}$ to PrP. Solutions were kept on ice for 1 h then centrifuged for 30 min at 16000 x g and 4 °C. For the precipitation of PrP/Cu^{2+} complexes under varying pH conditions the supernatants were either supplemented with 100 mM MOPS at pH 7.0 directly before addition of ammonium sulfate or the complexes were directly precipitated by addition of solid ammonium

sulfate to a saturation of 90 %. Precipitation was performed overnight on ice before the protein was pelleted by centrifugation for 30 min at 16000 x g and 4 °C. Pellets were then resuspended in minimal volumes of either 10 mM MOPS at pH 7.0 (*buffer f*) or 10 mM MES at pH 6.0 (*buffer e*) and transferred into appropriate sample holders for EPR or EXAFS measurements. Protein concentrations of PrP were determined by absorption measurements at 280 nm. An extinction coefficient of 56590 M^{-1} cm^{-1} was used for calculation of the protein concentration.

In addition, a soluble hPrP/^{63}Cu complex was prepared as follows: hPrP at a concentration of 0.7 mM was mixed in *buffer e* at pH 6.0 with ^{63}CuCl$_2$-solution of pH 6.0 at a molar ratio of 1:5 of hPrP to ^{63}Cu^{2+}. The solution was kept on ice for 1 h then centrifuged for 30 min at 16000 x g and 4 °C. The supernatant was dialysed exhaustively against 2 mM MES at pH 6.0. The remaining copper concentration in the dialysed sample was determined by inductively coupled plasma mass spectroscopy (ICP-MS).

Determination of copper concentrations

ICP-MS on diluted samples was done on a Elan 6100 mass spectrometer (Perkin–Elmer, Sciex, Toronto, Canada) with external calibration by multi-element standards (Merck, Darmstadt, FRG) and an internal ^{103}Rh standard (final concentration 10 µg/l). The mass spectrometer combined with a conventional cross flow nebulizer, a peristaltic pump for sample introduction, and an AS-90plus autosampler (Perkin-Elmer), an RF power of 1200 W, a sample uptake of 1 ml/min and wash time of 80 s after each sample, a nebulizer gas flow of 0.9 l/min, and a dwell time per mass of 80 ms with 50 scans per sample and five replicates were employed for the simultaneous detection of ^{63}Cu, ^{65}Cu, ^{55}Mn, ^{57}Fe, and ^{66}Zn isotopes.

It should be emphasized here, that only for the soluble hPrP(23–231) copper complex a direct measurement of the copper content was possible (ICP-MS gave a value of 1.3 Cu^{2+} per hPrP). For the precipitated samples however, the amount of copper in the pellets has to be calculated by subtraction of the concentration measured for the supernatant from that of the entire samples before precipitation. Especially at pH 7.0,

where unbound copper precipitates as copper hydroxide, a certain amount of precipitated copper hydroxide can be carried over into the sample. Therefore the obtained values (1.7 and 2.7 Cu^{2+} per hPrP) are upper limits.

4.3. Mutant HG MmPrP(23–231)

The mutant HG of the murine PrP(23–231) was produced and purified essentially as described by Giese (Giese et al., 2004). The bacterial expression in BL21DE3 RIL *Escherichia coli* cells (Novagen), which was transformed with plasmids pET17b-MmPrP23-231HG clone 27, was carried out as originally described by Liemann (Liemann and Glockshuber, 1999). Briefly, bacterial liquid cultures were grown to an optical density of 0.5 at 600 nm before protein production was induced by addition of 1 mM IPTG. Cells were harvested two hours later. Then bacteria were lysed by addition of 0.5% Triton X-100 to the lysis buffer and incubation for 30 min at 37 °C. The initial purification by centrifugation, washing with detergents, and the ion-exchange chromatography were done as previously described (Giese et al., 2004). The partially purified mutant MmPrP was subjected to oxidation as described and oxidation was terminated by addition of 0.1 mM EDTA and adjustment of pH to about 7.0. Up to 50 mg of the mutant HG MmPrP were applied to a gel chromatography column (Sephadex S-75 HighPrep16-26, Pharmacia) equilibrated with buffer containing 8 M urea, 10 mM Mops (pH 7.0), and 150 mM NaCl. Fractions containing purified mutated PrP were pooled, concentrated with a centriprep device, and finally diluted 1:50 for refolding into 10 mM MES, pH 6.0. Solutions of refolded mutant PrP were stirred at 4°C for 4–12 h and aggregates were removed by centrifugation for 30 min at 17,000 rpm at 4°C. Supernatants were concentrated again using centriprep YM10 ultrafiltration cells (Millipore) and cleared from aggregates by centrifugation at 16,000g for 30 min at 4 °C. Mutant PrP was finally dialyzed against 2 mM MES, pH 6.0, to remove traces of urea and imidazole. Correctness of the α-helical fold of purified PrP was checked by CD-spectroscopy using a Jasco 715 CD-spectrophotometer. Protein concentrations of PrP were determined by absorption measurements at 280 nm.

Dialysed solutions of 50-100 µM of the mutant HG MmPrP at pH 6.0 were supplemented with crystaline $^{63}CuCl_2$ to yield a molar ratio of 1:1 of $^{63}Cu^{2+}$ to mutated PrP. Solutions were kept on ice for 1 h then centrifuged for 30 min at 16000 x g and 4 °C. For the precipitation of mutant-PrP/Cu^{2+} complexes, the supernatants were supplemented with 100 mM MOPS (pH 7.5) directly before addition of ammonium sulfate to a saturation of 90 %. Precipitation was performed overnight on ice before the protein was pelleted by centrifugation for 30 min at 16000 x g and 4 °C. Pellets were then resuspended in minimal volumes of a buffer containing 10 mM MOPS (pH 7.5) and 20% glycerol (*buffer d*), and transferred into appropriate sample holders for EPR or EXAFS measurements.

Experimental Results

5

The Cu^{2+} binding sites of the recombinant human full-length PrP(23–231) in a number of preparations, the mutant HG of murine full-length PrP(23–231), as well as several synthetic peptides based on the amino acid sequence of the N–terminal part of hPrP, were investigated by means of EPR, ENDOR, and EXAFS (Table 4.1[4]).

5.1 EPR results

EPR spectroscopy is a powerful technique to characterize the electronic structure of paramagnetic metal centers in metalloproteins. It has been widely used to analyze copper proteins. In a continuous wave ERP experiment, the unpaired electron spin of the Cu^{2+} interacts with the magnetic field and the surrounding nuclear spins. This generates a spectrum with a characteristic pattern that resembles coordination ligands and geometry of the Cu^{2+} complex. EPR spectroscopy is very sensitive to changes in the electronic configuration of a Cu^{2+} center. Note that the pure isotope ^{63}Cu was used to avoid inhomogeneous broadening of the EPR lines that would otherwise be present with the mixture of naturally occurring isotopes $^{63}Cu^{2+}$ and $^{65}Cu^{2+}$. In the samples studied here, EPR measurements turned out to be very helpful to identify species derived from different Cu^{2+}-configurations. In several samples and at different conditions, we found mixtures of molecules belonging to different Cu^{2+} configurations. However, we succeeded in the preparation of samples where the corresponding EPR spectra exhibit solely a well defined species type that can be linked to a particular Cu^{2+} configuration. Figure 5.1 shows the selected EPR spectra of the octapeptide–Cu^{2+} in NEM buffer at pH 7.2 (A) and the tetraoctapeptide-Cu^{2+} in ammonium acetate buffer containing DPC at pH 7.5 (B). The relatively small line widths and the good agreement with the simulated spectrum lead to the conclusion that these samples contain two well distinguishable Cu^{2+} configurations, referred to

---

[4] Chapter 4: Sample Preparation

as species I and II. The two distinct species show the typical features of square-planar type 2 Cu^{2+}–complexes. Due to the interaction of the unpaired electron spin of the Cu^{2+} and its nuclear spin $I = 3/2$, the hyperfine pattern of each species exhibits three of the four hyperfine transitions in the parallel region of the spectra (low-field range) while the fourth component ($m_I = -3/2$) is masked by overlap with the hyperfine transitions in the perpendicular region and with "extra absorption" features towards the high-field end of the spectra (Peisach and Blumberg 1974).
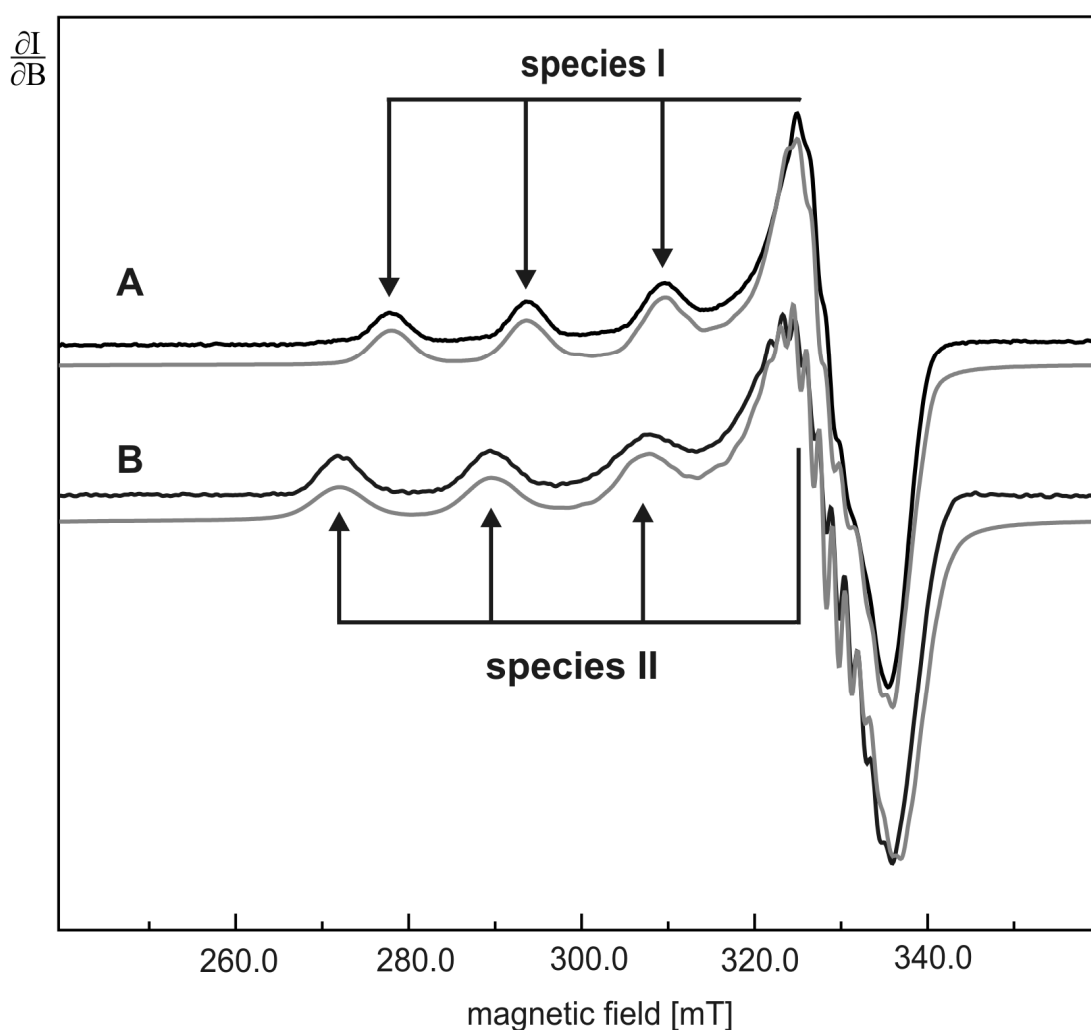
Figure 5.1: Black lines: X-band EPR spectra of the octapeptide–Cu^{2+} in NEM at pH 7.2 (A) and the tetraoctapeptide-Cu^{2+} in ammonium acetate buffer containing DPC at pH 7.5 (B). Grey lines: simulated spectra of these samples. The corresponding simulation EPR parameters are given in Table 5.1.

In Cu^{2+} complexes, nitrogen ligands can interact with the unpaired electron of the Cu^{2+} and give rise to further splitting of the hyperfine pattern, referred to as superhyperfine pattern. The multiplicity of these lines accounts for the number of nitrogen ligands. Indeed, in Figure 5.2, the existence of two well distinguishable species can be seen in the high-field region of the EPR spectra shown in Figure 5.1. Planar coordinations with three and four nitrogens for the octapeptide–Cu^{2+} (A) and the tetraoctapeptide-Cu^{2+} (B) respectively, give theoretical simulated spectra in best agreement with the experimental spectra.
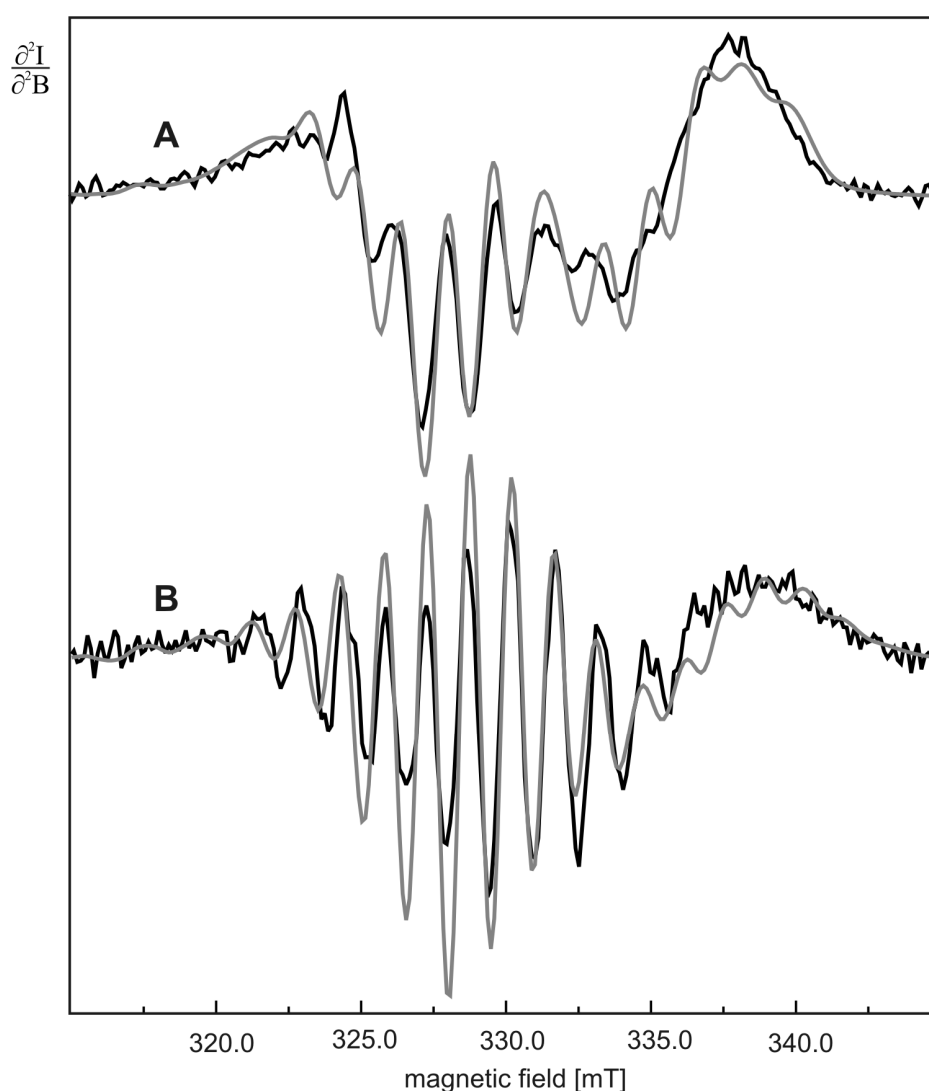
Figure 5.2: Black lines: high field region in second-derivative display of the EPR spectra of the octapeptide–Cu^{2+} in NEM at pH 7.2 (A) and the tetraoctapeptide-Cu^{2+} in ammonium acetate buffer containing DPC at pH 7.5 (B). Grey lines: simulated spectra of planar coordinations with three and four nitrogens for the octapeptide–Cu^{2+} (A) and the tetraoctapeptide-Cu^{2+} (B) respectively. The corresponding simulation EPR parameters are given in Table 5.1.

In the following, the EPR spectra of the samples studied in this work will be presented in groups attending to their sequence context.

Pentapeptide PrP(61-65) and Octapeptide PrP(60-67): Figure 5.3 depicts the EPR spectra of the pentapeptide and octapeptide, with one Cu^{2+} equivalent, at pH values around neutrality. The EPR spectra reveal two distinct species which show the typical features of square-planar type 2 Cu^{2+}–complexes. The pentapeptide– and octapeptide–Cu^{2+} complexes at pH values 7.5 and 7.2 respectively, show the same hyperfine pattern that we attribute to species I (C and E in Figure 5.3). Since the simulated spectra are in best agreement with the experimental spectra, it can be concluded that these samples contain only species I and therefore, both share one common peptide–Cu^{2+} configuration.

The EPR spectra of the pentapeptide– and octapeptide–Cu^{2+} complexes at pH value 6.5 exhibit an additional EPR species, referred to as species I-*LpH* in Figure 5.3 (spectra A and D) where the suffix *LpH* stands for low pH value. At pH 7.0 the EPR spectrum of the pentapeptide-Cu^{2+} shows mainly species I, although species I-*LpH* is also present as a residual species (B in Figure 5.3).

Figure 5.3 manifests that at pH values above 7.0, the EPR spectra of the pentapeptide- and octapeptide-Cu^{2+} complexes are attributable to species I without further contribution of species I-*LpH*.
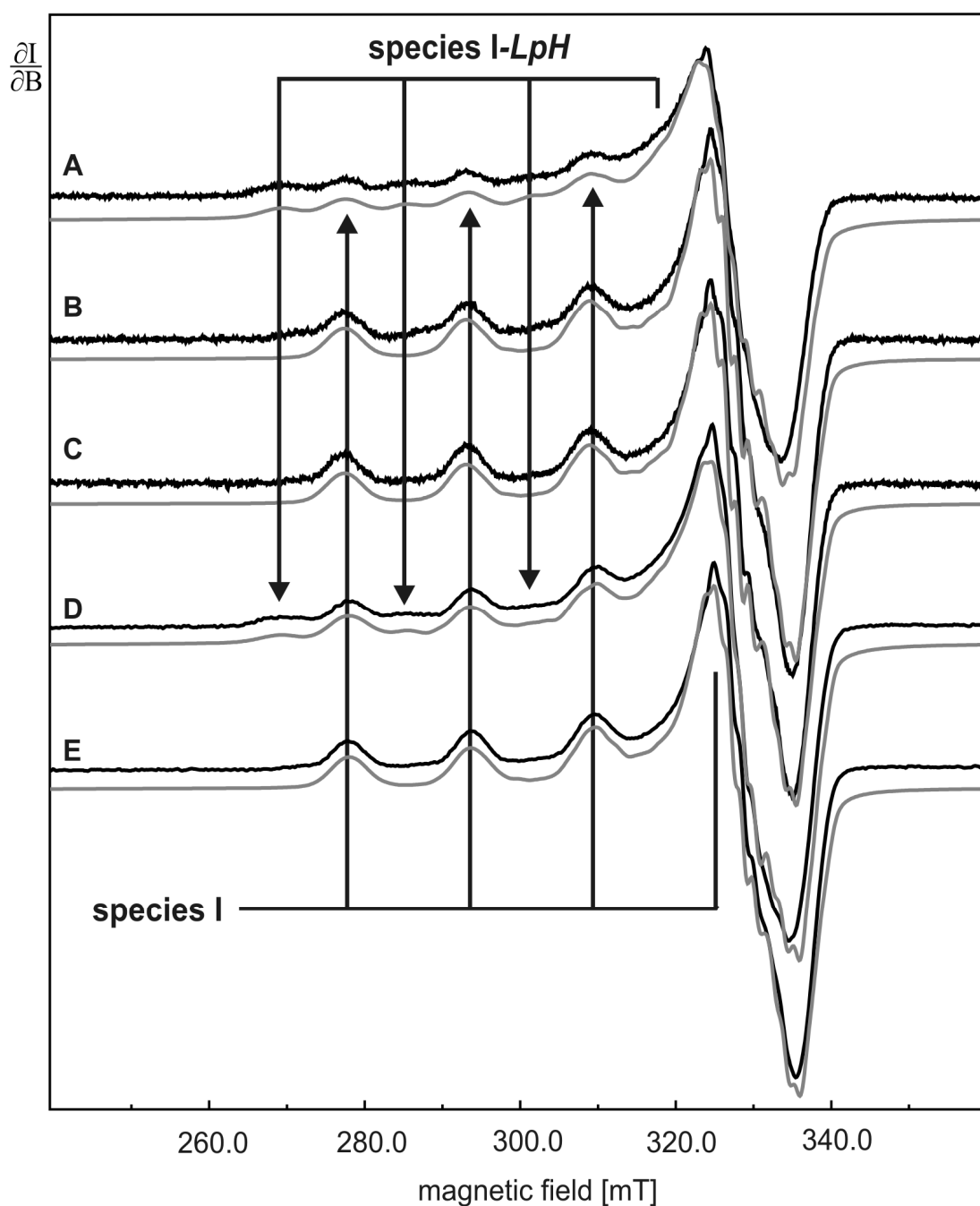
Figure 5.3: Black lines: X-band spectra of the pentapeptide PrP(61-65) at pH 6.5 (A), pH 7.0 (B), and pH 7.5 (C), and the octapeptide PrP(61-67) at pH 6.5 (D), and pH 7.2 (E), each with one Cu^{2+} equivalent. Grey lines: simulated spectra of these samples. The corresponding simulation parameters are given in Table 5.1.

Figure 5.4 depicts the second derivative of the high field region of the EPR spectra shown in Figure 5.3. All the spectra show basically the same superhyperfine pattern due to the contribution of species I. In contrast, species I-*LpH* does not contribute to the respective overall spectrum significantly. This can be explained due to the fact

that the contribution of species I-*LpH* to the superhyperfine structure is small compared to the contribution of species I.

$$\frac{\partial^2 I}{\partial^2 B}$$
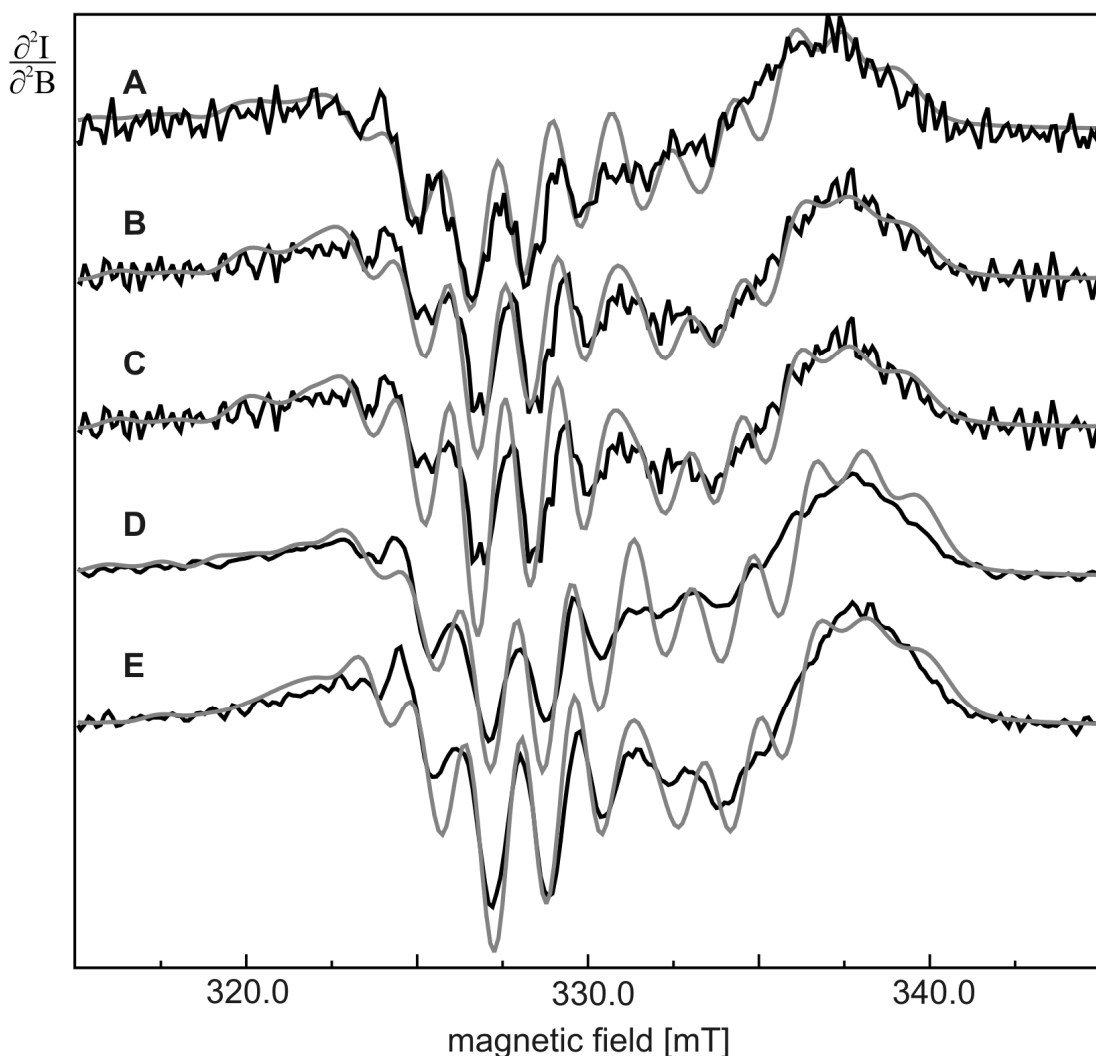
Figure 5.4: Black line: high field region in second-derivative display of the EPR spectra of the pentapeptide PrP(61-65) at pH 6.5 (A), pH 7.0 (B), and pH 7.5 (C), and the octapeptide PrP(61-67) at pH 6.5 (D), and pH 7.2 (E), each with one Cu^{2+} equivalent. Grey line: simulated spectra of planar coordinations with three nitrogens for these samples. The corresponding simulation parameters are given in Table 5.1.

Tetraoctapeptide PrP(60-91): Figure 5.5 displays the EPR spectra of the tetraoctapeptide with one through four Cu^{2+} equivalents at pH 7.5, in different buffers: NEM (A), MOPS (B), ammonium acetate containing DPC micelles (C), and phosphate containing DPC micelles (D). Here, in addition to the species I previously described, a new species referred to as species II can be identified. The appearance of

species in the EPR spectra depends on the tetraoctapeptide/Cu^{2+} ratio and the environment. All tetraoctapeptide samples with one stoichometric Cu^{2+} resemble a hyperfine pattern which we call species II. However, species I arises at greater Cu^{2+} load depending on the preparation environment. Note that in the case of phosphate buffer containing DPC micelles (D), all spectra show exclusively species II.
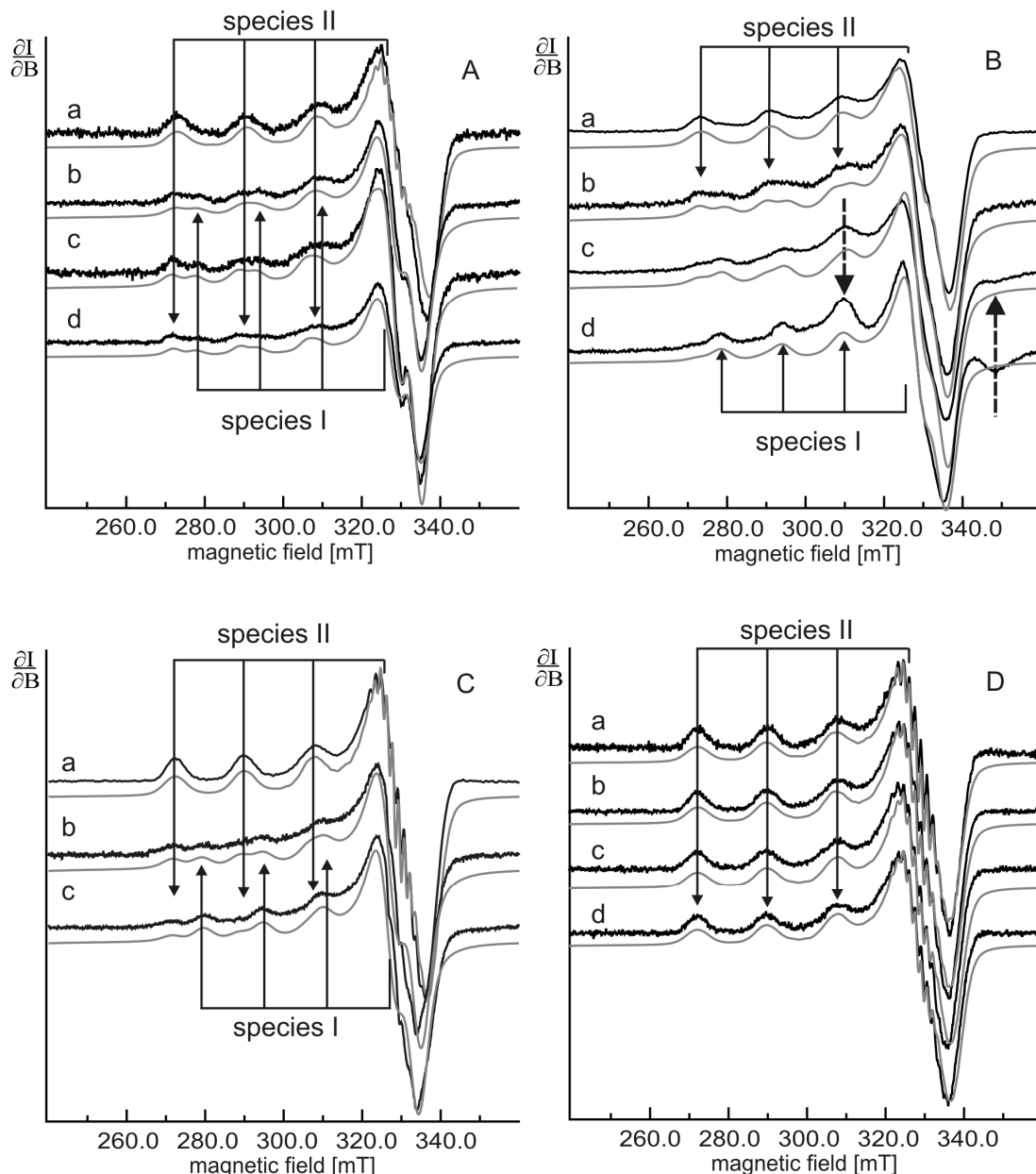
Figure 5.5: Black lines: EPR spectra of the tetraoctapeptide in different buffer systems and Cu^{2+} equivalents. Group A: NEM buffer; group B: MOPS buffer; group C: sodium phosphate containing DPC; group D: ammonium acetate buffer containing DPC. Within the groups, letters a, b, c and d stand for 1, 2, 3 and 4 Cu^{2+} equivalents respectively. Grey lines: simulated spectra of these samples. The corresponding simulation parameters are given in Table 5.1.

The EPR spectra of the tetraoctapeptide with three (c) and four (d) Cu^{2+} equivalents in MOPS buffer (Group B in Figure 5.5) are dominated by species I. However, these spectra exhibit additional features compared to the other preparations. In Figure 5.5, the features marked by large broken arrows point to approximately 310.0 and 347.0 mT, and suggest a strongly coupled dipolar spectrum superimposed on the uncoupled species I spectrum. These features are caused by copper contacts.

Strong dipolar coupling should be accompanied by a half field signal arising from a $\Delta m_S = 2$ transition. Indeed, the EPR spectrum of the tetraoctapeptide with three and four Cu^{2+} in MOPS reveals a half field signal centered at 160.0 mT as shown in Figure 5.6.
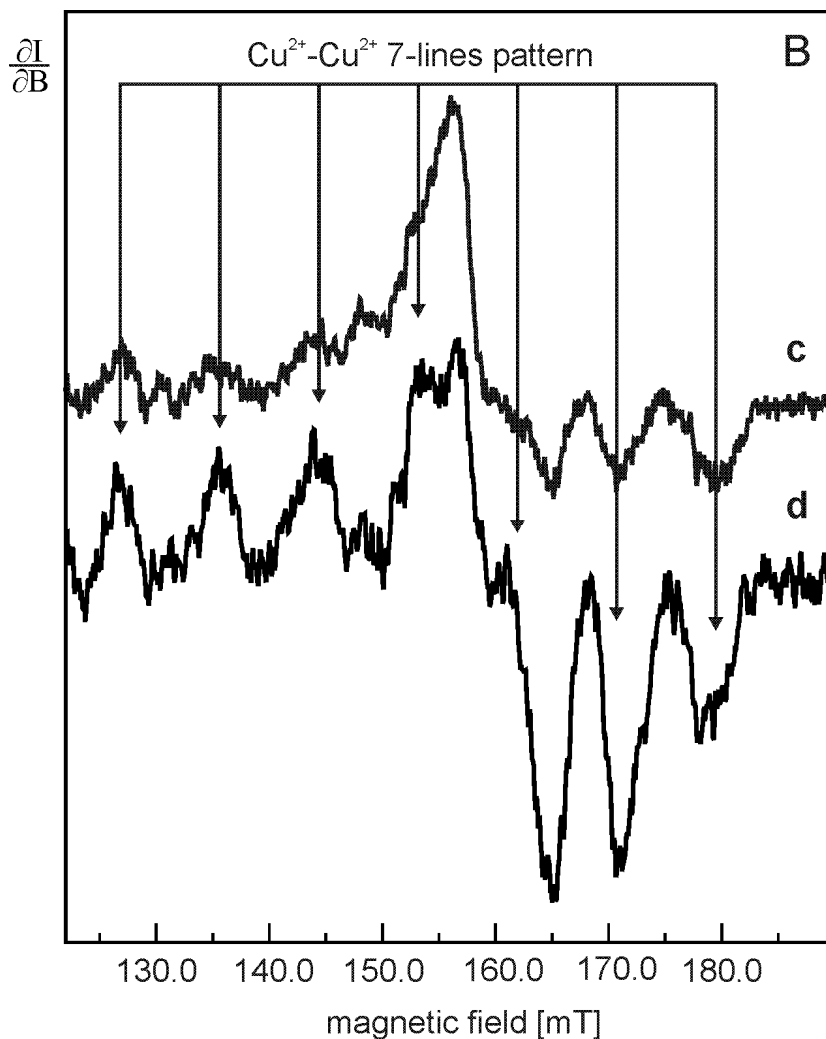
Figure 5.6: Half field signal of PrP(60–91) with 3 (c) and 4 Cu^{2+} (d) equivalents in MOPS buffer (B). The seven-line pattern is marked by arrows.

The tetraoctapeptide-3Cu^{3+} complex (c) showed a very weak half signal and presented a challenge while extracting the spectrum from the baseline. However, the main features of the dipolar pattern can still be observed. The hyperfine pattern shown in Figure 5.6 is caused by dipolar interaction of two identical Cu^{2+} ions ($I = 3/2$). A seven-line pattern with intensity in the ratio 1:2:3:4:3:2:1 is expected for such a complex.

The spectra shown in Figure 5.6 were collected at 35 K, within a sweep width of 1000 G, modulation amplitude of 15 G and microwave power of 5.029 mW. These conditions of data acquisition give the best signal-to-noise ratio.

Figure 5.7 depicts the high-field region of the EPR spectra shown in Figure 5.5. Like the spectra shown in Figure 5.5, the high-field region reveals a species distribution that varies upon the tetraoctapeptide/Cu^{2+} ratio and the environment. All tetraoctapeptides with one Cu^{2+} equivalent exhibit the same characteristic superhyperfine pattern, independently of the buffer system (Figure 5.7, spectrum a in groups A, B, C, and D). These features are very well resolved in all samples with one Cu^{2+} load, although their intensities vary upon the corresponding buffer. Planar coordinations with four nitrogen ligands for the tetraoctapeptide–1Cu^{2+} complexes in all buffer systems (a in groups A, B, C and D) give theoretical simulated spectra in best agreement with the experimental spectra. Note that all spectra in phosphate buffer exhibit precisely the same superhyperfine structure independently of the Cu^{2+} load (group D). However, in the other three buffer systems with more than one Cu^{2+} equivalent, the superhyperfine structure is not resolved due to overlapping of species I and II.
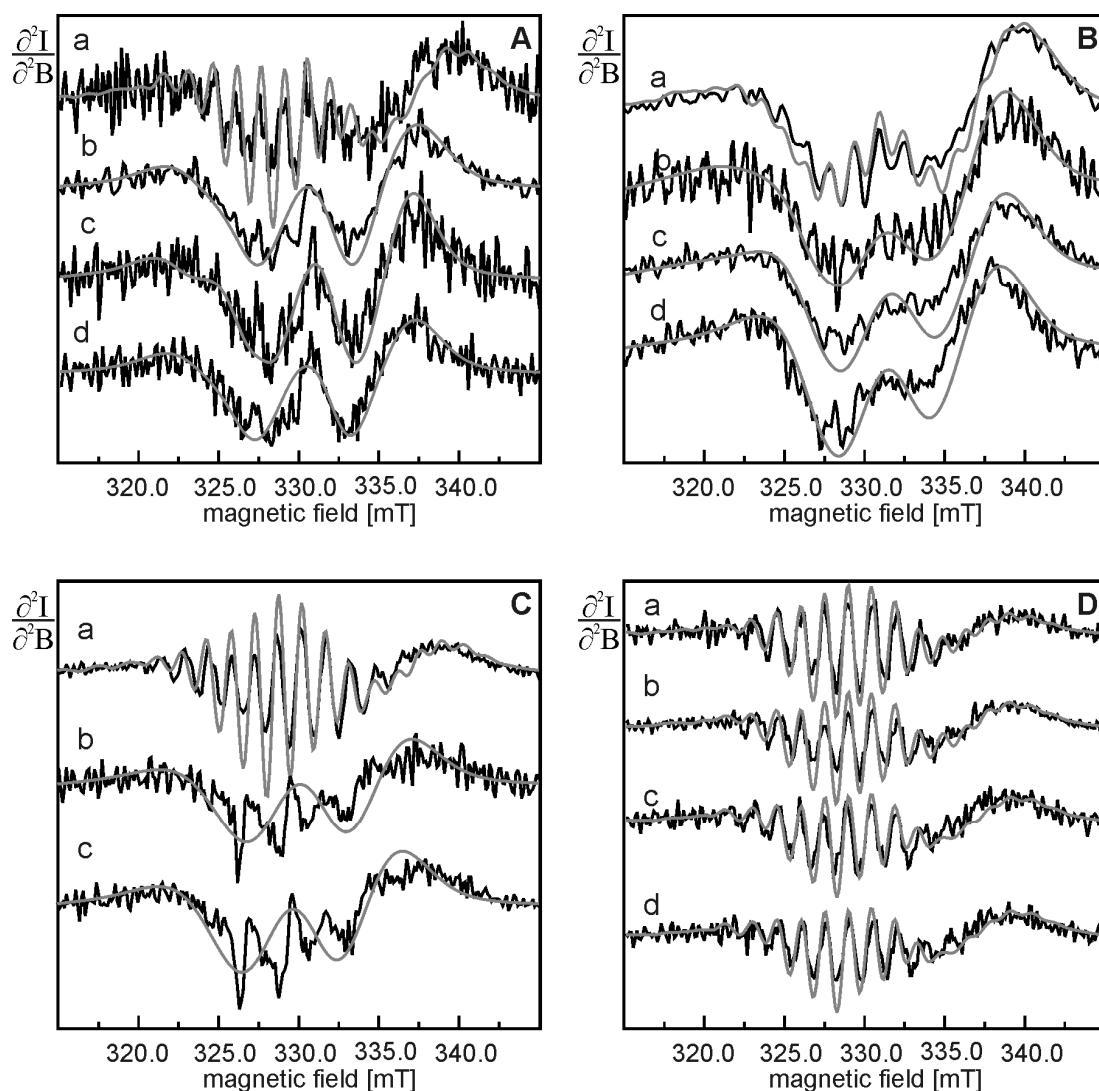
Figure 5.7: Black line: EPR in second derivative display of the high field region of the tetraoctarepeat peptide in different buffer systems and Cu^{2+} equivalents. Group A: NEM buffer; group B: MOPS buffer; group C: sodium phosphate containing DPC; group D: ammonium acetate buffer containing DPC. Within the groups, letters a, b, c and d stand for 1, 2, 3 and 4 Cu^{2+} equivalents respectively. Grey lines: simulated spectra of these samples. The corresponding simulation parameters are given in Table 5.1.

Recombinant human and mutant HG of the murine PrP(23–231): Figure 5.8 shows the EPR spectra of hPrP(23–231) with different Cu^{2+} contents (A and B) and the mutant HG of MmPrP(23–231) with one Cu^{2+} equivalent (C). For comparison, the EPR spectrum of the octapeptide–Cu^{2+} complex at pH 7.2 is also given as a species I type sample (spectrum D).
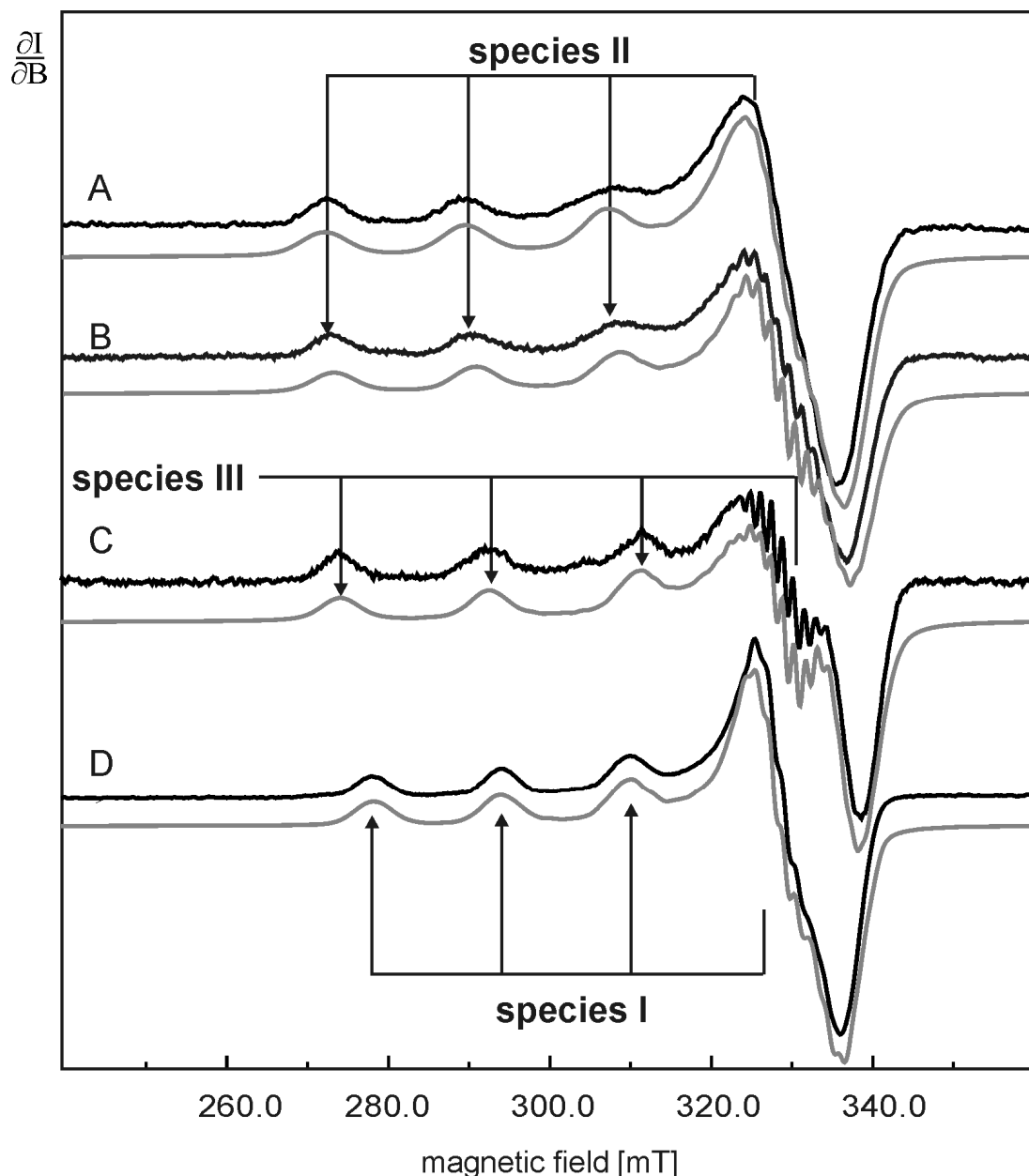
Figure 5.8: Black line: EPR spectra of the precipitated forms of recombinant hPrP(23–231) with 1.7 Cu^{2+} at pH 6.0 (A) and 2.7Cu^{2+} at pH 7.0 (B), the mutant HG of MmPrP(23–231) with 1 Cu^{2+} at pH 7.5 (C), and the octapeptide–Cu^{2+} complex at pH 7.2 in solution. Grey lines: simulated spectra of these samples. The corresponding simulation parameters are given in Table 5.1.

The EPR spectra of hPrP(23–231) exhibit apparently the characteristic features of species II independently of the Cu^{2+} load and pH value (spectra A and B in Figure 5.8). However, the mutant HG of MmPrP(23–231) shows a different hyperfine pattern referred to as species III in Figure 5.8 (C). Species III shows as well the typical features of square-planar type 2 Cu^{2+}–complexes and it is attributable to a new copper configuration that differs from either species I (D) or II (A and B).

Close inspection of the low-field region of the EPR spectra of the hPrP sample at pH 7.0 (B) reveals extra features which can be linked with an additional minor species, as shown in Figure 5.9. The contribution of this residual species is very small to the overall spectrum. Therefore, it is very challenging to connect this species to a unique set of hyperfine parameters. Nevertheless, the minor species is compatible with species I.
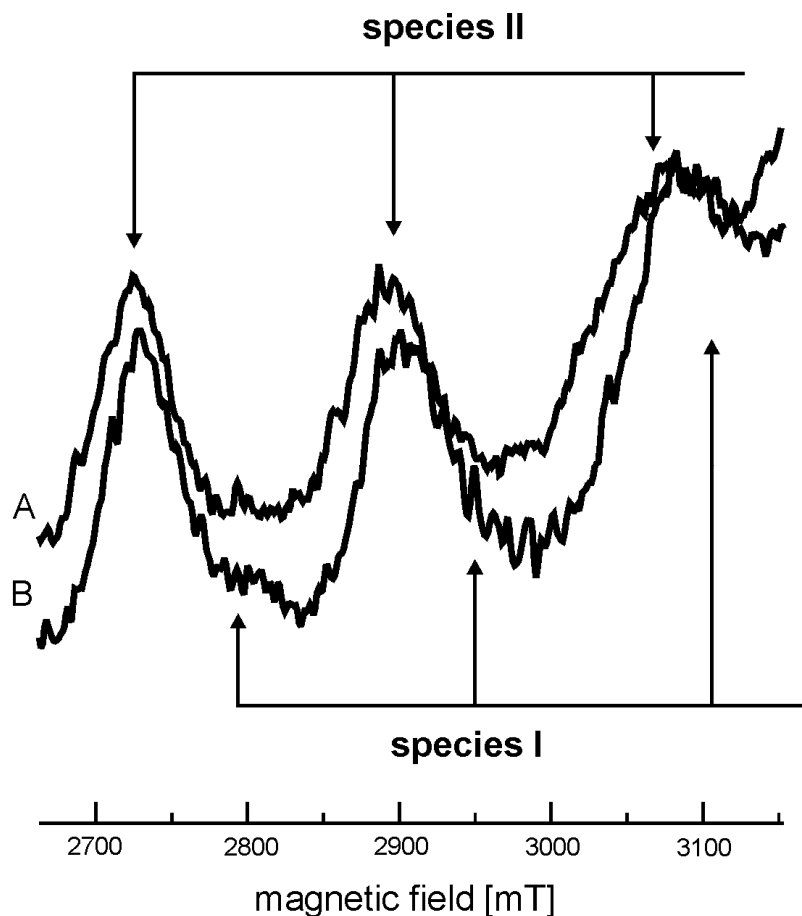
Figure 5.9: Low-field region of the EPR spectrum of hPrP(23–231) with 1.7 (A) and 2.7 Cu^{2+} (B) equivalents.

The EPR estimations shown in Figure 5.10 indicate that the signal of species I type complexes to the overall spectrum should be less than 20%.
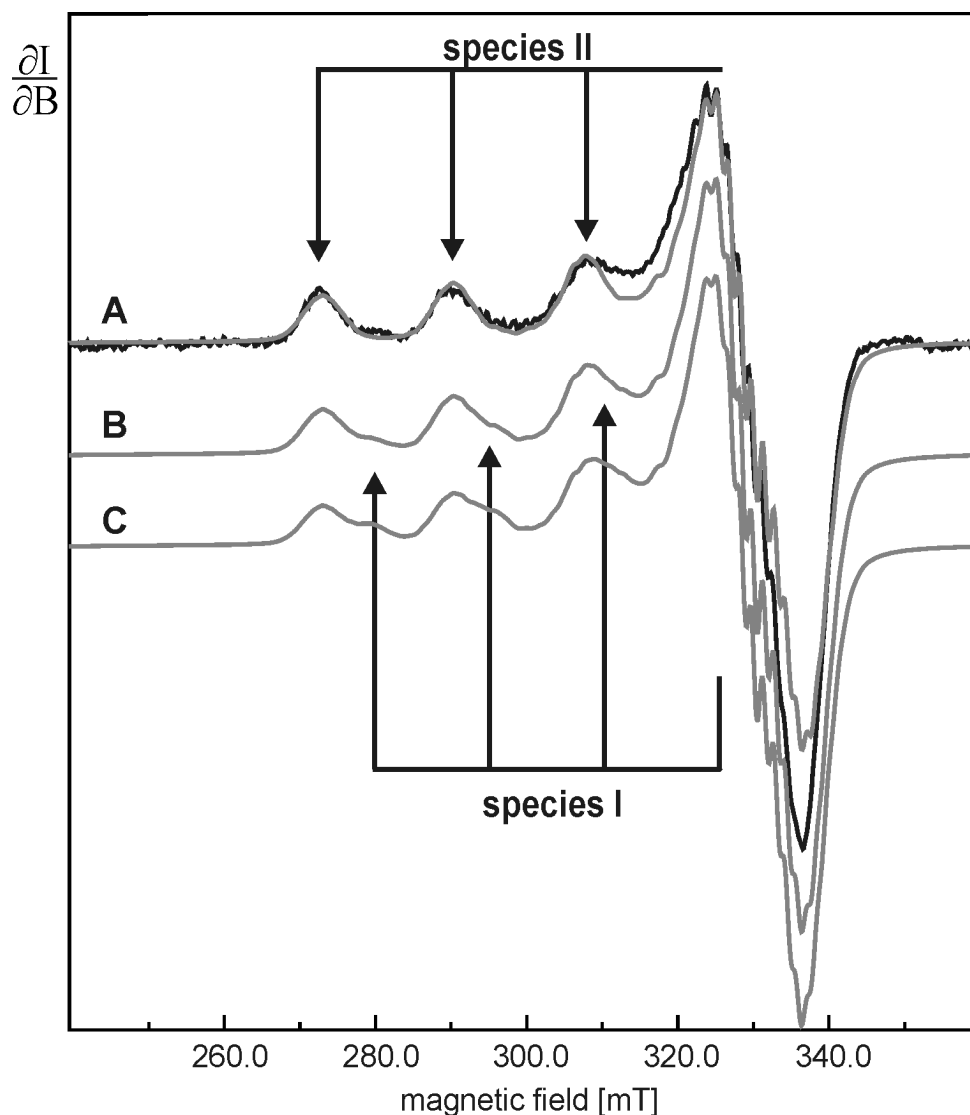
Figure 5.10: Black line: EPR spectrum of hPrP(23–231) with 2.7 Cu^{2+} equivalents at pH 7.0. Grey lines: simulations of 2.0 Cu^{2+} centers as species II and no additional Cu^{2+} as species I (A), additional 0.4 Cu^{2+} as species I (B), and additional 0.7 Cu^{2+} as species I (C).

The high-field region of the EPR spectra shown in Figure 5.8 supports the existence of three species (Figure 5.11). Both spectra of the hPrP(23–231) samples exhibit the same superhyperfine pattern with a line splitting of approximately 1.45 mT. Note that the intensity of the superhyperfine lines is larger at pH 7.0 than at pH 6.0 (compare spectra A and B in Figure 5.11). The mutant HG displays the same number of superhyperfine lines as the recombinant hPrP samples but with a slightly lower

line splitting of about 1.35 mT. One can then conclude that the Cu^{2+} configurations corresponding to species II and III are different, although both species share the same number of nitrogen ligands. In contrast, although species I shows the same line splitting as species II (about 1.45 mT), the superhyperfine structure of species I shows less number of lines than species II or III. The increase of superhyperfine lines from species I to species II or III indicates an increment of the nitrogen atoms that participate in the Cu^{2+} coordination.
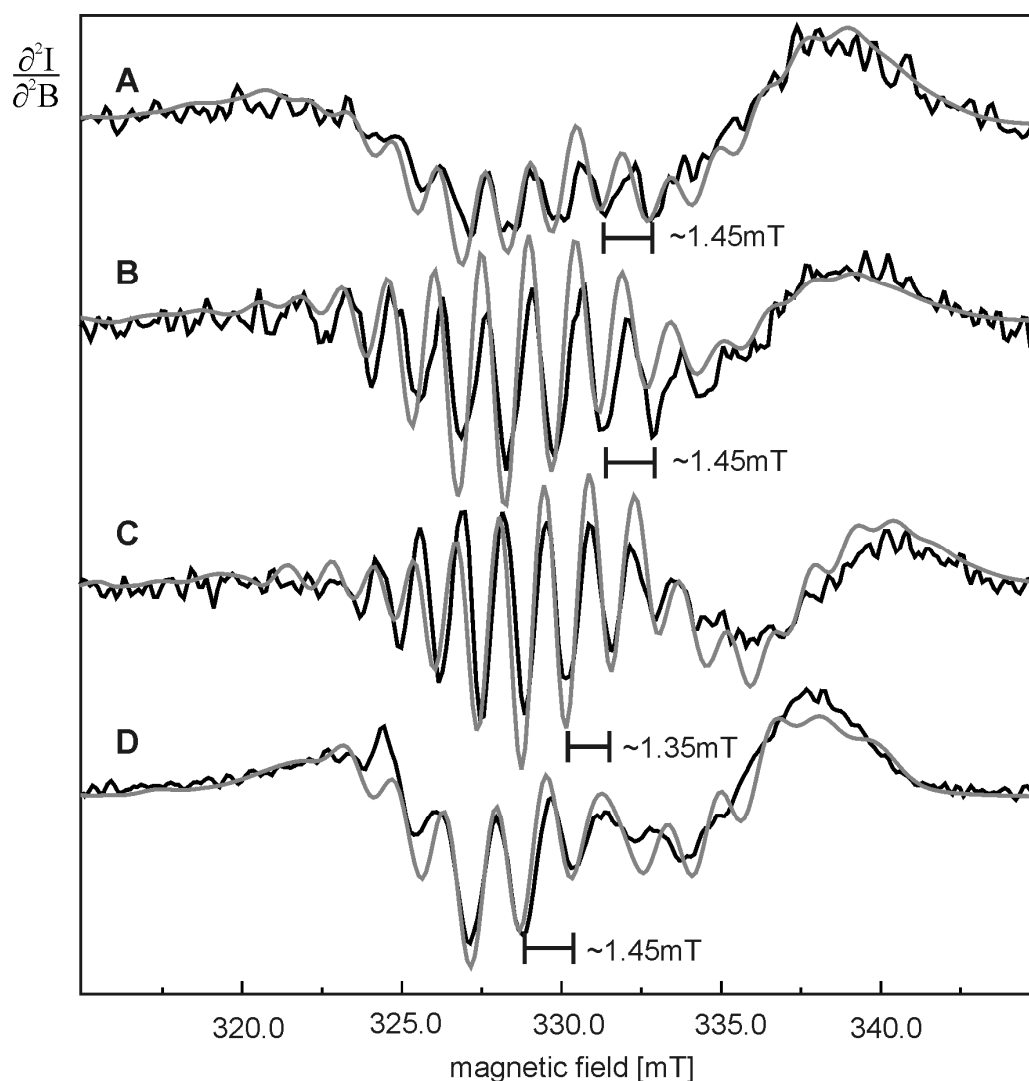
Figure 5.11: Second-derivative display of the high-field region of the precipitated forms of recombinant hPrP(23–231) with 1.7 Cu^{2+} at pH 6.0 (A), 2.7Cu^{2+} at pH 7.0 (B), the mutant HG of MmPrP(23–231) with 1 Cu^{2+} at pH 7.5 (C), and the octapeptide–Cu^{2+} complex at pH 7.2 in solution (D). Grey lines: simulated spectra of planar coordinations with three and four nitrogens for the octapeptide–Cu^{2+} (D) and the precipitated samples (A, B and C) respectively. The corresponding simulation EPR parameters are given in Table 5.1.

The program package Xemr was used to simulate EPR spectra (visit http://www.epr.chem.jyu.fi/xemr/ for more information). In the following, Table 5.1 summarizes the parameters used for simulation of the EPR spectra presented in this work.

Table 5.1

sample	pH	buffer	g_{xx}	g_{yy}	g_{zz}	A_{xx}^{Cu}	A_{yy}^{Cu}	A_{zz}^{Cu}	A_{xx}^{N}	A_{yy}^{N}	A_{xx}^{N}	Species	Nitrogen ligands
penta[5]+1Cu2+	6.5	*a*	2.08	2.08	2.30	7	7	179	unresolved			I-*LpH*	unresolved
			2.06	2.07	2.25	8	9	170	15.4	15.4	12.6	I	3
penta+1Cu2+	7.0	*a*	2.06	2.07	2.25	8	9	170	15.4	15.4	12.6	I	3
penta+1Cu2+	7.5	*a*	2.06	2.07	2.25	8	9	170	15.4	15.4	12.6	I	3
octa[6]+1Cu2+	6.5	*a*	2.08	2.08	2.30	11	11	180	unresolved			I-*LpH*	unresolved
			2.06	2.07	2.25	8	9	170	15.4	15.4	12.6	I	3
octa+1Cu2+	7.2	*a*	2.06	2.07	2.25	8	9	170	15.4	15.4	12.6	I	3
tetra[7]+1Cu2+	7.5	*a*	2.05	2.07	2.26	6	16	194	14.0	14.5	14.5	II	4
tetra+2Cu2+	7.5	*a*	2.05	2.08	2.27	5	15	188	unresolved			II	unresolved
			2.06	2.07	2.25	5	12	170				I	unresolved
tetra+3Cu2+	7.5	*a*	2.05	2.08	2.28	5	16	188	unresolved			II	unresolved
			2.05	2.07	2.25	5	5	170				I	unresolved
tetra+4Cu2+	7.5	*a*	2.05	2.08	2.27	5	13	187	unresolved			II	unresolved
			2.05	2.07	2.25	5	6	170				I	unresolved
tetra+1Cu2+	7.5	*b*	2.05	2.07	2.27	6	16	194	14.0	14.5	14.5	II	4
tetra+2Cu2+	7.5	*b*	2.06	2.08	2.28	5	7	190	unresolved			II	unresolved
			2.07	2.08	2.24	5	14	170				I	unresolved

[5] penta stands for the pentapeptide, hPrP(61-65).
[6] octa stands for the octapeptide, hPrP(60-67).
[7] tetra stands for the tetraoctapeptide, hPrP(60-91).

Table 5.1   69

	pH		g_{xx}	g_{yy}	g_{zz}	A_{xx}^{Cu}	A_{yy}^{Cu}	A_{zz}^{Cu}	A_{xx}^{N}	A_{yy}^{N}	A_{zz}^{N}		
tetra+3Cu2+	7.5	*b*	2.06	2.08	2.28	5	7	190		unresolved		II	unresolved
			2.07	2.08	2.24	5	14	170				I	unresolved
tetra+1Cu2+	7.5	*c*	2.05	2.07	2.27	6	16	192	14.0	14.5	14.5	II	4
tetra+2Cu2+	7.5	*c*	2.05	2.07	2.27	6	16	192	14.0	14.5	14.5	II	4
tetra+3Cu2+	7.5	*c*	2.05	2.07	2.27	6	16	192	14.0	14.5	14.5	II	4
tetra+4Cu2+	7.5	*c*	2.05	2.07	2.27	6	16	192	14.0	14.5	14.5	II	4
tetra+1Cu2+	7.5	*d*	2.05	2.07	2.26	5	19	193	14.0	14.5	14.5	II	4
tetra+2Cu2+	7.5	*d*	2.05	2.08	2.27	5	17	188		unresolved		II	unresolved
			2.04	2.06	2.23	5	5	174				I	unresolved
tetra+3Cu2+	7.5	*d*	2.05	2.08	2.27	5	17	188		unresolved		II	unresolved
			2.04	2.06	2.23	5	5	170				I	unresolved
tetra+4Cu2+	7.5	*d*	2.05	2.08	2.27	5	17	188		unresolved		II	unresolved
			2.04	2.06	2.23	5	5	170				I	unresolved
hPrP[8]+1.7Cu2+	6.0	*e*	2.05	2.08	2.27	14	19	188	12.3	13.4	13.5	II	4
hPrP+2.7Cu2+	7.0	*f*	2.07	2.05	2.26	10	14	189	14.5	14.5	14.0	II	4
m-PrP[9]+1Cu2+	7.5	*d*	2.05	2.06	2.24	10	17	200	10.7	13.6	13.8	III	4

Table 5.1: Parameters of the simulated EPR spectra, where g_{xx}, g_{yy}, g_{zz} are the principal values of the g tensor, $A_{xx}^{Cu}, A_{yy}^{Cu}, A_{zz}^{Cu}$ are the principal values of the magnetic hyperfine A^{Cu} tensor, and $A_{xx}^{N}, A_{yy}^{N}, A_{zz}^{N}$ are the principal values of the magnetic superhyperfine A^{14N} tensor. The g, A^{Cu} and A^{14N} tensors are defined as usual.

---

[8] hPrP stands for recombinant human PrP(23-231).
[9] m-PrP stands for mutant HG of the recombinant murine PrP(23-231).

5.2 ENDOR results

In Cu^{2+} paramagnetic complexes, the unpaired electron of the Cu^{2+} ion interacts with nuclear spin of protons via dipolar and Fermi contact interactions, giving rise to an energy shift of the ^{1}H nuclear magnetic resonant (NMR) lines. The dipolar interaction depends on the position of the ^{1}H with respect to the metal ion. Therefore, ENDOR spectra taken at molecular orientations selected by EPR can then be used to determine ^{1}H positions (Hurst et al., 1985). ENDOR spectra of selected samples were recorded at nine different magnetic fields, also referred as EPR working points. Each of these working points selects orientations θ of the corresponding copper complexes, where the angle θ defines the orientation of the symmetry axis of the copper complex with respect to the magnetic field (see Figure 5.12). Table 5.2 shows the orientations of the selected molecules for the studied samples.
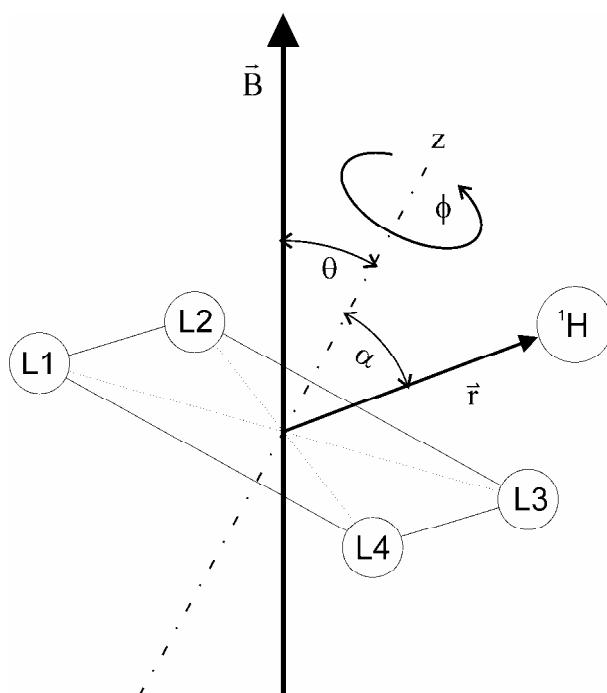
Figure 5.12: The four ligands of the Cu^{2+} center define a plane. The normal of this plane is called z, and rotations around this axis are described by the angle ϕ. The proton ^{1}H at the position $\vec{r}$ forms an angle α with respect to z. The magnetic field $\vec{B}$ is turned an angle θ with respect to z. L1, L2, L3 and L4 represent the first ligands of the Cu^{2+} center.

working point	magnetic field (mT)	θ for species I	θ for species II	θ for species III
1	279.0	0°	25°	20°
2	286.4	27°	32°	34°
3	293.8	0°, 40°	21°, 48°	10°, 44°
4	301.0	31°, 50°	38°, 57°	32°, 53°
5	308.2	0°, 45°, 59°	10°, 51°, 65°	45°, 62°
6	315.6	35°, 58°, 69°	38°, 63°, 74°	28°, 58°, 62°
7	323.0	0°, 54°, 72°, 80°	58°, 79°, 85°	47°, 70°, 79°
8	328.3	34°, 70°, 90°	29°, 87°	62°, 83°, 89°
9	334.0	66°	63°	33°, 83°

Table 5.2: Correlation of the working points with the magnetic fields of the EPR spectrometer. For each working point only molecules which have a certain orientation θ to the magnetic field contribute, where θ defines the angle formed between the applied magnetic field and the z-axis of the molecular coordinate system (see Figure 5.12).

In order to study the ^{1}H environment of the species observed in the previously reported EPR experiments, ENDOR spectra were taken at representative samples of EPR–detected species. Figure 5.13 shows the ENDOR spectra of the pentapeptide–(A), octapeptide–Cu^{2+}(B), and tetraoctapeptide–$4Cu^{2+}$ (C) complexes which can be described by species I. Figure 5.14 displays the tetraoctapeptide-Cu^{2+} (A) and hPrP(23–231)–$2.7Cu^{2+}$ (B) complexes, both ascribable to species II samples. In addition, Figure 5.14 also displays the ENDOR spectra of the mutant HG of the MmPrP (C) which previously was linked to species III.

For all samples studied in this work, ENDOR spectra show a common intense signal centered on the proton nuclear Zeeman frequency (see υ_L in Figure 5.13 and 5.14). These broad lines are the consequence of the contribution of weakly coupled protons ($|\vec{r}| > 3.7\text{Å}$) to the spectra and dominate the spectra in the region of 10-15 MHz depending upon the selected working point (see e.g., grey area in Figure 5.13 at the wp9). As one selects higher magnetic fields (rising the working point), these broad resonances appear at higher frequencies. In addition, on each side of the weakly-coupled ^{1}H resonances, broad and relatively weak lines are discernible (see coupled resonances $\upsilon_{1+} - \upsilon_{1-}$ and $\upsilon_{2+} - \upsilon_{2-}$ in Figure 5.13 at the wp9). These resonances can be described by protons sited at distances less than 3.7Å with respect to the respective

copper center. Their patterns are approximately shifted in parallel to the proton nuclear Zeeman frequency depending on the magnetic field.

The three samples represented in Figure 5.13 display very similar ^{1}H–ENDOR spectra and most likely, they have the same proton environment around their respective Cu^{2+} centers. However, the ENDOR spectra of the pentapeptide– (A) and the octapeptide–Cu^{2+} complex (B) display precisely the same pattern of intensities whereas in the tetraoctapeptide–$4Cu^{2+}$ complex (C), the ratio between the line resulting from weakly coupled protons (e.g., the grey area at the wp9) and the side resonances (solid arrows at wp9) is larger than for the other two samples (A and B). In the tetraoctapeptide–$4Cu^{2+}$ sample (C), there are more ^{1}H available at distances $|\vec{r}| > 3.7 \text{Å}$ than in the pentapeptide– (A) and the octapeptide–Cu^{2+} complex (B) and therefore, the central line must be more intense.

On the other hand, the ^{1}H–ENDOR spectra of the tetraoctapeptide–$1Cu^{2+}$ and the recombinant hPrP (Figure 5.14, A and B respectively) exhibit the same resonance lines and intensity pattern through all the working points. Therefore, we can conclude that the Cu^{2+} centers of the hPrP sample share the same ^{1}H environment as the tetraoctapeptide–$1Cu^{2+}$ complex. However, the mutant HG of MmPrP (C) displays a different ^{1}H-ENDOR pattern to the one attributable to species II (A and B in Figure 5.14). Nevertheless, it is quite similar to the ^{1}H-ENDOR pattern resulting from species I type samples (Figure 5.13).

The ^{1}H-ENDOR analysis of selected samples clearly supports our interpretation of the EPR data. Our observations confirm that the EPR species I, II, and III, can be interpreted as different peptide–Cu^{2+} configurations. Moreover, we were able to map the ^{1}H environment of the corresponding species.
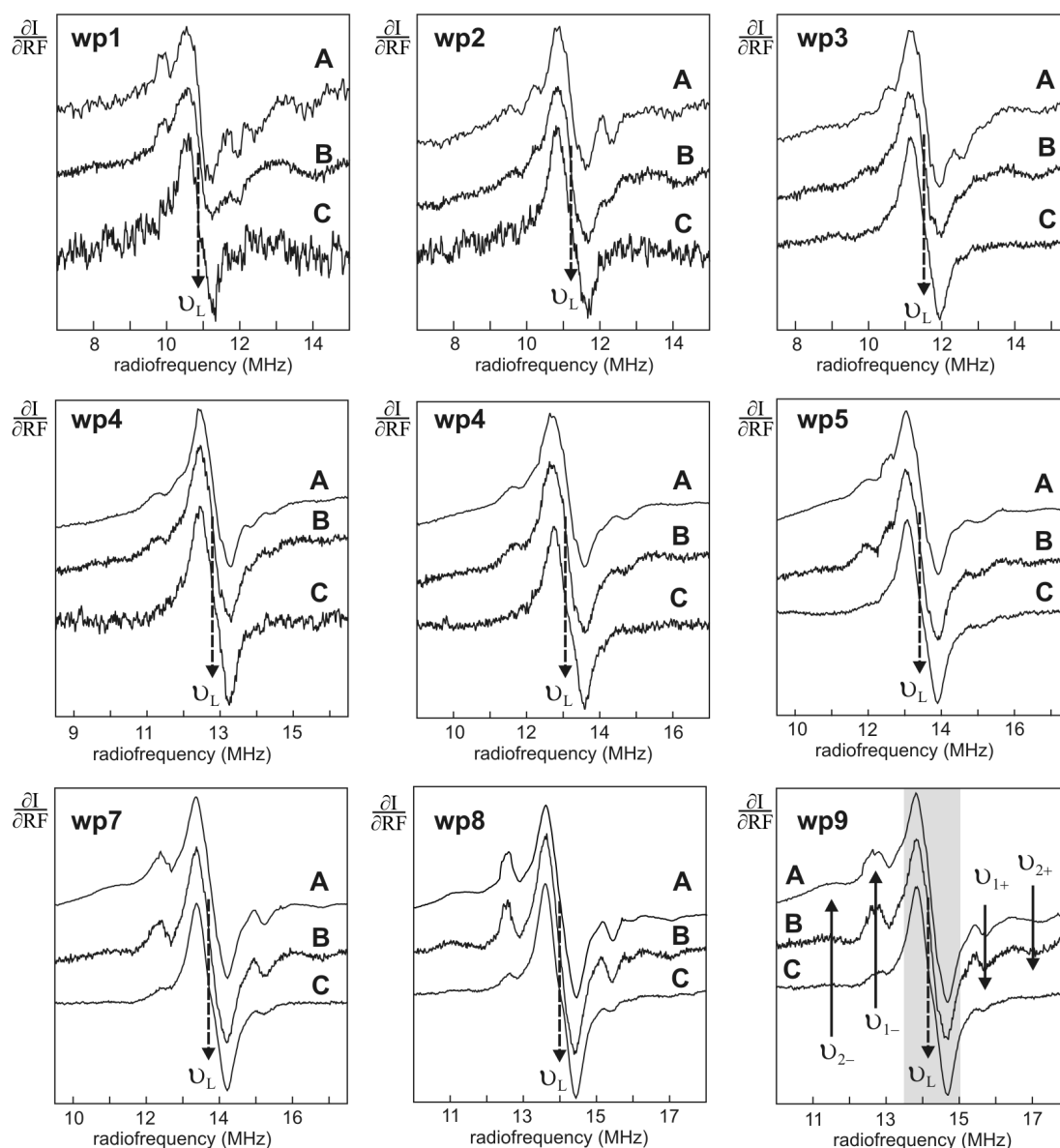
Figure 5.13: ENDOR spectra of the pentapeptide-Cu^{2+} at pH 7.5 (A), octapeptide-Cu^{2+} pH 7.2 (B) and tetraoctapeptide-$4Cu^{2+}$ in MOPS buffer at pH 7.5 (C). The spectra were taken at 9 different magnetic fields (wp1 to wp9). Broken arrows point to the ^{1}H nuclear Zeeman frequency (υ_L). At the wp9, the grey area marks the influence region of weakly coupled protons. Solid arrows point to resonances from ^{1}H sited at $|\vec{r}| < 3.7 \text{Å}$.
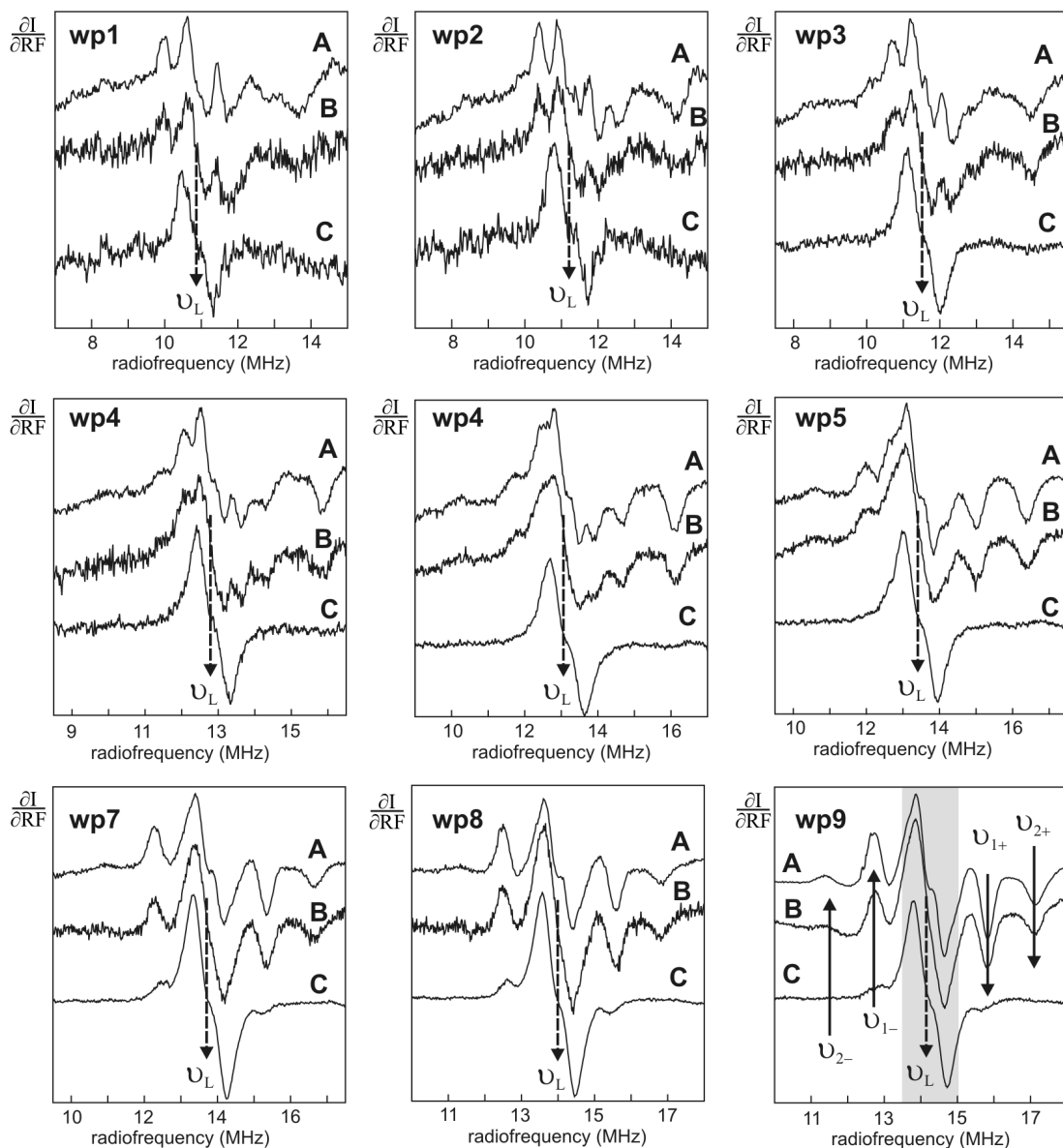
Figure 5.14: ENDOR spectra of the tetraoctapeptide–1Cu^{2+} in ammonium acetate buffer containing DPC (A), the recombinant hPrP(23–231) at pH 7.0 loaded with 2.7 Cu^{2+} equivalents (B), and the mutant HG of the MmPrP with 1 Cu^{2+} equivalent. The spectra were taken at 9 different magnetic fields (wp1 to wp9). Broken arrows point to the ^{1}H nuclear Zeeman frequency (υ_L). At the wp9, the grey area marks the influence region of weakly coupled protons. Solid arrows point to resonances from ^{1}H sited at $|\vec{r}| < 3.7\text{Å}$.

5.3 EXAFS results

The experimental k^3–weighted EXAFS spectra and their corresponding Fourier transforms (FT) of the octapeptide–Cu^{2+} at pH 7.2 (A), as well as the tetraoctapeptide–$4Cu^{2+}$ in MOPS buffer at pH 7.5 (B) are displayed in Figure 5.15a and 5.15b respectively. The FT of the spectra indicates the distance of scattering atoms to the absorbing centre as a radial distribution function. Inspection of the k^3–weighted EXAFS spectra and its FT essentially confirms one type of Cu^{2+}–complex as suggested by EPR and ENDOR data, species I. In these complexes, the EXAFS spectra are dominated by a main single signal. This oscillation is characterized by low frequency with maximums at approximately 4.7, 6.7, 8.7, and 10.7 $\AA^{-1}$ (broken arrows in Figure 5.15a). It is caused by the nearest neighbor coordination. In addition, the EXAFS signal exhibits weak high frequency oscillations which cause the features in the regions 4.5–5.0 $\AA^{-1}$ and 5.7–6.2 $\AA^{-1}$ (grey areas in Figure 5.15a). These features and the broad weak peaks at ~ 3 and 4 $\AA$ of the FT (solid arrows in Figure 5.15b) support the presence of a histidine residue in the Cu^{2+} binding site of these complexes.
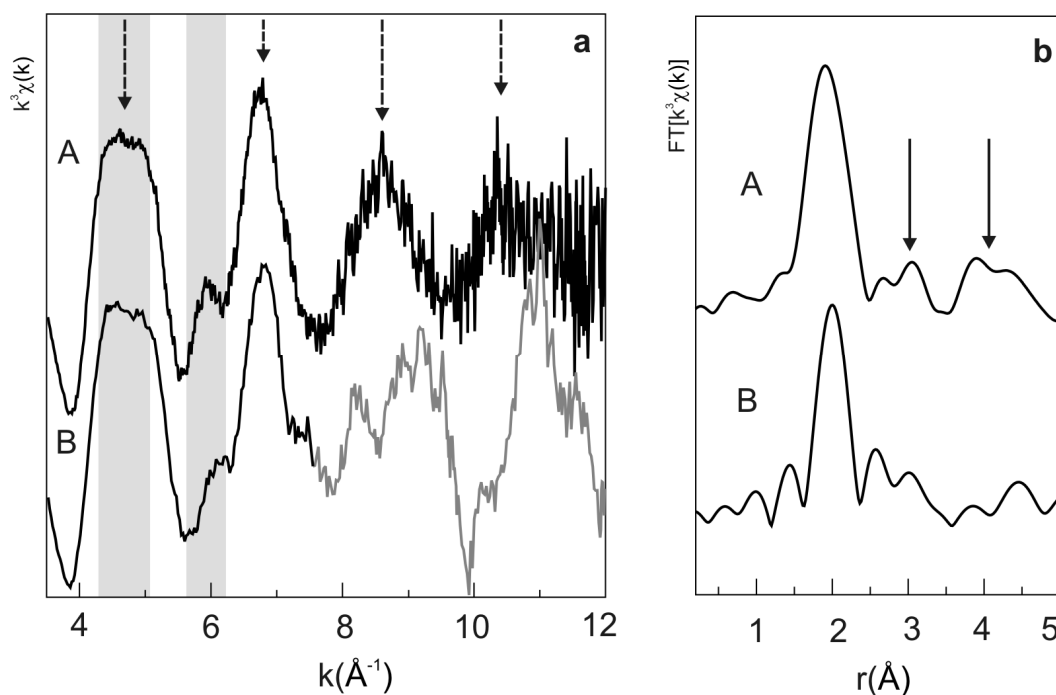
Figure 5.15: (a) k^3–weighted EXAFS spectra of the octapeptide–Cu^{2+} at pH 7.2 (A), tetraoctapeptide–$4Cu^{2+}$ at pH 7.5 (B); (b) Corresponding FT of the EXAFS spectra of A and B.

Note that beyond ~8 Å^{-1}, the tetraoctapeptide (grey part of the spectrum B in Figure 5.15a) displays a rather different EXAFS in comparison to the EXAFS signal of the octapeptide. This difference is caused by contamination from copper hydroxide precipitate. EXAFS requires very homogeneous samples because all the copper added to the samples influences the EXAFS signal, unlike EPR and ENDOR, where only paramagnetic copper contributes to the spectra. Therefore, one should not consider the region beyond ~8 Å^{-1} of the EXAFS of the tetraoctapeptide and subsequently, its influence in the corresponding FT of the spectrum.

Figure 5.16a and 5.16b depicts the k^3–weighted EXAFS spectra and their corresponding FT of the precipitated forms of hPrP(23–231) with 1.7 Cu^{2+} at pH 6.0 (A), 2.7 Cu^{2+} at pH 7.0 (B) and in solution, with 1.3 at pH 6.0 (C).
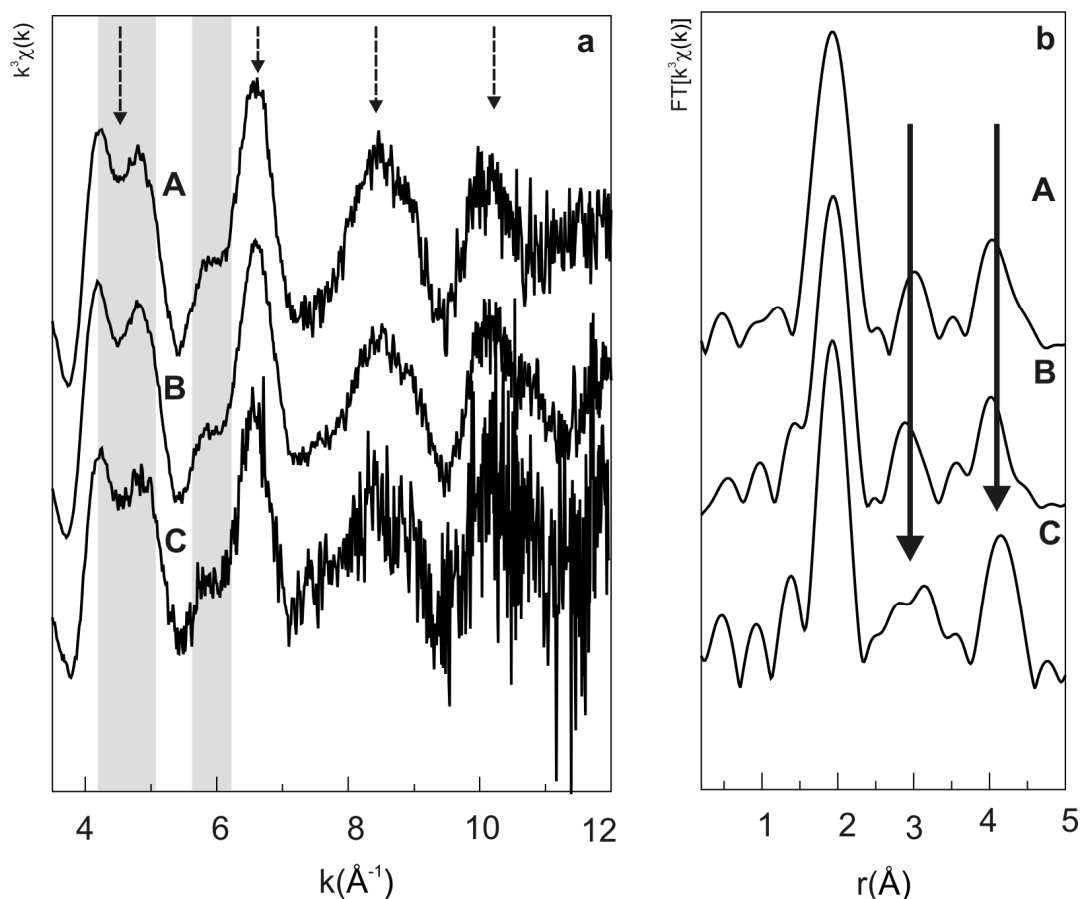
Figure 5.16: (a) k^3–weighted EXAFS spectra of the precipitated forms of hPrP(23–231) with 1.7 Cu^{2+} at pH 6.0 (A), 2.7 Cu^{2+} at pH 7.0 (B) and in solution, with 1.3 at pH 6.0 (C); (b) Corresponding FT of the EXAFS spectra of A, B, and C.

In Figure 5.16a, all spectra display the same qualitative features, independent of the pH variation and aggregation state. Note that the statistics for the spectrum of hPrP(23–231)/1.3 Cu^{2+} (C) are significantly worse compared to the other spectra, due to the lower concentration of copper existing in the sample. Consequently, samples with precipitated material were measured. The EXAFS spectra shown in Figure 5.16a exhibit a main oscillation which dominates the EXAFS signal with maximums at approximately 4.5, 6.7, 8.5, and 10.2 Å^{-1} (broken arrows in Figure 5.16a). As already discussed, this signal originates from the coordinating ligands. The additional features in the regions 4.5–5.0 Å^{-1} and 5.7–6.2 Å^{-1} (grey areas in Figure 5.16a), as well as the peaks at ~ 3 and 4 Å in Figure 5.16b can only be explained by multiple scattering processes. They are typical for multiple scattering by imidazole rings.

Model Building and Molecular Mechanics Simulations

6

In this chapter, the data resulting from EPR, ENDOR, and EXAFS measurements of the Cu^{2+} binding site of hPrP(23–231) are combined with molecular mechanics calculations and subsequently used by a simulated annealing protocol which enables us to obtain several models of the octarepeat domain of hPrP in complex with two Cu^{2+} ions. These models can be then simulated and compared with the original experimental data.

6.1. Model Building

Using that information collected by means of EPR, ENDOR and EXAFS, a model of the peptide–Cu^{2+} associated to species II can be proposed. In the context of the recombinant hPrP, a model of the octarepeat domain with two copper centers was built taking into account the following:

- According to EPR data, species I and II consist of a square planar 3N-1O and 4N configurations respectively. An axial weakly bound ligand is also possible.

- ENDOR spectra reveal that species I and II require complexes with quite similar proton surroundings including resonances associated to axial water. However, species II is likely to bind two hystidil imidazoles whereas species I binds one hystidil imidazole.

- EXAFS spectra of species I and II show a very similar main oscillation. The main differences are found in multiple-scattering features. EXAFS data supports the fact that species II is coordinated by two hystidil imidazoles.

Detailed justification of the information derived by means of EPR, ENDOR and EXAFS will be given in the discussion[10].

The following Cu^{2+} configuration fulfils the requirements previously introduced: The nitrogens of the deprotonated amides Gly70, Gly71 and the N_δ of the imidazole of His69 are ligands in species I as well as in species II. However, the oxygen of Gly71 in species I is replaced by the N_δ of His61. An axial water molecule completes the penta–coordination. The second Cu^{2+} ion is bound identically by the third and fourth histidine imidazoles and the corresponding glycines. In this context, one should remember that each histidine of the octarepeat domain is a possible Cu^{2+} binding site. Since in the model discussed here two histidines bind to each Cu^{2+} center, there remain only two Cu^{2+} sites. Both binding places are identical with respect to the first coordination shell. A simplified drawing of the proposed model is shown in Figure 6.1.
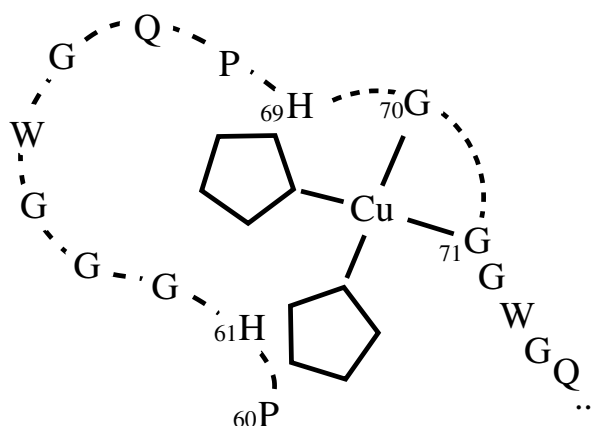
Figure 6.1: Sketch of the Cu^{2+} coordination in species II in the context of the recombinant hPrP(23–231) in presence of two copper centers.

6.2. Molecular Mechanics and Simulated Annealing

Taking into account the previously proposed Cu^{2+} configuration of species II, modeling computations allow us to generate structures with low energy and reliable covalent geometry. The classical molecular mechanics force field CHARMM22

---

[10] Chapter 7, section 7.1. Copper Configurations: Species I, II and III.

(MacKerell Jr. et al., 1998) in combination with additional molecular mechanics (MM) parameters (Weiss, in preparation) were used to build a basic copper configuration consistent with the model shown in Figure 6.1. Standard simulated annealing protocols within the MM-molecular dynamics (MD) program XPLOR (Brünger, 1992) were used to generate multiple structures by means of successive energy minimizations of a basic configuration previously generated.

Initially, an extended random coil structure was generated for the peptide. Two Cu^{2+} centers, Cu-site1 and 2, were covalently attached to the N_δ of His69 and His85 respectively. Then, the amide nitrogens of Gly70 and Gly71 were chosen to bind ionically to Cu-site 1, whereas the amide nitrogens of Gly86 and Gly87 bind to Cu-site 2. The N_δ of the imidazole of His61 and His77 are linked to Cu-site 1 and 2 respectively, by means of distance restrains. In both sites, a water molecule served as a weak axial fifth ligand.

A special simulated annealing protocol was applied involving cooling from 3000 K to 300 K while switching slowly from a solely ionic Cu^{2+} interaction to a covalently bound Cu^{2+} ion (Mentler et al., 2005). In this way, a feasible prototype can be built. Subsequently, it was used to generate 5000 conformations using the complete MM force field for such copper complexes and standard simulated annealing procedures. The number of these conformations can be reduced to 100 structures if only the structures compatible with the force field (low energy) and certain restrains inferred from the experimental spectra (e.g. distance of ligands or planarity of the copper complex) are considered.

The EXAFS spectra of the remaining conformations (100) were simulated taking into account up to five scattering processes. The multiple scattering contributions of the simulated EXAFS signals are strongly influenced by the particular position of atoms in the second and third coordination spheres around the copper center, especially by the N_ε of the imidazole ring of histidine residues bound to the copper ion. Five structures from the preceding group of conformations show EXAFS simulations in close agreement with the experimental spectrum and were thus selected for further refinement. After choosing a random velocity distribution representing a 400 K

ensemble, a subsequent short 100 ps MD run followed by an energy minimization was carried out and 5 times, generating a total of 500 structures.

Once again, the selection criteria above described was applied. This resulted in 50 conformations which EXAFS simulations fit reasonably well the experimental spectrum of hPrP(23–231). For each of these structures, the proton positions in respect to the two copper centers can be determined and consequently, used to simulate their corresponding ENDOR spectra. The simulations are then compared with the experimental spectrum of hPrP(23–231). The conformation that gives the best fit of the ENDOR spectrum is shown in Figure 6.2.
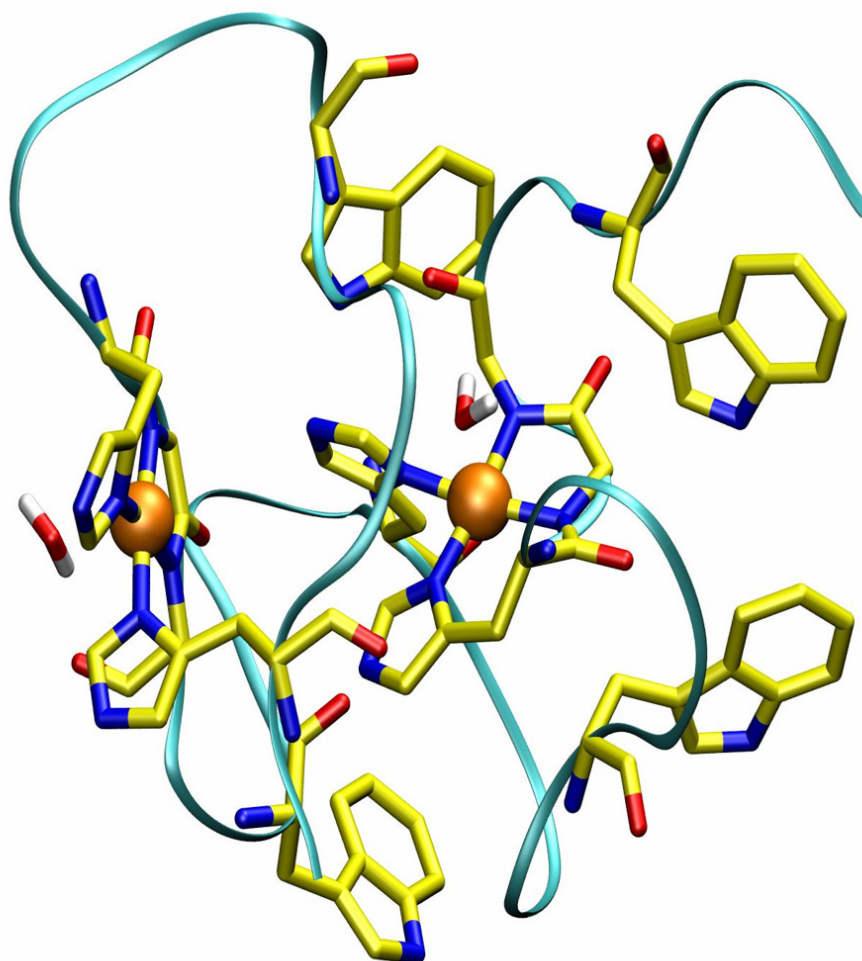
Figure 6.2: Representation of the proposed model. This conformation was used to simulate and validate our EXAFS, EPR and ENDOR experimental data.

This model allow us to simulate quite well the EXAFS spectra of hPrP(23–231) with 2.7 Cu^{2+} as can be seen in Figure 6.3. Table 6.1 contains the first ligand distances of the copper centers shown in Figure 6.2.
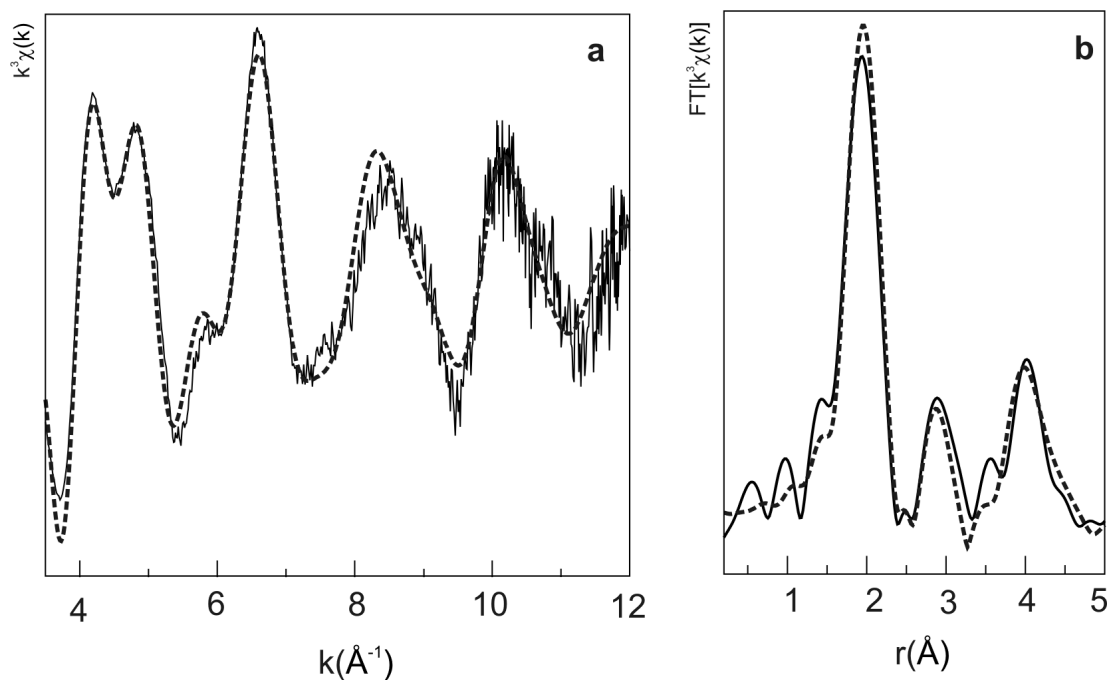
Figure 6.3: (a) k^3–weighted EXAFS spectra of the hPrP(23–231)/2.7Cu^{2+}; (b) Corresponding Fourier transform. Solid lines: experimental data. Dashed lines: simulation of the final model shown in Figure 6.2.

Copper-site 1		Copper-site 2	
Ligands	Cu^{2+} - Ligand (Å)	Ligands	Cu^{2+} - Ligand (Å)
^{61}His N_δ	1.97	^{85}His N_δ	1.96
^{69}His N_δ	1.97	^{77}His N_δ	1.97
^{70}Gly NH	2.01	^{86}Gly NH	2.00
^{71}Gly NH	2.04	^{87}Gly NH	2.04
H_2O O	2.27	H_2O O	2.27

Table 6.1: Cu^{2+}-ligand distances.

Given the proposed model, the protons sited within a sphere of radius 5 Å around the two Cu^{2+} centers are summarized in Table 6.2. This set of protons gives a ENDOR simulation that corresponds perfectly to the ENDOR spectra of hPrP(23–231)/2.7Cu^{2+} (Figure 6.4).

Copper site 1			Copper site 2		
Residue ^{1}H	Cu^{2+}-^{1}H (Å)	angle (deg)	Residue ^{1}H	Cu^{2+}-^{1}H (Å)	angle (deg)
^{61}His HB1	3.55	40	^{77}His HB1	3.10	38
^{61}His HB2	2.97	34	^{77}His HB2	3.09	31
^{61}His HE1	3.05	47	^{77}His HE1	3.14	50
^{69}His HA	3.02	69	^{85}His HA	2.60	40
^{69}His HB1	4.34	71	^{85}His HB1	4.47	68
^{69}His HB2	3.06	53	^{85}His HB2	4.09	88
^{69}His HE1	3.27	74	^{85}His HE1	3.19	70
^{70}Gly HA1	3.69	77	^{86}Gly HA1	3.60	72
^{70}Gly HA2	3.55	75	^{86}Gly HA2	3.64	79
^{71}Gly HA1	3.20	76	^{87}Gly HA1	3.21	84
^{71}Gly HA2	4.03	84	^{87}Gly HA2	3.97	78
H_2O H1	2.96	15	H_2O H1	2.98	16
H_2O H2	2.55	30	H_2O H2	2.47	37
^{61}His HE2	4.96	73	further than 5 Å and then, they are not considered		
^{62}Gly HN	4.57	25			
^{77}His HE2	4.17	50			
further than 5 Å and then, they are not considered			^{62}Gly HA1	3.92	35
			^{81}Trp HA	4.47	63
			^{81}Trp HB1	4.13	59
			^{81}Trp HB2	4.47	37

Table 6.2: Protons considered in the simulation shown in Figure 6.4. For the two copper sites, the position of each proton is specified (angle and distance).
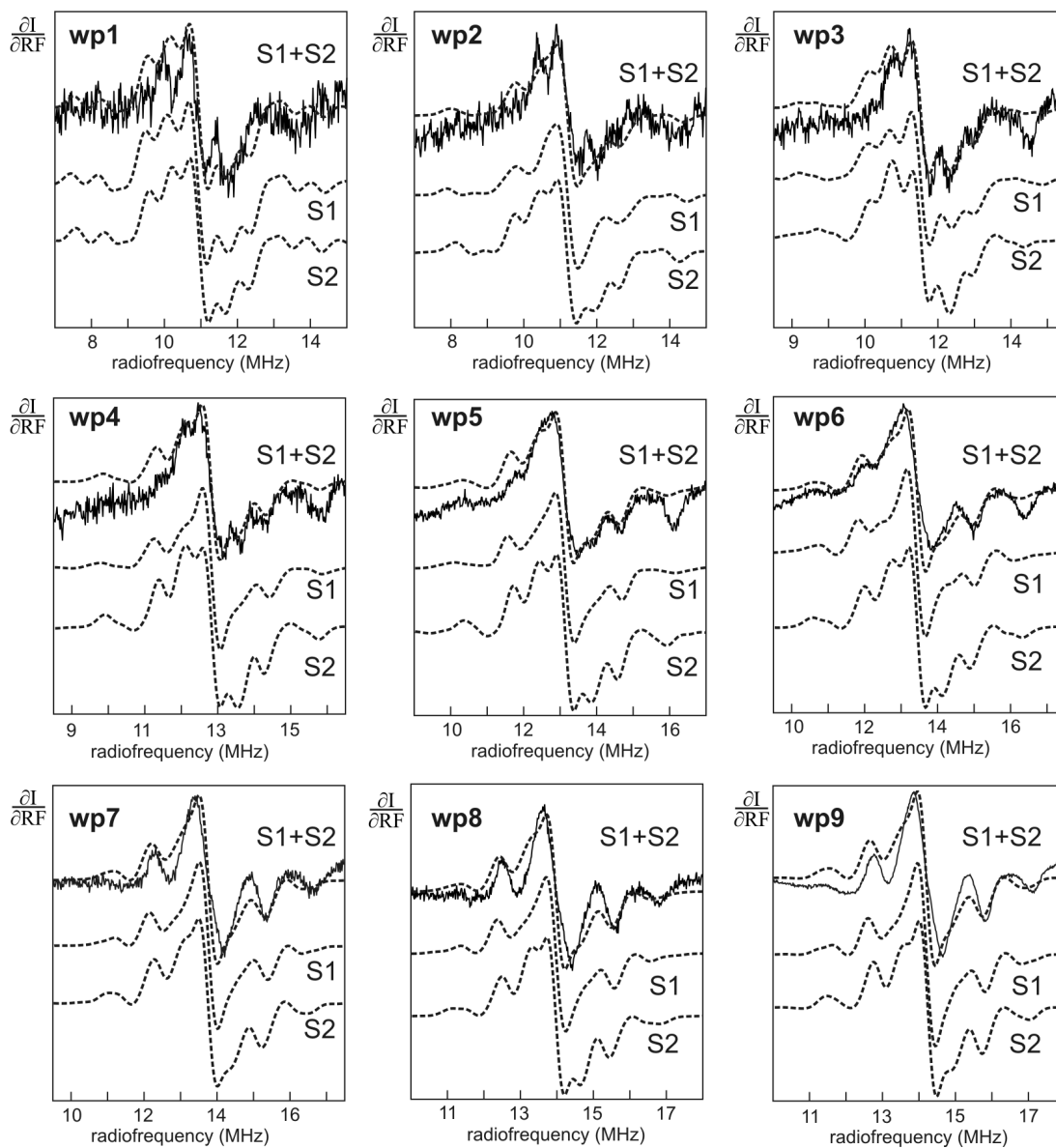
Figure 6.4: Solid line: ENDOR spectra of the hPrP(23–231)/2.7Cu^{2+}. Dashed line S1+S2: simulation of the proposed model. Dashed lines S1 and S2: simulations of each copper site of the model shown in Figure 6.2.

The structure shown in Figure 6.2 is in best agreement not only with ENDOR but with all spectroscopic data without violating standard bond lengths or angles.

Discussion

<div style="text-align: right">

7

</div>

7.1. Copper Configurations: Species I, II and III.

It should be emphasized here that each histidine residue within the N-terminal domain of PrP^C is a possible Cu^{2+} binding place. Therefore, in samples of the recombinant hPrP(23–231), the tetraoctapeptide hPrP(60–91), the mutant HG of MmPrP(23–231), and the octapeptide or pentapeptide, six, four, two and one Cu^{2+} center(s) can be occupied respectively. In the course of our investigations, we have identified three clearly distinguishable copper configurations among the samples. They were referred to as species I, II and III. It should be emphasized here, that we succeeded in the preparation of samples where the Cu^{2+} complexes show a defined species type (I, II, or III). Therefore, these species can be analyzed independently.

Within the group of studied samples, our EPR data turned out to be very helpful to distinguish coordination ligands and geometry of the Cu^{2+} complexes present in the samples. Among the EPR spectra we could identify four different hyperfine patterns, namely species I-*LpH*, I, II and III. Species I-*LpH* is present as a minor component at pH values below 7.0. However, at the pH range used to collect the EPR spectra, this component appears to always accompany species I. Therefore, it will not be discussed in detail.

In principle, the Peisach-Blumberg correlations connect hyperfine parameters with the type of Cu^{2+} ligands in a map. This representation is based on the ratio $g_\parallel / A_\parallel$ of different model compounds for which structure and charge are very well known (Peisach and Blumberg, 1974). Unfortunately, the information is ambiguous in our case since species I, II, and III are compatible with 4 nitrogen (4N), 3 nitrogen and 1 oxygen (3N-1O), 2 nitrogen and 2 oxygen (2N-2O), 1 nitrogen and 3 oxygen (1N-

3O) ligands (see Figure 7.1). In addition, weak five- or six-fold coordinations along the *z*-axis cannot be excluded. Note that species I-*LpH* is not compatible with a 4N configuration and its position in the Peisach-Blumberg map indicates that this component forms a Cu^{2+} geometry involving less nitrogen ligands than the other three species. The contribution of Species I-*LpH* to the overall spectrum decreases with elevated pH (Figure 5.3). This is compatible with the fact that nitrogen ligation in peptide-Cu^{2+} complexes increases with elevated pH.
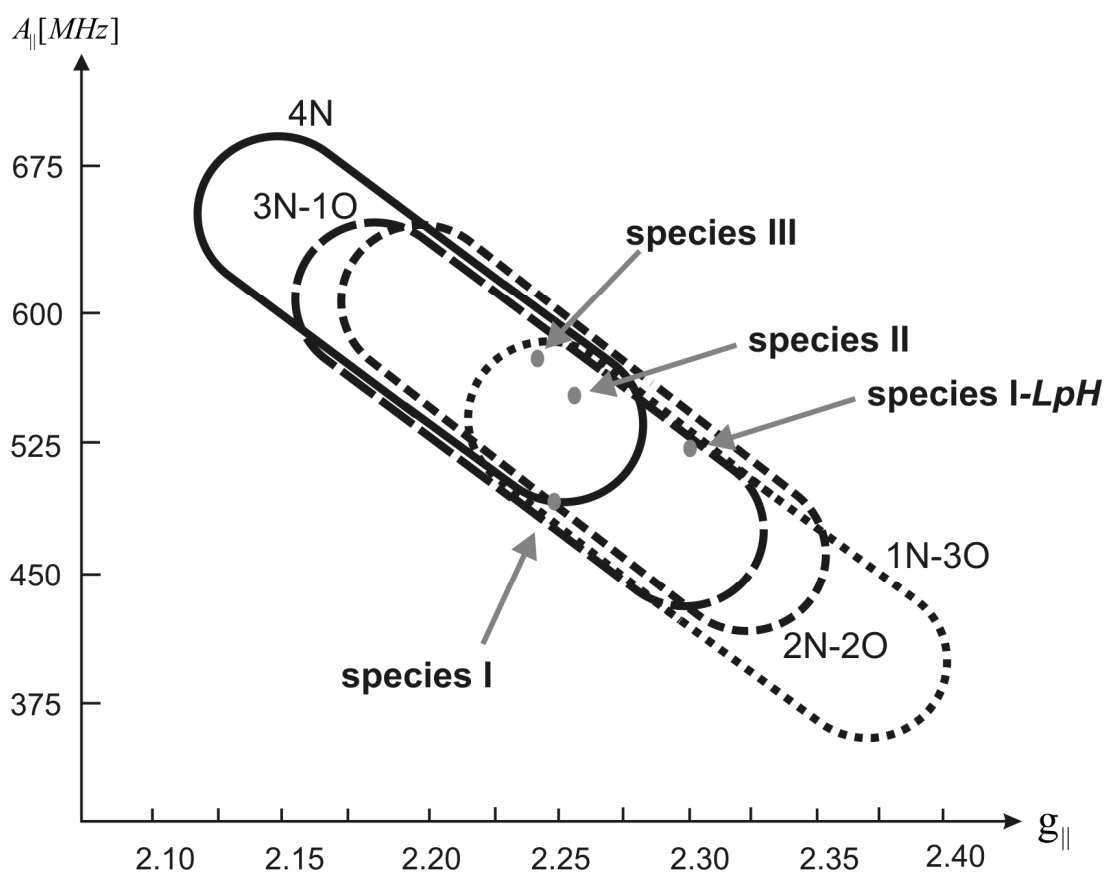
Figure 7.1: The Peisach-Bunberg correlations. Grey solid points: species I, II, III and I-*LpH*.

Figure 7.2 shows selected EPR spectra of the octapeptide–Cu^{2+} (A), the hPrP(23–231)–2.7Cu^{2+} (B) and the mutant HG of the MmPrP(23–231)–Cu^{2+} (C) which are representative samples of species I, II and III, respectively. The high-field region of the EPR spectra is shown in Figure 7.3.

Species I is well known in the context of the octarepeat PrP(60–67) in complex with one Cu^{2+} ion (Mentler et al., 2005). It is characterized by a planar copper complex

with three nitrogen and one oxygen ligands as well as an axial oxygen from a water molecule. In the resulting model determined in this work (Mentler et al., 2005), the N_δ of the His61 acts as a nitrogen ligand, as well as two amide nitrogens of the adjacent glycine residues namely Gly62 and Gly63. The square planar configuration is completed by the carbonyl oxygen of Gly63. This 3N–1O configuration simulates the EPR spectrum of the octapeptide sample very well and especially the high field region (spectrum A in Figure 7.2 and Figure 7.3 respectively).
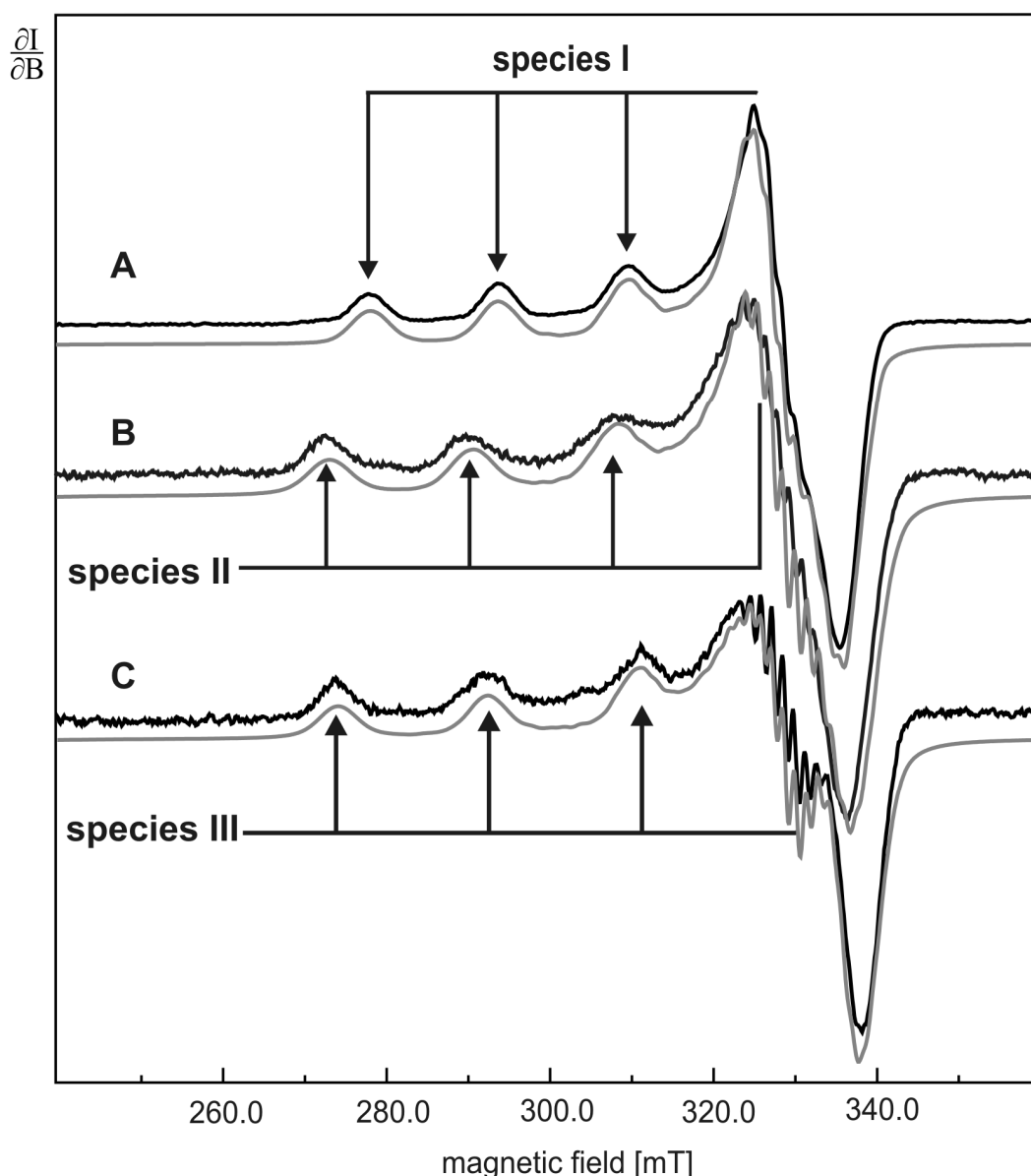
Figure 7.2: Black lines: X-band EPR spectra of the octapeptide–Cu^{2+} (A), the hPrP(23–231)–2.7Cu^{2+} (B) and the mutant HG of the MmPrP(23–231)–Cu^{2+} (C). Grey lines: simulated spectra of these samples. The corresponding simulation parameters are given in Table 5.1.

The superhyperfine structure can help us to solve the uncertainty about the number of nitrogen ligands in the species found in our analysis. The multiplicity of the lines in the superhyperfine structure is proportional to the number of nitrogen ligands (Figure 7.3).
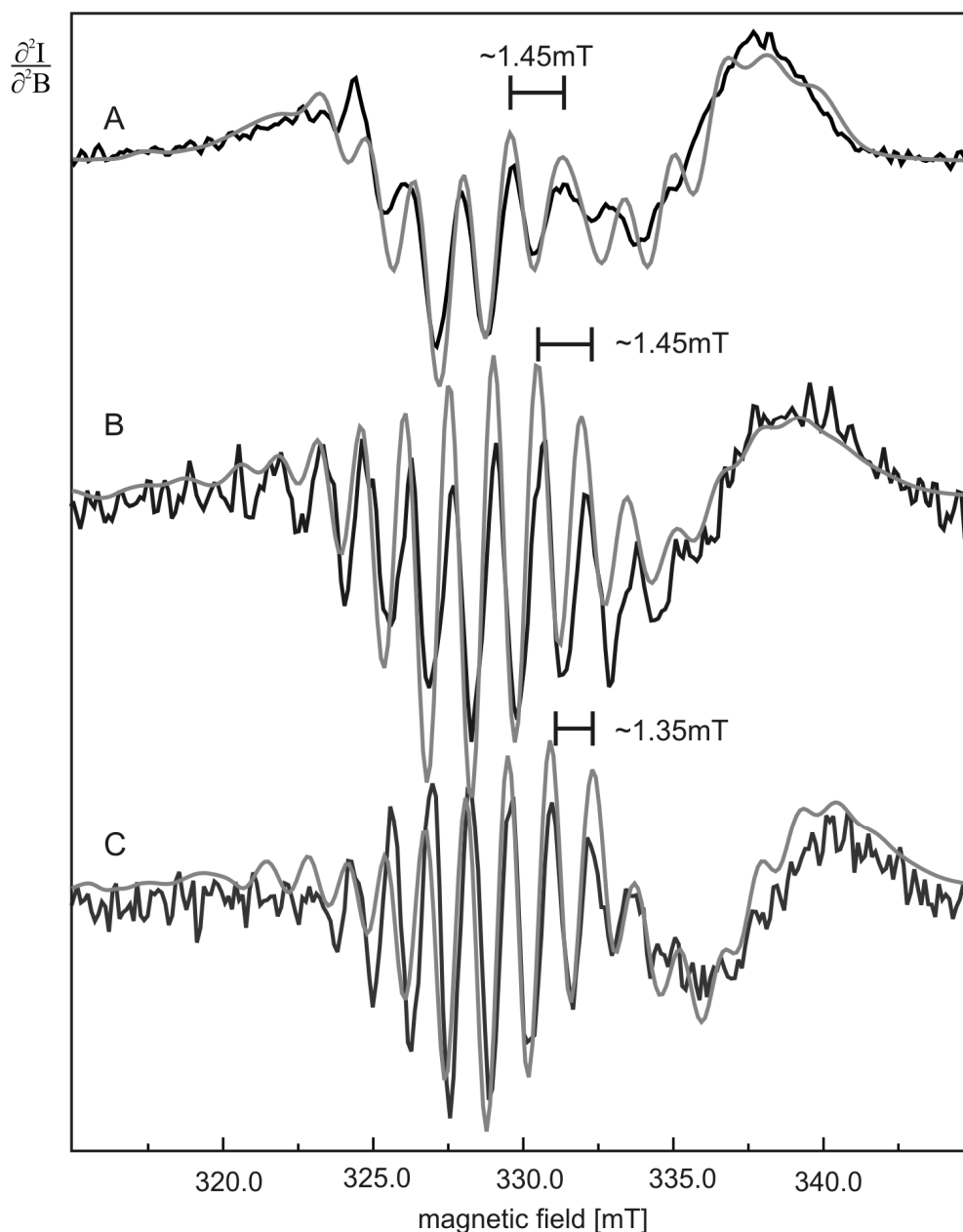
Figure 7.3: High field region of the EPR spectra of the octapeptide–Cu^{2+} (A), the hPrP(23–231)–2.7Cu^{2+} (B) and the mutant HG of the MmPrP(23–231)–Cu^{2+} (C). Grey lines: simulated spectra of planar coordinations with three nitrogen ligands for the octapeptide–Cu^{2+} (A) and four nitrogen ligands for the hPrP(23–231)–2.7Cu^{2+} (B) and the mutant HG of the MmPrP(23–231)–Cu^{2+} (B and C, respectively). The corresponding simulation parameters are given in Table 5.1.

In species I and II, the splitting of the superhyperfine lines is about 1.45 mT whereas species III exhibits a splitting of about 1.35 mT. These values are in agreement with previously reported superhyperfine splitting values for nitrogen coordination in Cu^{2+} complexes (Katterle et al., 2002; Lemos et al., 2000; Scholl and Hüttermann, 1992; Yuan et al., 1999). On the other hand, species II and III show the same multiplicity of superhyperfine lines. Since it is well known that species I is coordinated via a 3N–1O configuration (Burns et al., 2002; Mentler et al., 2005), the increase of the superhyperfine lines from species I to species II/III strongly indicates an increase of the nitrogen ligands from three to four. Furthermore, planar coordinations with three and four nitrogen ligands closely simulate the experimental data (compare Figures 7.2 and 7.3) for species I (A) and species II/III (B and C), respectively.

Figure 7.4 shows the ENDOR spectra of the octapeptide–Cu^{2+} (A), the hPrP(23–231)–2.7Cu^{2+} (B) and the mutant HG of the hPrP(23–231)–Cu^{2+} (C) which are representative samples of species I, II and III, respectively. Inspection of the ^{1}H–ENDOR resonances reveals a similar ^{1}H environment of the Cu^{2+} complexes for species I, II, and III. However, each species displays a rather different intensity pattern. In the hPrP(23–231)–2.7Cu^{2+} complex (B), the ratio between the line resulting from weakly coupled protons (e.g., grey area centred around ν_L at wp9) and the side resonances (e.g., solid arrows at wp9) is smaller than the intensity ratio observed for the octapeptide–Cu^{2+} (A). This ratio difference is even more pronounced in the case of the mutant HG of the MmPrP(23–231)–Cu^{2+} (C) in comparison to the other spectra.

According to the EPR data species I and II differ in the number of coordinating nitrogens (3N and 4N, respectively). In addition, ENDOR data bring out a similar ^{1}H environment of the Cu^{2+} complexes for species I and II, although with a different intensity pattern. If one combines all these data, it can be concluded that species I and II bear different imidazole coordination. Since in species I a single imidazole participates in the Cu^{2+} coordination, one can assume that species II binds to two imidazole nitrogens. This interpretation is supported by the fact that the main intensity differences of the ENDOR spectra are found at resonances expected to stem from imidazole hydrogens (see solid arrows at wp9).
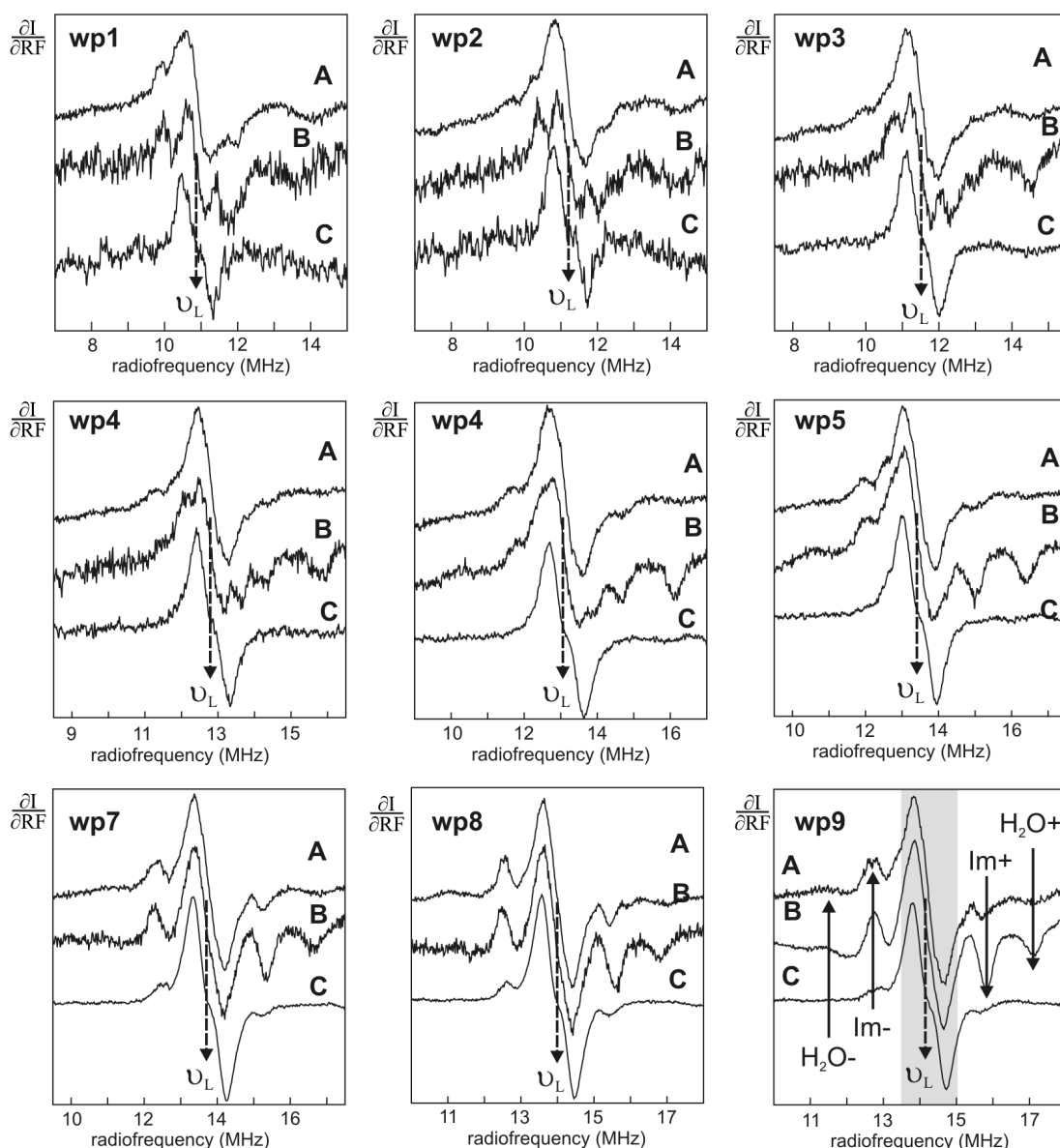
Figure 7.4: ENDOR spectra of the octapeptide–Cu^{2+} at pH 7.2 (A), the recombinant hPrP(23–231) at pH 7.0 loaded with 2.7 Cu^{2+} equivalents (B), and the mutant HG of the MmPrP(23–231) with one Cu^{2+} equivalent (C). The spectra were taken at 9 different magnetic fields (wp1 to wp9). Broken arrows point at the ^{1}H nuclear Zeeman frequency (υ_L). At the wp9, the grey area marks the influence region of weakly coupled protons. Solid arrows point at resonances expected to stem from imidazole hydrogens (Im+ and Im-) and axial water (H_2O+ and H_2O-).

In previous investigations of our laboratories regarding the octapeptide–Cu^{2+} complex, [1]H–resonances were associated to axial water by means of comparison with an analogous deuterated sample (Mentler et al., 2005). The ENDOR spectra of the hPrP(23–231)–2.7 Cu^{2+} complex shows these resonances as well (see solid arrows at wp9). Therefore, it can be assumed that in species II a water molecule participates as

the axial ligand in the Cu^{2+} coordination. The ENDOR spectra of the mutant HG of MmPrP(23–231) with one Cu^{2+} equivalent and the octapeptide–Cu^{2+} complex are very similar, even in respect to the intensity pattern (spectra A and C in Figure 7.4). Therefore, it can be assumed that species I and III share a rather similar ^{1}H environment, although the [1]H–resonances which were associated to binding of axial water are missing for species III. Moreover, EPR data reveals that species I and III differ in the number of coordinating nitrogens (3N and 4N respectively). One can then conclude that in species III only one imidazole nitrogen participates in the Cu^{2+} coordination. The square-planar 4N configuration is completed by amide nitrogens.

In samples which show species II type spectra, the EXAFS data strongly support the coordination of the Cu^{2+} centers by two histidyl imidazoles. Figure 7.5a shows the EXAFS spectra of samples representative of species I and II, namely the octapeptide–Cu^{2+} (A) and the hPrP(23–231)–2.7Cu^{2+} (B) respectively. Figure 7.5b displays their corresponding Fourier transforms. Unfortunately, we did not succeed in recording a reliable EXAFS spectrum of the mutant HG of MmPrP(23–231) because the sample was highly contaminated by copper hydroxide (data not shown). Therefore, the EXAFS spectra associated to species III is missing.
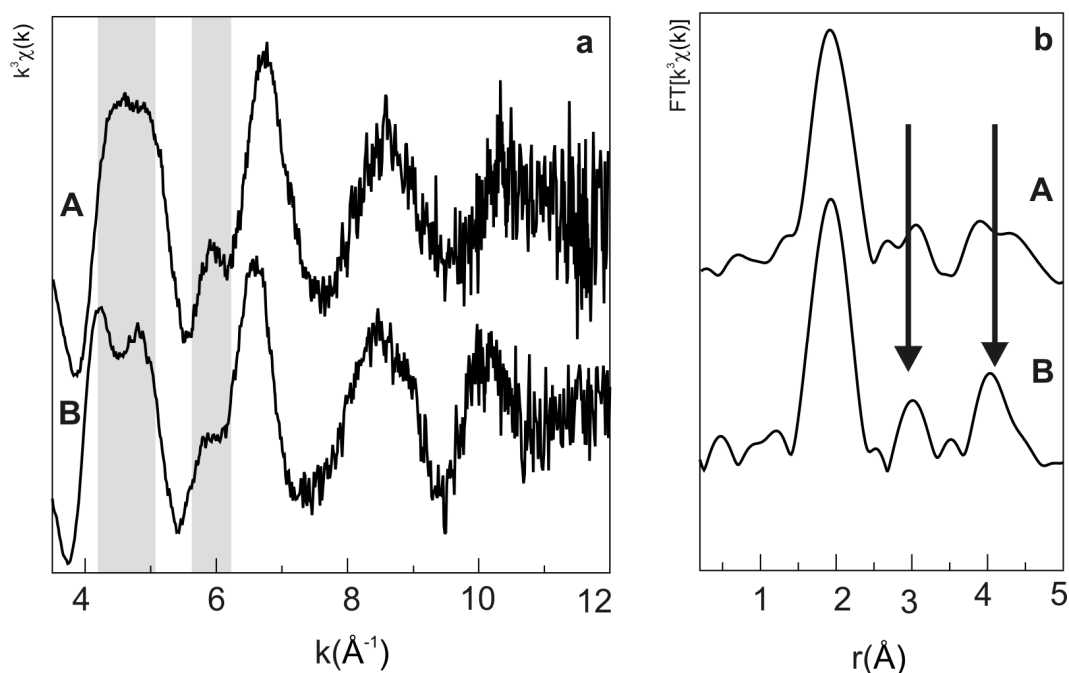
Figure 7.5: (a) k^3–weighted EXAFS spectra of the octapeptide–Cu^{2+} (A), and the hPrP(23–231)–2.7Cu^{2+} (B); (b) Corresponding FT of the EXAFS spectra of A and B.

EXAFS oscillations are very sensitive to distance of first ligands and imidazole coordination of the Cu^{2+} complex. Indeed, EXAFS spectra associated to species I and II exhibit differences in some regions, although both share a similar main oscillation. The features in the regions 4.5–5.0 $\overset{\circ}{A}{}^{-1}$ and 5.7–6.2 $\overset{\circ}{A}{}^{-1}$ (spectra A and B within the grey areas in Figure 7.5a), as well as the peaks at approximately 3 and 4 $\overset{\circ}{A}$ in the Fourier transforms (Figure 7.5b) are typical of multiple scattering by imidazole rings. The amplitude of the peaks in the Fourier transform (solid arrows in Figure 7.5b) is enlarged in species II in comparison to species I. In the case of species II, these features give another strong support for the Cu^{2+} coordination by two histidyl imidazoles (Arnesano et al., 2003a; Arnesano et al., 2003b; Hasnain et al., 2001).

7.2. Model of hPrP(23–231) with Two Cu^{2+} Centers.

The structure of species I in the context of the octarepeat peptide, hPrP(60–67), was solved with atomic resolution through the use of a newly developed method previously described by Mentler (Mentler et al., 2005). This method combines spectroscopic data from EPR, ENDOR, and EXAFS, with computations that allow us to obtain a model compatible with the experimental data. In a similar fashion, taken the experimental evidences previously introduced, a model for species II in the context of the hPrP can be produced (Figure 6.2). It should be noted here that in contrast to other studies, where Cu^{2+} binding to PrP-derived peptides is treated as an equivalent model for Cu^{2+} binding to full-length PrP, our investigation was essentially performed on the recombinant hPrP(23–231) in complex with $^{63}Cu^{2+}$. At neutral and slightly basic pH values, the full-length hPrP(23–231) is poorly soluble. It impedes the structure determination of the fully Cu^{2+} saturated binding sites of PrP in solution. Cu^{2+}-binding to PrP is optimal at pH about 7.4 where five or six Cu^{2+} centers bind to the N-terminal domain of PrP (Brown et al., 1997). Therefore, we chose to add Cu^{2+} to hPrP(23–231) at pH 6.0 and 7.0 at peptide-concentration conditions such that aggregation of PrP is prevented. In the next step, the hPrP/Cu^{2+} complexes were precipitated by addition of ammonium sulfate. The so obtained samples of hPrP in complex with Cu^{2+} yielded experimental spectra with a good signal to background ratio, although at these pH values, the copper sites of PrP are not saturated.

Precipitation processes can affect the folding of the peptide/Cu^{2+} complex. To check the intactness of the peptide/Cu^{2+} fold after precipitation, we recorded an EXAFS spectrum of the hPrP(23–231)/1.3 Cu^{2+} complex in solution at pH 6.0. This spectrum exhibits very low signal-to-noise ratio, although the main oscillation observed in the precipitated samples is still distinguishable (Figure 5.16, spectrum C). There was no hint for any interference of the precipitation procedure with the structure of the copper binding sites and then, our approach based on hPrP/Cu^{2+} complexes in their precipitated forms is legitimate.

In our proposed model, one Cu^{2+} coordinates to two histidines of two octarepeats and therefore, we can only bind two Cu^{2+} ions in the octarepeat region. Here, it should be emphasized again that the reported Cu^{2+} loads for hPrP(23–231) in their precipitated forms (1.7 and 2.7) are upper limits which results of an indirect measurement[11]. These values can be actually lower. Still, it has to be addressed, how the hPrP actually binds non-integer copper amounts. In theory, hPrP molecules can bind one, two, three and/or four Cu^{2+} centers in the octarepeat region, some molecules can even remain Cu^{2+} free. One can then expect an equilibrium of molecules with different copper loads. In respect to the hPrP and tetraoctapeptide samples, our findings indicate that this equilibrium strongly depends upon the Cu^{2+} load, pH value and buffer system. At low and intermediate Cu^{2+} occupancy, the species II type of copper binding is favored, whereas at saturation of the Cu^{2+} sites in the octarepeat domain the species I type dominates. However, it must be stressed that we did not succeeded in the preparation of samples of recombinant hPrP(23–231) where all possible Cu^{2+} centers were occupied.

In this context, for the sample of hPrP with 1.7 Cu^{2+} equivalents, it can be assumed that in their molecules, one or two Cu^{2+} centers are occupied as species II type. This hypothesis is supported by the fact that tetraoctapeptide molecules coordinated with one Cu^{2+} center show species II type spectrum independently of the buffer system. On the other hand, the EPR spectra of the sample with 2.7 Cu^{2+} exhibit essentially species II, although obviously our model can explain only two Cu^{2+} sites. Therefore, the most plausible hypothesis is to assume a equilibrium of species mixture where

---

[11] Chapter 4: Sample Preparation

65% of the molecules bind two Cu^{2+} centers as species II type and in the remaining 35% of molecules, the four copper sites consists of species I type. Here, one has to bear in mind that indeed, the EPR of tetraoctapeptide samples close to Cu^{2+} saturation (three or four Cu^{2+} equivalents) show generally tendency to bind Cu^{2+} as species I (compare spectra c and d in Figure 5.5). However, a contribution of 35% molecules binding as species I is not compatible with the EPR spectrum of hPrP(23–231)–2.7Cu^{2+}. The EPR estimations shown in Figure 5.10 indicate that the signal of species I type complexes should be less than 20% of the overall spectrum. Furthermore, assuming the same contributions of species I and II as used for the EPR estimations, EXAFS simulations are also compatible with our experimental data (Figure 7.6). To simulate these EXAFS estimations, we have taken our proposed model as species II, and for species I, we assume the coordination obtained for the octapeptide-Cu^{2+} complex (Mentler et al., 2005).
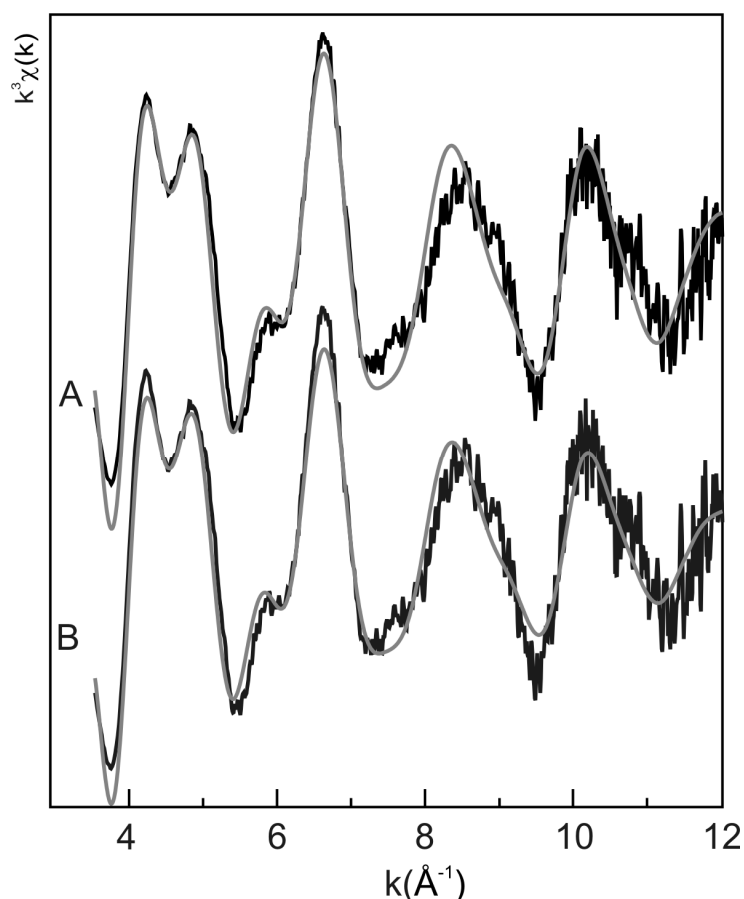
Figure 7.6: Estimation of the influence of a species I contribution in the EXAFS spectrum of hPrP(23−231)−2.7Cu^{2+}. Black line: EXAFS spectrum of hPrP(23−231)−2.7Cu^{2+}. Grey broken lines: simulations with 100% species II (A) and a mixture of 80% species II plus 20% species I (B).

At this point of our discussion about the 2.7 Cu^{2+} in hPrP, the Cu^{2+}-balance is still not even. However, as already mentioned the 2.7 Cu^{2+} load is an upper limit because it is the result of an indirect measurement. The presence of copper hydroxide precipitate cannot be ruled out. At pH 7.0, aquo Cu^{2+} is only sparingly soluble and precipitates as copper hydroxide which is EPR silent (Aronoff-Spencer et al., 2000; Cereghetti et al., 2001). And hence, the peptide-unbound Cu^{2+} does not contribute to the EPR or ENDOR spectra. In contrast to EPR or ENDOR, EXAFS should be able to detect any copper signal, independently whether it is paramagnetic or not. Although we did not find a significant contribution of copper hydroxide in our EXAFS spectra, we nevertheless addressed this issue by adding increasing contributions of copper hydroxide to the simulated EXAFS spectra derived from our proposed model (Figure 7.7).
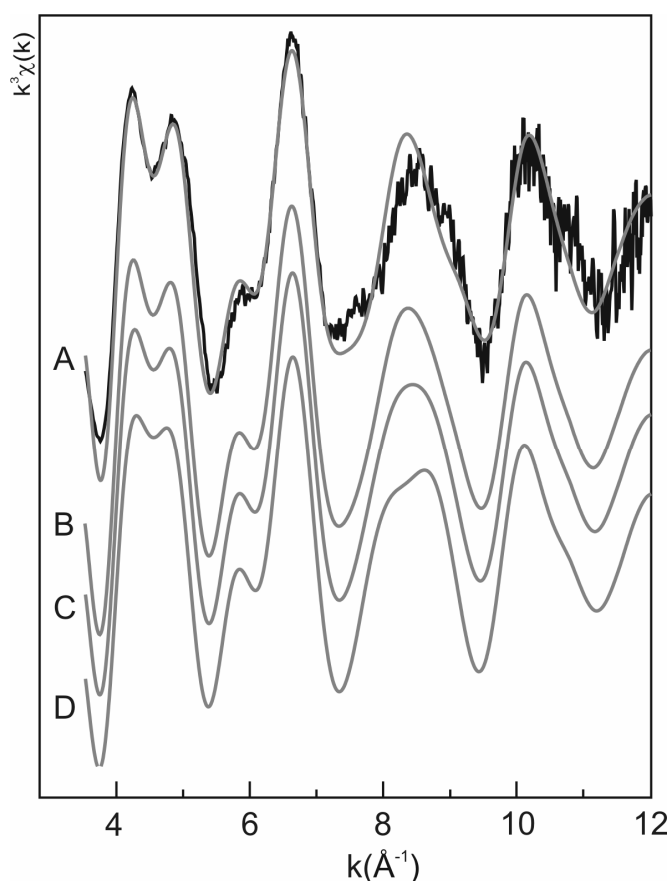
Figure 7.7: Estimations of the influence of copper hydroxide in the EXAFS spectrum of the hPrP(23–231) at pH 7.0 with 2.7 Cu^{2+} equivalents. Black line: k^3–weighted EXAFS spectrum of the sample. Grey lines: Simulations of 2 Cu^{2+} as species II and additionally 0.0 copper hydroxide (A), 0.25 copper hydroxide (B), 0.4 copper hydroxide (C), and 0.7 copper hydroxide (D).

Simulations of EXAFS spectra with different copper hydroxide amounts reveal that we can not exclude a contribution of up to 0.25 (out of 2.7) equivalents of copper hydroxide, which makes no significant change of the EXAFS simulation.

7.3. Cu^{2+}-Binding Outside of the Octarepeat Region.

Regarding the copper binding sites involving histidine residues which do not belong to the octarepeat region, in samples of the hPrP(23–231), we do not find any evidences of copper binding to histidine residues at the positions 96 and/or 111, as proposed by several independent studies (Burns et al., 2003; Jones et al., 2004; Wells et al., 2006a; Wells et al., 2006b). The EPR spectra of hPrP(23–231) essentially exhibit species II and therefore, we can assume a common first coordination shell for the Cu^{2+} complexes in the octarepeat domain and reject additional copper sites. It should be emphasized that at the conditions used for the samples of hPrP, not all the possible copper sites are occupied. Our findings indicate that the affinity of the Cu^{2+} sites within the octarepeat domain is greater than in putative sites involving histidine residues at the positions 96 and/or 111.

We addressed the non-octarepeat Cu^{2+}-binding site(s) by measuring the mutant HG of MmPrP(23–231) with one Cu^{2+} equivalent, where the histidine residues of the octarepeat units are substituted by glycine residues and therefore, Cu^{2+} binding in the octarepeat domain is prevented. At this point, it should be emphasized again that in the N-terminal domain of the mutant HG of MmPrP only two histidine residues, His96 and His111, are available for copper binding. The investigation of the mutant HG of MmPrP(23–231) was carried out in precipitated material because this sample showed similar problems of solubility as the hPrP(23–231). Unfortunately, the EXAFS spectrum of this sample is not reliable due to the presence of unbound-peptide Cu^{2+}. In this case, the methodology previously discussed for species II could not be applied satisfactorily. However, a considerably body of experimental data is available. Their hyperfine and superhypefine patterns indicate a 4N square-planar geometry that is different to either species I or II, and it was solely

observed in this sample. ENDOR data suggest that the copper center is coordinated only by one imidazole ring and most likely, the 4N coordination is completed by backbone amide nitrogens. The definitive proof for this hypothesis should be the EXAFS spectrum of the corresponding sample.

7.4. Comparison with Literature.

The pioneering work of Brown demonstrated that PrP binds Cu^{2+} *in vivo* (Brown et al., 1997). Thereafter, the copper binding sites of PrP^C and PrP^C-derived peptides, either their affinities or coordination, have been widely studied by means of different biophysical and biochemical techniques (see e.g., (Burns et al., 2003; Chattopadhyay et al., 2005; Jackson et al., 2001; Viles et al., 1999). The current consensus about the nature of the Cu^{2+} binding to PrP^C states that at pH 7.4, PrP^C binds up to four Cu^{2+} ions with high affinity in the octarepeat region. Each octapeptide unit is able to bind independently a Cu^{2+} center with coordination of the histidyl imidazole ring and glycine residues (Burns et al., 2003). It has to be noted that this finding is based on studies carried out in synthetic PrP-derived peptides representing the octarepeat domain. The question that remains to be addressed is whether these synthetic peptides can be considered a complete model for Cu^{2+} binding to the prion protein or if the C-terminal domain plays any role in the folding of the N-terminal domain when it binds Cu^{2+}. Nevertheless, the study of Cu^{2+} binding to PrP-derived peptides is easier than in recombinant PrP because these peptides are more soluble than recombinant PrP at pH values where Cu^{2+}-binding is optimal. As already mentioned, in addition to the copper sites of the octarepeat domain, coordination of one or two Cu^{2+} ions has been contemplated in the region outside of the octarepeat domain, spanning residues 92 to 115 of recombinant hPrP(23-231). However, there is disagreement in literature about these additional binding sites. It remains controversial whether one or two Cu^{2+} ion(s) bind(s) at sites involving histidine residues corresponding to the positions 96 and 111 of hPrP(23–231). Moreover, the reported affinities and coordinating ligands of these additional sites have varied greatly over the years in literature (Brown, 1999; Burns et al., 2003; Hasnain et al., 2001; Jackson et al., 2001; Jones et al., 2004; Kramer et al., 2001).

Recently a number of studies have shown that depending on the Cu^{2+} load and the pH value, the octapeptide domain exhibits multiple modes of Cu^{2+} binding (Chattopadhyay et al., 2005; Valensin et al., 2004; Wells et al., 2006a; Wells et al., 2006b). Therefore, the model consisting of four octapeptide units binding independently a Cu^{2+} center provides an incomplete picture of Cu^{2+} binding to PrP.

A variety of spectroscopic techniques have been applied to investigate the structure of the Cu^{2+} binding sites of PrP^C and as a result, several models of the folding of PrP in the presence of Cu^{2+} have been put forth (Table 7.1).

Reference	Buffer	pH	Peptide Sequence[12]	Technique
(Stöckel et al., 1998)	MES	6.0	SHaPrP(29–231), PrP(57–91), PrP(73–91)	Fluorescence, CD
(Viles et al., 1999)	phophate acetate NEM	7.4	PrP(58–91), PrP(66–91), PrP(76–86), PrP(73–91), PrP(51–75)	NMR, Absorption (UV/visible)
(Burns et al., 2003)	NEM	7.4	SHa(29–231), SHa(90–231), PrP(23–28, 57–98), PrP(90–116), PrP(90–101), PrP(106–116), PrP(92–96)	EPR, ESEEM
(Jones et al., 2004)	none	5.5-9.4	PrP(23-231, Δ51–90), PrP(H111A)[13], PrP(H96A)[14], PrP(91-115), PrP(90-126), PrP(51-96)	CD, NMR, Absorption (Uv/visible)
(Morante et al., 2004)	MES NEM	6.5, 7.4	αBoPrP(24–242), BoPrP(25–30, 60–94), BoPrP(25–30, 60–78), BoPrP(25–30, 60–70)	EXAFS
(Redecke et al., 2005)	MES	6.5	ChPrP(53–58), ChPrP(53–64), ChPrP(53–70), ChPrP(53–76), PrP(60–67), PrP(60–83), PrP(60–91)	EXAFS
(Chattopadhyay et al., 2005)	NEM	7.4	PrP(23–28, 57–91), PrP(60–83), PrP(61–73), PrP(60–67), PrP(61–65), several PrP-derived peptides where some amino acids were substituted	EPR, ESEEM
(Wells et al., 2006a)	MES	5.5	hPrP(23–231), hPrP(91–231)	NMR
(Wells et al., 2006b)	Tris MOPS acetate	7.4	PrP(57–91), hPrP(91–115)	CD, NMR Fluorescence

Table 7.1: List of references including the corresponding sample context and applied technique(s).

Among different studies, the addressed samples differ largely in respect to their sequence context, buffer or Cu^{2+} load. One has to keep this in mind to compare the

---

[12] Unless otherwise specified all sequences of PrP-derived peptides refer to the human PrP.
[13] PrP(91-115) were His111 is replaced by Ala.
[14] PrP(91-115) were His96 is replaced by Ala.

findings of these diverse investigations. In the following, a number of proposed models (not all of them, but the most outstanding contributions) will be discussed and compared with our results. These contributions, the corresponding sample context, as well as the applied spectroscopic method are listed in Table 7.1.

The Cu^{2+} sites of recombinant Syrian hamster PrP, SHaPrP(29–231), and various PrP-derived peptides were investigated by means of fluorescence- and CD-spectroscopy (Stöckel et al., 1998). This early work put forth a model for the Cu^{2+} binding site of SHaPrP(29–231) at pH 6.0 where two Cu^{2+} centers bind in the octarepeat domain (Figure 7.8). Each Cu^{2+} binds to residues of two consecutive octarepeat units. The Cu^{2+} configuration consists of a 2N-2O square planar geometry. The first coordination shell is formed by one histidyl imidazole nitrogen and one glycine carbonyl oxygen of two adjacent octapeptide repeats. The glycine carbonyl oxygen in the middle of the glycine triplet in the octarepeat peptide was chosen because this enabled the Trp residue to come into proximity with the Cu^{2+} center and thus, the quenching of Trp fluorescence upon binding of Cu^{2+} to SHaPrP(29–231) can be explained. Our findings agree with this work in respect to the number of bound Cu^{2+}, and the coordination of the Cu^{2+} binding site by 2 His and 2 Gly residues. However, in our model the glycine carbonyl oxygens are replaced by amid nitrogens.
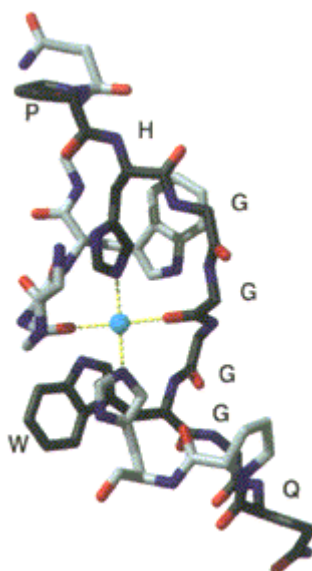
Figure 7.8: Conformation of Cu^{2+} binding to two octarepeat units (reproduced from (Stöckel et al., 1998)).

Absorption-, CD- and EPR-spectroscopy were used to study PrP-derived peptides consisting of to 2-, 3- and 4-octarepeat units with different Cu^{2+} loads (Viles et al., 1999). The peptide PrP(58–91), that includes the full octarepeat domain, with 1, 2 and 3 equivalents of Cu^{2+} was investigated by X-band EPR. The spectra exhibit a quite similar hyperfine pattern as those in our investigation showing species II type. However, the two proposed peptide/Cu^{2+} models differ. They put forth a square planar 3N-1O configuration where the coordinating oxygen stems from a water molecule (Figure 7.9). The water molecule includes two ^1H that are in contradiction to our ENDOR results. We do not find ^1H resonances compatible with coordination of a water molecule in the plane defined by the Cu^{2+} and the ligands. Although in our model two histidines coordinate each Cu^{2+} center as well, we propose a different Cu^{2+} configuration. They claim that, with more than two Cu^{2+} ions, each histidine from the octarepeat domain represents a link between two Cu^{2+} ions, binding through N_δ and N_ε in adjacent octarepeat units. In contrast, in our model only the N_δ participates in the Cu^{2+} binding.
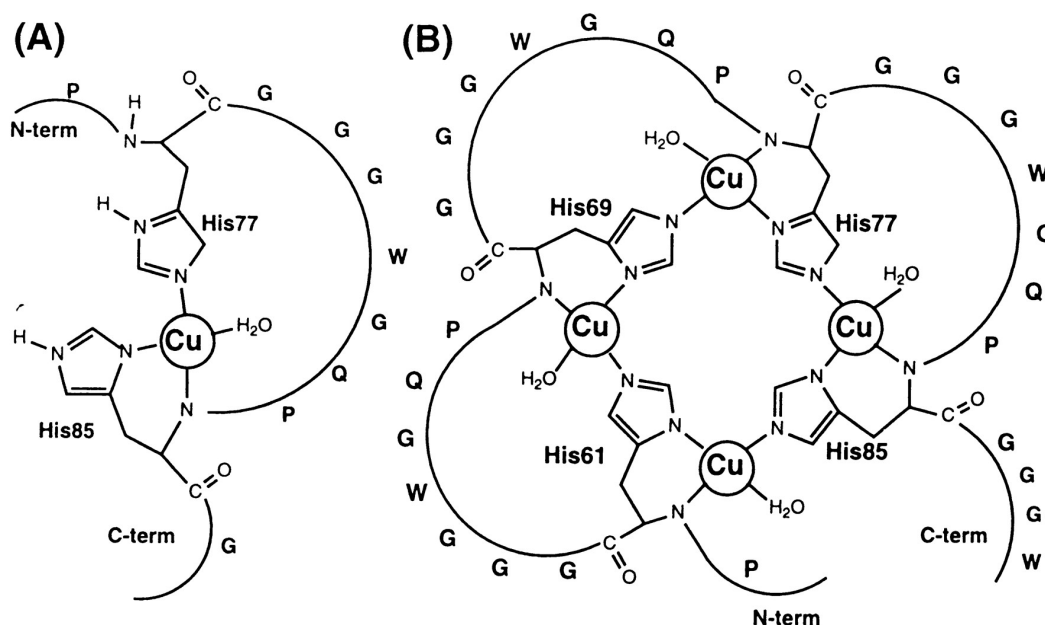
Figure 7.9: (A) Structure for the complex of Cu^{2+} with PrP(76–86) that includes two octarepeat units. (B) Structure for the bridged complex of four Cu^{2+} with PrP(58–91) that includes 4 octarepeat units.

The Cu^{2+} coordination in the full-length recombinant SHaPrP(29–231) was investigated by means of EPR and three-pulse ESEEM (Burns et al., 2003). For comparison, they also studied several PrP-derived peptides that allowed them to identified two different Cu^{2+} binding regions. They found that each octapeptide unit of the octarepeat domain (there are four) binds one Cu^{2+} center as our species I type (Figure 7.10). We partially agree with this result. Our findings concerning the tetraoctapeptide with different Cu^{2+} loads (1, 2, 3 and 4 Cu^{2+} ions) indicate that a mixture of species is present in most of the spectra. Moreover, the species ratio depends on the Cu^{2+} load and buffer system. However, the spectra with three and four Cu^{2+} show a general tendency to species I.
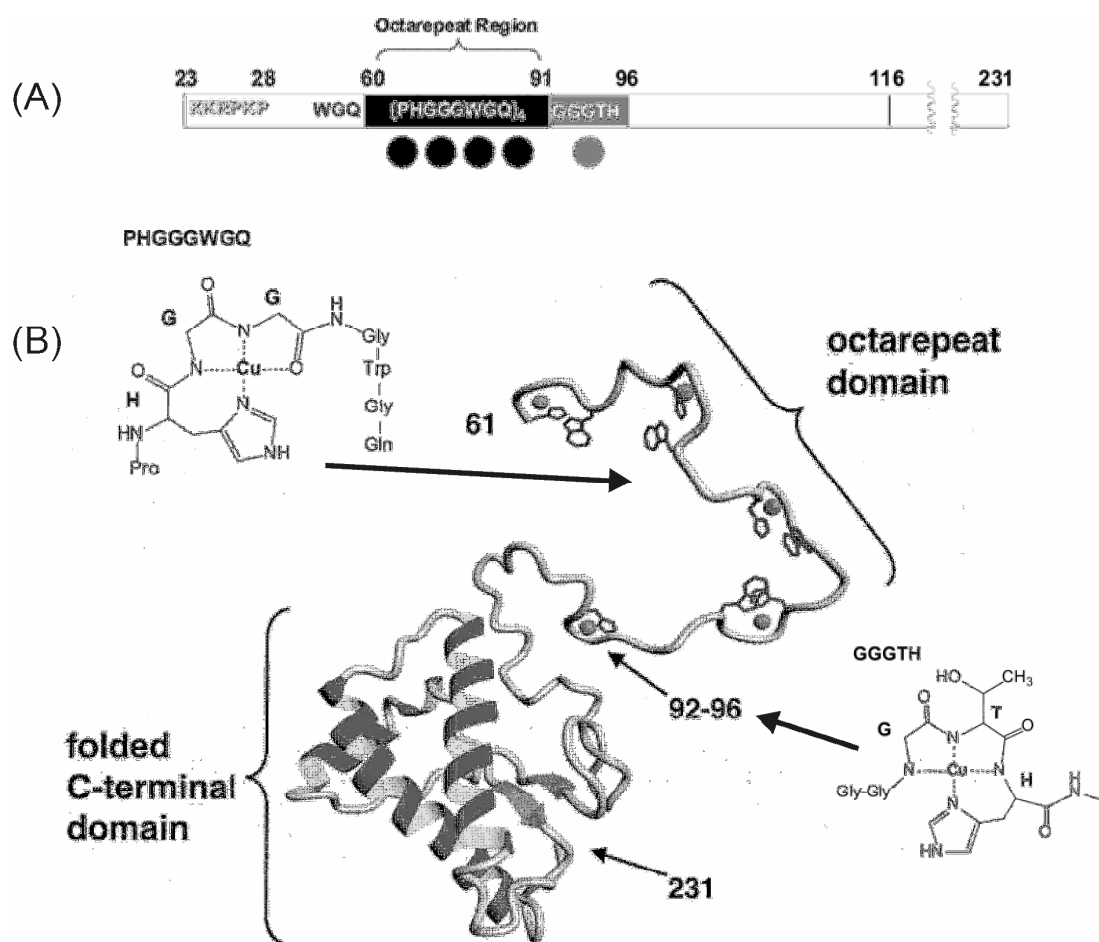
Figure 7.10: (A) Bar diagram of the Cu^{2+} binding sites of PrP; (B) Two different models proposed for the Cu^{2+} sites of the octarepeat domain and the "fifth" binding place (reproduced (Burns et al., 2003)).

In addition, they found that the His96 can bind a fifth Cu^{2+} ion through the N_δ and its backbone amid nitrogen. The square-planar 4N configuration is completed by backbone amid nitrogens of the residues Thr95 and Gly94 (Figure 7.10). The EPR spectrum associated with this fifth binding Cu^{2+} is consistent with our measurement of the mutant HG of the MmPrP(23–231) with one Cu^{2+} ion (species III type) that shows a clear superhyperfine pattern in agreement with a 4N coordination. The superhyperfine features are missing in its spectrum, however, they proposed a 4N configuration as well. We could not determine which residues participates in the fifth Cu^{2+} center, although the coordination proposed by Burns is compatible with our EPR and ENDOR data. Here, one should note that species III only appears in the spectra of the mutant HG of the MmPrP. We did not find any influence of species III in our samples of the hPrP. Most probably, this stems from the fact that our samples are not fully copper saturated.

Regarding the non-octarepeat Cu^{2+} sites, investigations on several PrP-derived peptides by means of CD, EPR, NMR and absorption spectroscopy (UV-visible) have been reported (Jones et al., 2004). They concluded that Cu^{2+} binds preferentially to both His96 and His111, rather than to the octarepeat domain. The proposed model consists of a 4N configuration where two nitrogen ligands belong to His96 and His111, and the remaining coordinating atoms are the backbone amid nitrogens of His96 and Met112 (Figure 7.11). We do not find evidences of Cu^{2+} coordination by His96 or His111 in the hPrP samples. Therefore, our data indicate that the affinity of the Cu^{2+} binding place in the octarepeat region is greater than for the "fifth" binding site in the context of the recombinant hPrP(23–231). On the other hand, our data regarding the fifth binding site (species III) are in agreement with respect to a 4N configuration, although two imidazoles involved in Cu^{2+} binding are inconsistent with our ENDOR spectra of the mutant HG of MmPrP (species III). Furthermore, the EPR hyperfine parameters given for this copper motif are incompatible with any of the species type found in our EPR investigation. Therefore, the described divergences can only be explained by the fact that the sequence contexts were different or maybe, because they performed their investigations in the absence of any buffer.
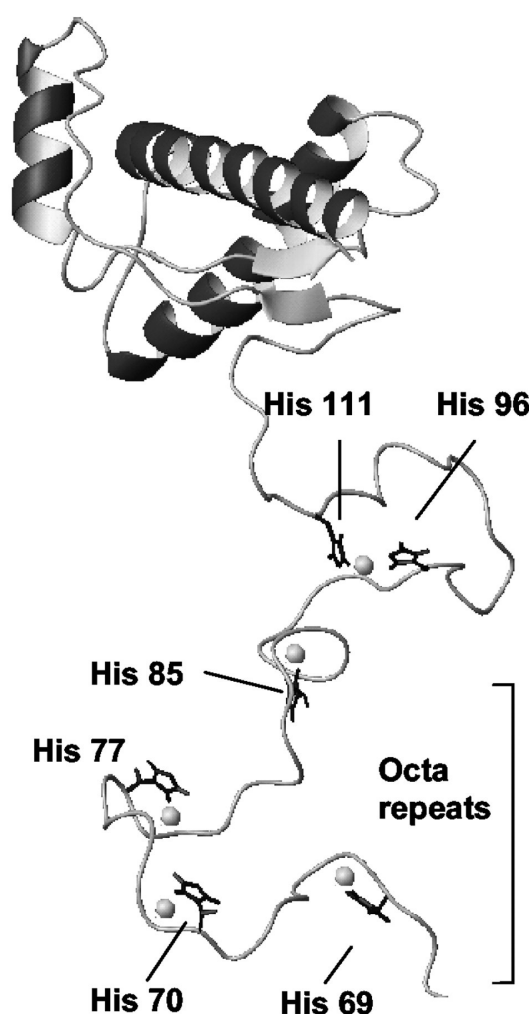
Figure 7.11: Model of PrP(57–231) showing binding positions of five Cu^{2+} ions (reproduced from (Jones et al., 2004)).

In a very "creative" report, Morante addressed a X-ray absorption spectroscopy (XAS) study of the Cu^{2+} binding sites of the αBoPrP(24–242) (Morante et al., 2004). Note that BoPrP has six octapeptide repeats within its octarepeat domain. At half-site Cu^{2+} occupancy, they proposed that the Cu^{2+} binding sites of αBoPrP(24–242) consist of penta-coordinated Cu^{2+} sites with one axially bound water molecule and two equatorial nitrogen atoms from two histidyl imidazole rings. Interestingly, they considered that the coordinating histidine residues can belong to the octarepeat domain of one or two different molecules. And thus, contact between molecules can occur in what they referred to as inter-repeat mode (Figure 7.12). The remaining two equatorial ligands could not be determined unambiguously by this XAS study.

Nevertheless, they considered as possible candidates amid nitrogen or carbonyl oxygen atoms from glycine residues. In this study, we were able to resolve unambiguously the uncertainty regarding the remaining two equatorial ligands.
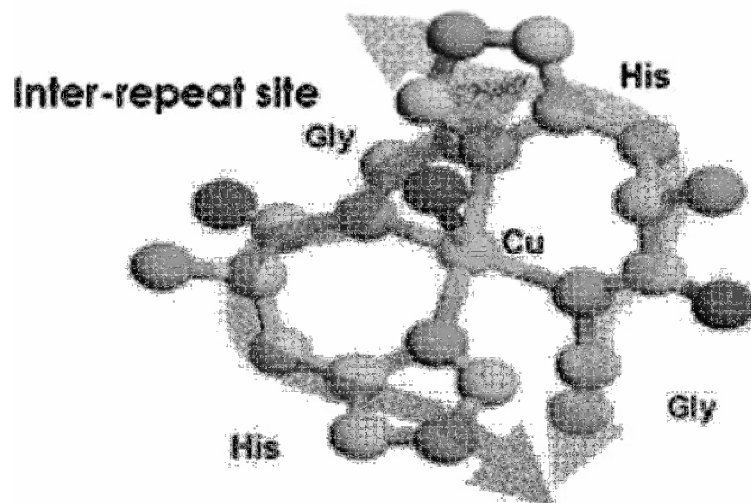
Figure 7.12: Inter-repeat Cu^{2+} site where two octarepeat units which can belong to different molecules bind one Cu^{2+} ion (reproduced from (Morante et al., 2004))

The copper binding sites of human and chicken prion protein at pH 6.5 were independently analyzed and then compared using XAS (Redecke et al., 2005). The Cu^{2+} binding configuration of the octarepeat domain of hPrP was studied by means of PrP-derived peptides consisting of one, three and four successive copies of the octapeptide sequence. To avoid the presence of peptide-unbound copper, the Cu^{2+} concentration was chosen so that only 0.5 Cu^{2+} ions per binding site were available. The EXAFS spectrum of one octapeptide–Cu^{2+} complex at pH 6.5 differs from our measurement of the same complex at pH 7.15 (compare especially the peak at k = 6.5 $\AA^{-1}$ in their paper). These differences can be explained if one notes that EXAFS spectra were recorded in samples that differ on pH value. In regard to the complete octarepeat domain, their EXAFS spectra of the tetraoctapeptide with 2 Cu^{2+} equivalents at pH 6.5 are different to our EXAFS measurements of the hPrP(23–231). Particularly, the main differences are found where one expects contributions stemming from imidazole coordination. Nevertheless, the Cu^{2+} environment of the tetraoctapeptide and hPrP(23–231) can be different. It is known from literature that at

pH 6.5, the tetraoctapeptide binds Cu^{2+} with two different configurations (Aronoff-Spencer et al., 2000). Since they do not report to have checked for inhomogeneities in respect to species type (by means of e.g., EPR or mass spectroscopy), it is likely that their EXAFS spectra were taken in samples where at least, two Cu^{2+} configurations coexist.

Chattopadhyay have published a study based on a variety of EPR techniques such as X-band EPR, S-band EPR and three-pulse ESSEM (Chattopadhyay et al., 2005). At pH 7.4, a variety of PrP-derived peptides with different Cu^{2+} loads were investigated. Particularly, in the PrP(23–28, 57–91) where the fragment 23–28 was attached because it increases solubility, the Cu^{2+} concentration was varied from 0.25 to 6 Cu^{2+} equivalents per molecule. They found two to three distinct species type contributing simultaneously in the EPR spectra. At high Cu^{2+} occupancy, above 2.0 Cu^{2+} equivalents per molecule, the so-called component 1 dominates the EPR spectra, although a residual species referred to as component 2 is also present. At low Cu^{2+} occupancy, from 0.25 to 2 Cu^{2+} equivalents per molecule, they found that two species coexist, namely the already mentioned component 2 and component 3 which shows similar parameters to our species II.

Component 1 is interpreted as 3N-1O complex in agreement with our species I. In the model proposed for component 2 type, two Cu^{2+} ions are bound in the octarepeat region in such a fashion that each copper complex binds to the N_δ and the backbone amid nitrogen of a histidine residue. Two water molecules complete the square-planar 2N-2O configuration. In addition, they proposed as weakly bound fifth axial ligand the nitrogen of another imidazole. For component 3, it is assumed that the Cu^{2+} is coordinated by three nitrogen atoms of histidyl imidazoles and a water oxygen (which could also be a nitrogen atom of a fourth histidyl imidazole). The different components are shown in Figure 7.13.
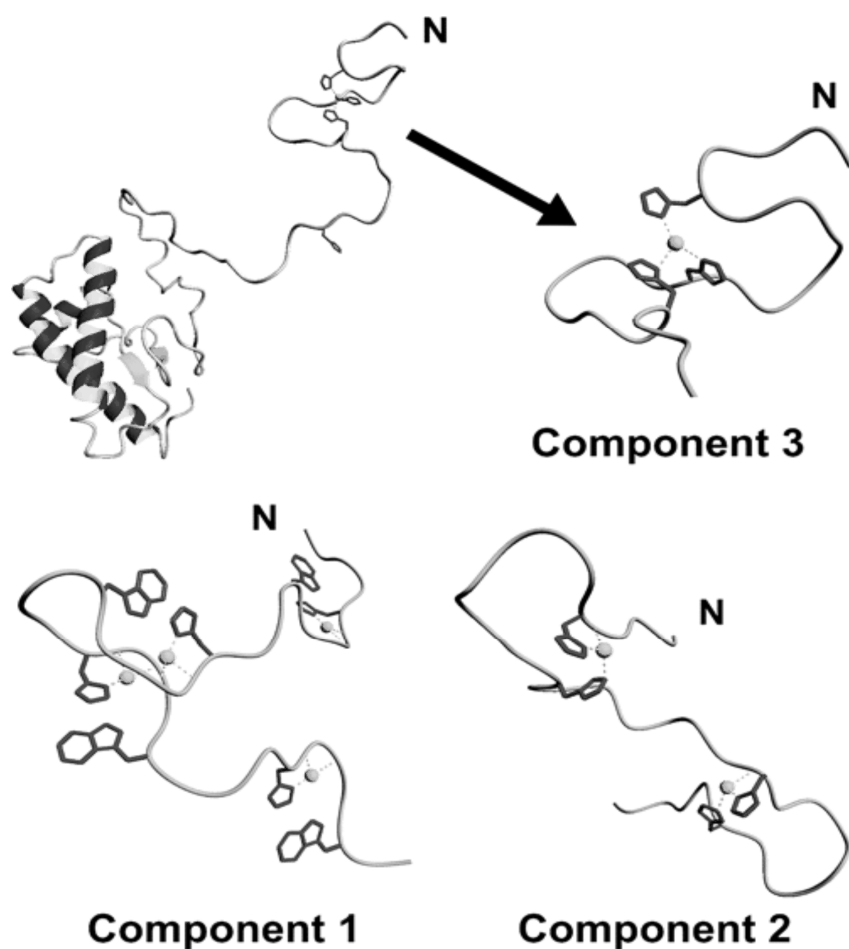
Figure 7.13: Different components found in PrP(23–28, 57–91) as a function of the Cu^{2+} load (reproduced from (Chattopadhyay et al., 2005)).

With respect to component 1 (our species I), our models are identical. At high Cu^{2+} occupancy where component 1 dominates, in addition, they found evidences of dipolar interaction between the Cu^{2+} ions. We also found evidences for dipolar coupling in two spectra of the tetraoctapeptide in MOPS buffer (see Figure 5.5 and 5.6, group B). However, although our species II shows nearly the same EPR parameters as component 3, they put forth a model that can not explain our experimental findings concerning species II in the context of the hPrP(23–231). In our model, we have two Cu^{2+} ions per tetraoctapeptide (two histidine residues), whereas they suggest that three histidine residues bind one Cu^{2+}. Obviously, this is in clear contradiction with our sample of hPrP with 2.7 Cu^{2+}.

Although in the course of our EPR investigation, we did not find a species corresponding to their component 2, we tried to adopt their model for an interpretation of species II due to the fact that the proposed model for component 2 explains the binding of two Cu^{2+} ions per tetraoctapeptide. We generated models consistent with the information given by Chattopadhyay (Chattopadhyay et al., 2005). XPLOR and its simulated annealing protocols were used to calculate models. However, the EXAFS spectra simulated from this model cannot fit with our experimental data. Particularly, the fifth ligand, the axially bound imidazole ring, is completely in disagreement with our spectrum. Given the model adopted from Chattopadhyay, Figure 7.14 shows the EXAFS simulation of the conformation with the minimum energy. Table 7.2 shows the first-ligand distances for this model. In this comparison, one should not forget that the model for component 2 was developed for a quite different sample.
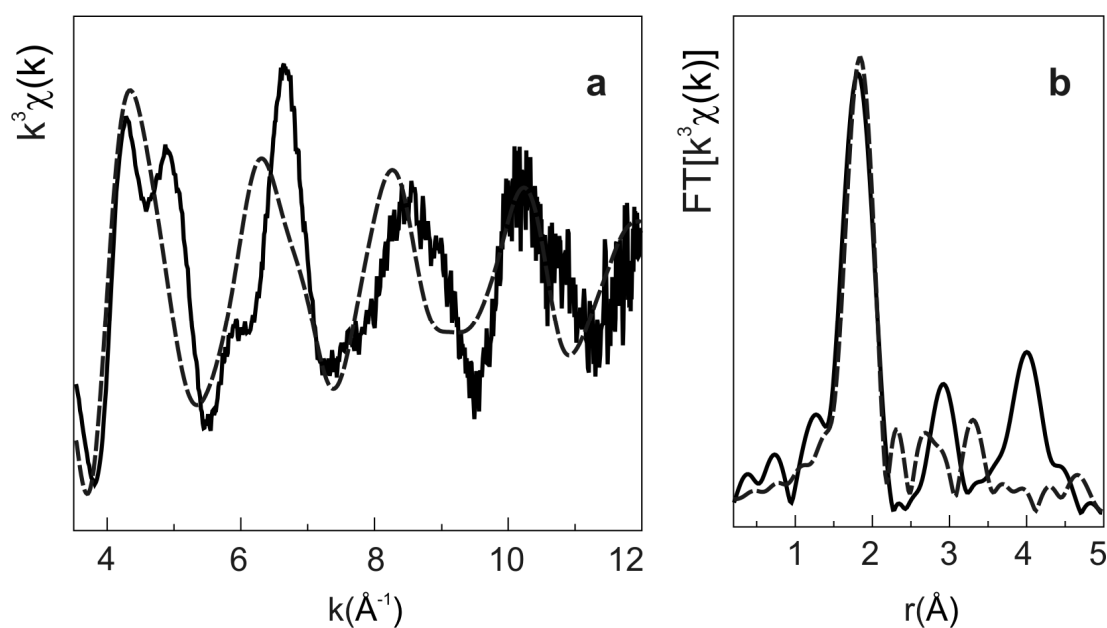
Figure 7.14: (a) k^3–weighted EXAFS spectra of the hPrP(23–231)/2.7Cu^{2+} complex; (b) Fourier transform. Black lines: experimental data. Broken lines: simulation of the model proposed by Chattopadhyay (Chattopadhyay et al., 2005).

Copper site 1		Copper site 2	
Ligands	Cu^{2+} - Ligand (Å)	Ligands	Cu^{2+} - Ligand (Å)
^{69}His N_δ	1.98	^{77}His N_δ	1.98
^{69}His NH	2.05	^{77}His NH	2.08
$H_2O(1)$ O	2.00	$H_2O(1)$ O	2.00
$H_2O(2)$ O	2.00	$H_2O(2)$ O	2.00
^{61}His N_δ	2.25	^{85}His N_δ	2.26

Table 7.2: Distances of the direct ligands of copper sites 1 and 2 in the simulated model proposed by Chattopadhyay (Chattopadhyay et al., 2005).

Recently and independently to the preciously discussed study, Wells has proposed multiple forms of Cu^{2+} coordination in the N-terminal domain of PrP depending upon the molecule/Cu^{2+} ratio as shown in Figure 7.15 (Wells et al., 2006b). Based on NMR, CD and fluorescence data of the tetraoctarepeat, PrP(57–91), in diverse buffer systems and with different Cu^{2+} loads, they basically proposed the same Cu^{2+} binding components that Chattopadhyay previously reported (Chattopadhyay et al., 2005). Since we already discussed these components with respect to our work, it is redundant to add further comments. In respect to the non-octarepeat binding place, they studied the PrP(91-115) with one and two Cu^{2+} equivalents with a similar program of experiments to that used for PrP(57–91). They found two Cu^{2+} coordinations depending on the Cu^{2+} load. When two Cu^{2+} ions are available, they suggest that each Cu^{2+} binds to either His96 or His111. The coordination is completed by deprotonated amide nitrogens. These sites are compatible with our data for species III, although we cannot clarify whether in our samples the Cu^{2+} center is coordinated by His96 or His111. We can even not exclude that both binding motifs are present. Since both Cu^{2+} sites (associated to His96 and His111) are very similar with respect to the first coordination shell, it could be that we have a mixture of them in our samples. At low Cu^{2+} occupancy, they found that both His96 and His111 participate in the Cu^{2+} coordination. Furthermore, they suggest that there might be more histidine residues from other molecules involved in the coordination. Obviously, this second Cu^{2+} binding mode for PrP(91-115) at low Cu^{2+} occupancy is completely inconsistent with our data for species III (mutant HG of MmPrP(23–231)/Cu^{2+}). Although again we have to emphasize that these samples are very

different in respect to their sequence context.
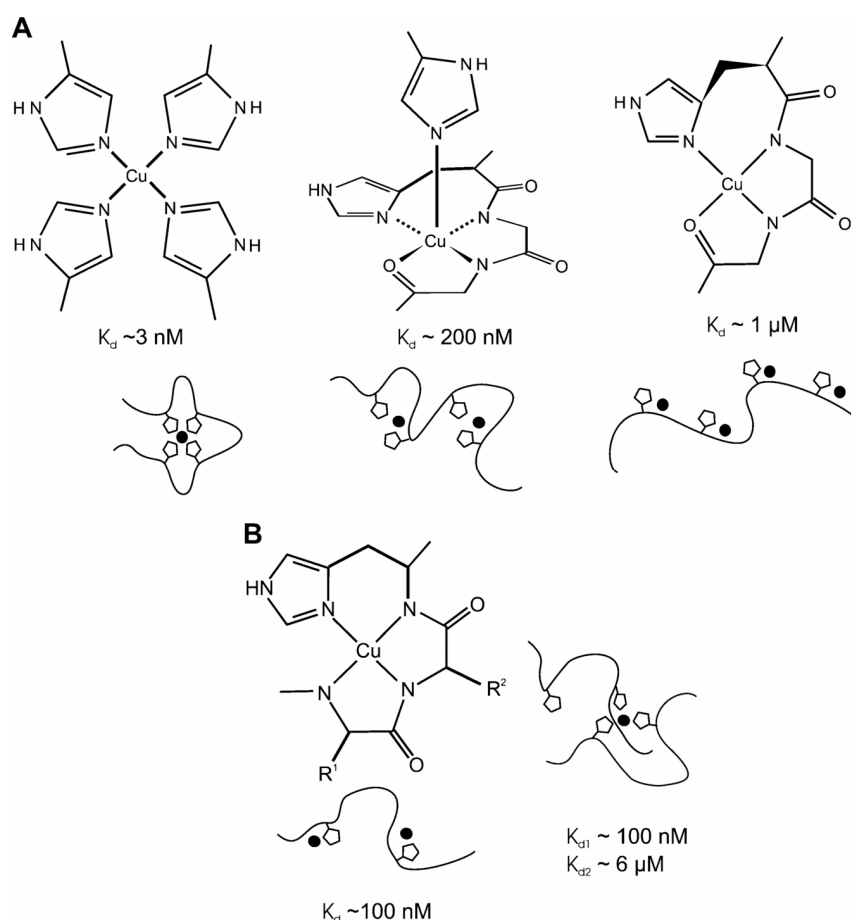
Figure 7.15: (A) Three Cu^{2+} coordination motifs within the octarepeat units depending upon Cu^{2+} concentration. (B) Two Cu^{2+} coordination motifs for PrP(91–115) (reproduced from (Wells et al., 2006b)).

In another recent study, Wells has reported a NMR investigation of the Cu^{2+} binding to recombinant hPrP(23–231) at pH 5.5 (Wells et al., 2006a). Two configurations are contemplated (Figure 7.16). At low Cu^{2+} occupancy (less that one Cu^{2+} per molecule), their data indicate that at least seven functional groups, namely the six histidines of the N-terminal domain and the N-terminal amine, contribute to coordinate a single Cu^{2+} ion. Since seven coordinating groups cannot all be simultaneously involved in the Cu^{2+} coordination (in proteins, Cu^{2+} is generally coordinated by three, four or five ligands), they proposed a rapidly ensemble of different coordination geometries, involving different combinations of the seven coordinating groups. The second coordination motif occurs when the molecule is

loaded with two Cu^{2+} ions. Then, the seven functional groups previously mentioned share the coordination of the two Cu^{2+} ions. They do not exclude that the second motif is also a rapidly exchanging ensemble of species with different coordination modes. This coordination types are clearly in disagreement with our data regarding the hPrP with different Cu^{2+} loads in either solution (pH 6.0) or precipitated forms (pH 6.0 and 7.0). Our EPR data are clearly attributable to species II. The described mixture of species cannot fit into our EPR data because such a species mixture would considerably broad the hyperfine splitting and definitely, the superhyperfine structure would not be resolved at all. Moreover, we were able to locate the Cu^{2+} binding site of hPrP by comparison with several PrP-derived peptides and the mutant HG of MmPrP. We can exclude the participation of either His96 or His111 in the Cu^{2+} coordination in hPrP.
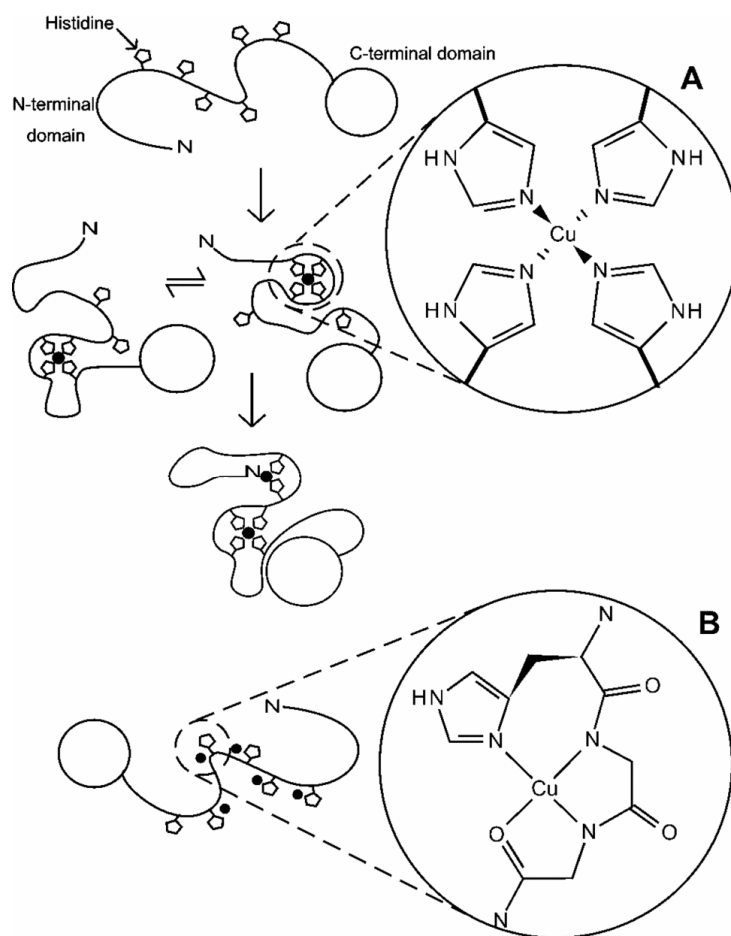
Figure 7.16: Illustration of two alternative modes of Cu^{2+} coordination in the full-length PrP at pH 5.5 (reproduced from (Wells et al., 2006a)).

In the course of this work, we have demonstrated that using complementary experimental techniques together with MD simulations can be very useful in resolving uncertainties that otherwise may not be readily apparent from the results of a single method. It was possible to validate one model that completely agreed with the experimental data. In the context of the recombinant hPrP(23–231), using EPR, ENDOR, and EXAFS, combined with MD simulations, we were able to infer a reliable model for the copper binding place of PrP which, as already disccused, differs from other models previously proposed.

Literature

Arnesano, F., Banci, L., Bertini, I., Felli, I.C., Luchinat, C. and Thompsett, A.R. (2003a) A strategy for the NMR characterization of type II copper(II) proteins:The case of the copper trafficking protein CopC from Pseudomonas Syringae. *J. Am. Chem. Soc*, **125**, 7200- 7208.

Arnesano, F., Banci, L., Bertini, I., Mangani, S. and Thompsett, A.R. (2003b) A redox switch in CopC: an intriguing copper trafficking protein that binds copper (I) and copper (II) at different sites. *PNAS*, **100**, 3814-3819.

Aronoff-Spencer, E., Burns, C.S., Avdievich, N.I., Gerfen, G.J., Peisach, J., Antholine, W.E., Ball, H.L., Cohen, F.E., Prusiner, S.B. and Millhauser, G.L. (2000) Identification of the Cu^{2+} binding sites in the N-terminal domain of the prion protein by EPR and CD spectroscopy. *Biochemistry*, **39**, 13760-13771.

Binsted, N., Strange, R.W. and Hasnain, S.S. (1992) Constrained and restrained refinement in EXAFS data analysis with curved-wave theory. *Biochemistry*, **31**, 12117-12125.

Brown, D.R. (1999) Prion protein expression aids cellular uptake and veratridine-induced release of copper. *Journal of Neuroscience Research*, **58**, 717-725.

Brown, D.R., Qin, K., Herms, J.W., Madlung, A., Manson, J., Strome, R., Fraser, P.E., Kruck, T., Bohlen, A.v., Schulz-Schaeffer, W., Giese, A., Westaway, D. and Kretzschmar, H. (1997) The cellular prion protein binds copper i*n vivo*. *Nature*, **390**, 684-687.

Brown, D.R., Wong, B.-S., Hafiz, F., Clive, C., Haswell, S.J. and Jones, I.M. (1999) Normal prion protein has an activity like that of superoxide dismutase. *Biochem. J.*, **344**, 1-5.

Brünger, A.T. (1992) X-PLOR Version 3.1. *The Howard Hughes Med. Inst., Dep.*

Molecular Biophys.and Biochem.

Büeler, H., Fischer, M., Lang, Y., Bluethmann, H., Lipp, H.-P., Dearmond, S.J., Prusiner, S.B., Aguet, M. and Weissmann, C. (1992) Normal development and behaviour of mice lacking the neuronal cell-surface PrP protein. *Nature*, **356**, 577-582.

Burns, C.S., Aronoff-Spencer, E., Dunham, C.M., Lario, P., Avdievich, N.I., Antholine, W.E., Olmstead, M.M., Vrielink, A., Gerfen, G.J., Peisach, J., Scott, W.F. and Millhauser, G.L. (2002) Molecular features of the copper binding sites in the octarepeat domain of the prion protein. *Biochemistry*, **41**, 3991-4001.

Burns, C.S., Aronoff-Spencer, E., Legname, G., Prusiner, S.B., Antholine, W.E., Gerfen, G.J., Peisach, J. and Millhauser, G.L. (2003) Copper coordination in the full-length, recombinant prion protein. *Biochemistry*, **42**, 6794-6803.

Cereghetti, G.M., Schweiger, A., Glockshuber, R. and Van Doorslaer, S. (2001) Electron paramagnetic resonance evidence for binding of Cu^{2+} to the C-terminal domain of the murine prion protein. *Biophysical Journal*, **81**, 516-525.

Chattopadhyay, M., Walter, E.D., Newell, D.J., Jackson, P.J., Aronoff-Spencer, E., Peisach, J., Gerfen, G.J., Benett, B., Antholine, W.E. and Millhauser, G.L. (2005) The octarepeat domain of the prion proteins binds Cu(II) with three distinct coordination modes at pH 7.4. *J Am Chem Soc*, **127**, 12647-12656.

Cohen, F.E., Pan, K.M., Huang, Z., Baldwin, M., Fletterick, R.J. and Prusiner, S.B. (1994) Structural clues to prions replication. *Science*, **264**, 530-531.

Collinge, J., Whittington, M.A., Sidle, K.C., Smith, C.J., Palmers, M.S., Clarke, A.R. and Jefferys, J.G. (1994) Prion protein is necessary for normal synaptic function. *Nature*, **370**, 295-297.

Dickinson, A.G. and Outram, G.W. (1988) Genetic aspects of unconventional virus infections: the basis of the virino hypothesis. *Ciba Found Symp.*, **135**, 63-83.

Diringer, H., Beekes, M. and Oberdieck, U. (1994) The nature of the scrapie agent: the virus theory. *Ann. N. Y. Acad. Sci.*, **724**, 246-258.

Donne, D.G., Viles, J.H., Groth, D., Mehlhorn, I., James, T.L., Cohen, F.E., Prusiner, S.B., Wright, P.E. and Dyson, H.J. (1997) Structure of the recombinant full-lengh hamster prion protein PrP(29-231): the N terminus is highly flexible. *Proc. Nat. Ac. Sci (USA)*, **94**, 13452-13457.

Flechsig, E., Shmerling, D., Hegyi, I., Raeber, A.J., Fischer, M., Cozzio, a., von Mering, C., Aguzzi, A. and Weissmann, C. (2000) Prion protein devoid of the octapeptide repeat region restores susceptibility to scrapie in PrP knockout mice. *Neuron*, **27**, 399-408.

Giese, A., Levin, J., Bertsch, U. and Kretzschmar, H. (2004) Effect of metal ions on de novo aggregation of full-length prion protein. *Biochemical and Biophysical Research Communications*, **320**, 1240-1246.

Goldfarb, L.G., Brown, P., Cervenakova, L. and Carleton Gajdusek, D. (1994) Genetic analysis of Creutzfeldt-Jakob disease and related disorders. *Phil. Trans. R. Soc. Lond. B*, **343**, 379-384.

Goñi, F., Knudsen, E., Schreiber, F., Scholtzova, H., Pankiewicz, J., Carp, R., Meeker, H.C., Rubenstein, R., Brown, D.R., Sy, M.-S., Chabalgoity, J.A., Sigurdsson, E.M. and Wisniewski. (2005) Mucosal vaccination delays or prevents prion infection via an oral route. *Neuroscience*, **133**, 413-421.

Griffith, J.S. (1967) Self-replication and scrapie. *Nature*, **215**, 1043-1044.

Hasnain, S.S., Murphy, L.M., Strange, R.W., Grossmann, J.G., Clarke, A.R., Jackson, G.S. and Collinge, J. (2001) XAFS study of the high-affinity copper-binding site of human PrP$^{91-231}$ and its low-resolution structure in solution. *J. Mol. Biol.*, **311**, 467-473.

Hornshaw, M.P., McDermott, J.R. and Candy, J.M. (1995a) Copper binding to the N-terminal tandem repeat regions of mammalian and avian prion protein. *Biochemical and Biophysical Research Communications*, **207**, 621-629.

Hornshaw, M.P., McDermott, J.R., Candy, J.M. and Lakey, J.H. (1995b) Copper binding to the N-terminal tandem repeat region of mammalian and avian prion protein: structural studies using synthetic peptides. *Biochem. Biophys. Res. Comm.*,

214, 993-999.

Hurst, G.C., Henderson, T.A. and Kreilick, R.W. (1985) Angle-selected ENDOR spectroscopy. 1. Theoretical interpretation of ENDOR shifts from randomly orientated transition-metal complexes. *J Am Chem Soc*, **107**, 7294-7299.

Jackson, G.S., Murray, I., Hosszu, L.L.P., Gibbs, N., Waltho, J.P., Clarke, A.R. and Collinge, J. (2001) Location and properties of metal-binding sites on the human prion protein. *Proc. Nat. Ac. Sci (USA)*, **98**, 8531-8535.

Jarrett, J.T. and Lansbury, P.J. (1993) Seeding "one-dimensional crystallization" of amyloid: a pathogenic mechanism in alzheimer's disease and scrapie? *Cell*, **73**, 1055-1058.

Jones, C.E., Abdelraheim, S.R., Brown, D.R. and Viles, J.H. (2004) Preferential Cu^{2+} coordination by His^{96} and His^{111} induces β-sheet formation in the unstructured amyloidogenic region of the prion protein. *The Journal of Biological Chemistry*, **279**, 32018-32027.

Katterle, B., Gvozdev, R.I., Abudu, N., Ljones, T. and Andersson, K.K. (2002) A continuous-wave electron-nuclear double resonance (X-band) study of the Cu^{2+} sites of particulate methane mono-oxygenase of *Methylococcus capsulatus* (strain M) in membrane and pure dopamine β-mono-oxygenase of the adrenal medulla. *Biochem. J.*, **363**, 677-686.

King, C.-Y. and Diaz-Avalos, R. (2004) Protein-only transmission of three yeast prion strains. *Nature*, **428**, 319-.

Knaus, K.J., Morillas, M., Swietnicki, W., Malone, M., Surewicz, W.K. and Yee, V.C. (2001) Crystal structure of the human prion protein reveals a mechanism for oligomerization. *Nature Struct. Biol.*, **8**, 770-774.

Kramer, M.L., Kratzin, H.D., Schmidt, B., Römer, A., Windl, O., Liemann, S., Hornemann, S. and Kretzschmar, H. (2001) Prion protein binds copper within the physiological concentration range. *The Journal of Biological Chemistry*, **276**, 16711-16719.

Lemos, S.S., Collins, M.L.P., Eaton, S.S., Eaton, G.R. and Antholine, W.E. (2000)

Comparison of EPR-visible Cu^{2+} sites in pMMO from *Methylococcus capsulatus* (Bath) and *Methylomicrobium album* BG8. *Biophysical Journal*, **79**, 1085-1094.

Liemann, S. and Glockshuber, R. (1999) Influence of amino acid substitutions related to inherited human prion diseases on the thermodynamic stability of the cellular prion protein. *Biochemistry*, **38**, 3258-3267.

Liu, H., Farr-Jones, S., Ulyanov, N.B., Llinas, M., Marqusee, S., Groth, D., Cohen, F.E., Prusiner, S.B. and James, T.L. (1999) Solution structure of Syrian hamster protein rPrP(90-231). *Biochemistry*, **38**, 5362-5377.

López García, F., Zahn, R., Riek, R. and Wüthrich, K. (2000) NMR structure of the bovine prion protein. *Proc. Nat. Ac. Sci (USA)*, **97**, 8334-8339.

MacKerell Jr., A.D., Bashford, D., Bellott, M., Dunbrack Jr., R.L., Evanseck, J., Field, M.J., Fischer, S., Gao, J., Guo, H., Ha, S., , Joseph, D., Kuchnir, L., Kuczera, K., Lau, F.T.K., Mattos, C., Michnick, S., Ngo, T., Nguyen, D.T., Prodhom, B., Reiher, I., W. E.,, Roux, B., Schlenkrich, M., Smith, J., Stote, R., Straub, J., Watanabe, M., Wiorkiewicz-Kuczera, J., Y., D., and Karplus, M. (1998) All-atom empirical potential for molecular modeling and dynamics studies of proteins. *J. Phys. Chem.*, **102**, 3586-3616.

Mentler, M., Grantner, K., Weiss, A., Fiori, S., Fiorino, F., Renner, C., Meyer-Klaucke, W., Moroder, L., Tavan, P., Kretzschmar, H. and Parak, F. (2003) Refined structure of prion protein octapeptide repeat/Cu(II) complex in aqueous solution. *in preparation*.

Mentler, M., Weiss, A., Grantner, K., Del Pino, P., Deluca, D., Fiori, S., Renner, C., Meyer-Klaucke, W., Moroder, L., Bertsch, U., Kretzschmar, H.A., Tavan, P. and Parak, F.G. (2005) A new method to determine the structure of the metal environment in metalloproteins: investigation of the prion octapeptide repeat Cu^{2+} -complex. *Europ. Biophysics Journal*, **34**, 97-112.

Miura, T., Sasaki, S., Toyama, A. and Takeuchi, H. (2005) Copper reduction by the octapeptide repeat region of prion protein: pH dependence and implications in cellular copper uptake. *Biochemistry*, **44**, 8712-8720.

Morante, S., González-Iglesias, R., Potrich, C., Meneghini, C., Meyer-Klaucke, W., Menestrina, G. and Gasset, M. (2004) Inter- and intra-octarepeat Cu(II) site geometries in the prion protein: implications in Cu(II) binding cooperativity and Cu(II)-mediated assemblies. *The Journal of Biological Chemistry*, **279**, 11753-11759.

Mouillet-Richard, S., Ermonval, M., Chebassier, C., Laplanche, J.L., Lehmann, S., Launay, J.M. and Kellermann, O. (2000) Signal transduction through prion protein. *Science*, **289**, 1925-1928.

Muramoto, T., Scott, M., Cohen, F.E. and Prusiner, S.B. (1996) Recombinant scrapie-like prion protein of 106 amino acids is soluble. *Proc. Nat Acad. Sciences USA*, **93**, 15457-15462.

Murphy, D.M. and Farley, R.D. (2006) Principles and applications of ENDOR spectroscopy for structure determination in solution and disordered matrices. *Chem. Soc. Rev.*, **35**, 249-268.

Nicholl, D., Windl, O., de Silva, R., Sawcer, S. and Dempster, J.W. (1995) Inherited Creutzfeldt-Jakob disease in a British family associated with a novel 144 base pair insertion of the prion protein gene. *J. Neurol. Neurosurg. Psychiatry*, **58**, 65-69.

Nolting, H.F. and Hermes, C. (1992) Documentation for the EMBL EXAFS data analysis and evaluation program package, EXPROG, release 1.0. EMBL. Hamburg.

Peisach, J. and Blumberg, W.E. (1974) Structural implications derived from the analysis of electron paramagnetic resonance spectra of natural and artificial copper proteins. *Archives of Biochemistry and Biophysics*, **165**, 691-708.

Pettifer, R.F. and Hermes, C. (1985) Absolute energy calibration of X-ray radiation from synchrotron sources. *J. Appl. Crystallogr.*, **18**, 404-412.

Prusiner, S.B. (1982) Novel proteinaceous infectious particles cause scrapie. *Science*, **216**, 136-144.

Prusiner, S.B. (1996) Molecular biology and pathogenesis of prion diseases. *Trends Biochem. Sci.*, **21**, 482-487.

Prusiner, S.B. (1997) Prion diseases and the BSE crisis. *Science*, **278**, 245-251.

Rachidi, W., Vilette, D., Guiraud, P., Arlotto, M., Riondel, J., Laude, H., Lehmann, S. and Favier, A. (2003) Expression of prion protein increases cellular copper binding and antioxidant enzyme activities but not copper delivery. *The Journal of Biological Chemistry*, **278**, 9064-9072.

Redecke, L., Meyer-Klaucke, W., Koker, M., Clos, J., Georgieva, D., Genov, N., Echner, H., Kalbacher, H., Perbandt, M., Bredehorst, R., Voelter, W. and Betzel, C. (2005) Comparative analysis of the human and chicken prion protein copper binding regions at pH 6.5. *The Journal of Biological Chemistry*, **14**, 13987-13992.

Rehr, J.J. and Albers, R.C. (1990) Scattering-matrix formulation of curved-wave multiple-scattering theory: Application to x-ray-absorption fine structure. *Phys. Rev. B*, **41**, 8139-8149.

Renner, C., Fiori, S., Fiorino, F., Landgraf, D., Deluca, D., Mentler, M., Grantner, K., Parak, F.G., Kretzschmar, H. and Moroder, L. (2004) Micellar environments induce structuring of the N-terminal tail of the prion protein. *Biopolymers*, **73**, 421-433.

Riek, R., Hornemann, S., Wider, G., Glockshuber, R. and Wüthrich, K. (1997) NMR characterization of the full-length recombinant murine prion protein, *m*PrP(23-231). *FEBS Letters*, **413**, 282-288.

Sayers, D.E., Stern, E.A. and Lytle, F.W. (1971) New technique for investigating noncrystalline structures: Fourier analysis of the EXAFS. *Phys. Rev. Lett.*, **27**, 1204-1207.

Scholl, H.-J. and Hüttermann, J. (1992) ESR and ENDOR of Cu(II) complexes with nitrogen donors: probing parameters for prosthetic group modeling of superoxide dismutase. *The Journal of Physical Chemistry*, **96**, 9684-9691.

Skworc, K.H., Windl, O., Schulz-Schaeffer, W.J., Giese, A., Bergk, J., Nägele, A., Vieregge, P., Zerr, I., Poser, S. and Kretzschmar, H.A. (1999) Familial Creutzfeldt-Jakob disease with a novel 120-bp insertion in the prion protein gene. *Annals of Neurology*, **46**, 693-700.

Stöckel, J., Safar, J., Wallace, A.C., Cohen, F.E. and Prusiner, S.B. (1998) Prion protein selectively binds copper(II) ions. *Biochemistry*, **37**, 7185-7193.

Tanaka, M., Chien, P., Naber, N., Cooke, R. and Weissman, J.S. (2004) Conformational variations in an infectious protein determine prion strain differences. *Nature*, **428**, 323-.

Valensin, D., Luczkowski, M., Mancini, F.M., Legowska, A., Gaggelli, E., Valensin, G., Rolka, K. and Kozlowski, H. (2004) The dimeric and tetrameric octarepeat fragments of prion protein behave differently to its monomeric unit. *Dalton Trans.*, 1284-1293.

Viles, J.H., Cohen, F.E., Prusiner, S.B., Goodin, D.B. and Wright, P.E. (1999) Copper binding to the prion protein: Structural implications of four identical cooperative binding sites. *Proc. Natl. Acad. Sci. USA*, **96**, 2042-2047.

Weissmann, C. (1999) Molecular genetics of transmissible spongiform encephalopathies. *The Journal of Biological Chemistry*, **274**, 3-6.

Wells, M.A., Jackson, G.S., Jones, S., Hosszu, L.L.P., Craven, C.J., Clarke, A.R., Collinge, J. and Waltho, J.P. (2006a) A reassessment of copper(II) binding in the full-length prion protein. *Biochem. J.*, **399**, 435-444.

Wells, M.A., Jelinska, C., Hosszu, L.L.P., Craven, C.J., Clarke, A.R., Collinge, J., Waltho, J.P. and Jackson, G.S. (2006b) Multiple forms of copper (II) coordination occur throughout the disordered N-terminal region of the prion protein at pH 7.4. *Biochemical Journal*, **400**, 501-510.

Wertz, J.E. and Bolton, J.R. (1972) *Electron spin resonance: elementary theory and practical applications*. McGraw-Hill Book Company.

Wille, H., Michelitsch, M.D., Guénebaut, V., Supattapone, S., Serban, A., Cohen, F.E., Agard, D.A. and Prusiner, S.B. (2002) Structural studies of the scrapie prion protein by electron crystallography. *PNAS*, **99**, 3563-3568.

Windl, O., Dempster, M., Estibeiro, J.P., Lathe, R., de Silva, R., Esmonde, T., Will, R., Springbett, A., Campbell, T.A., Sidle, K.C., Palmer, M.S. and Collinge, J. (1996) Genetic basis of Creutzfeld-Jakob disease in the United Kingdom: a systematic

analysis of predisposing mutations and allelic variation in the PRNP gene. *Human Genetics*, **98**, 259-264.

Yuan, H., Collins, M.L.P. and Antholine, W.E. (1999) Type 2 Cu^{2+} in pMMO from *Methylomicrobium album* BG8. *Biophysical Journal*, **76**, 2223-2229.

Zahn, R. (2003) The octapeptide repeats in mammalian prion protein constitute a pH-dependent folding and aggregation site. *J. Mol. Biol.*, **334**, 477-488.

Zahn, R., Liu, A., Lührs, T., Riek, R., Schroeter von, C., Lopez Garcia, F., Billeter, M., Calzolai, L., Wider, G. and Wüthrich, K. (2000) NMR solution structure of the human prion protein. *Proc.Natl. Acad. Sci. USA*, **97**.

Apendix A: Figures

122

124

126

Apendix B: Tables

Publications

Parts of this work were published in the following articles:

- Mentler, M., Weiss, A., Grantner, K., <u>Del Pino, P.</u>, Deluca, D., Fiori, S., Renner, C., Meyer-Klaucke, W., Moroder, L., Bertsch, U., Kretzschmar, H.A., Tavan, P. and Parak, F.G. (2005) A new method to determine the structure of the metal environment in metalloproteins: investigation of the prion octapeptide repeat Cu^{2+} -complex. *European Biophysics Journal*, **34**, 97-112.

- <u>Del Pino, P.</u>, Weiss, A., Bertsch, U., Renner, C., Mentler, M., Grantner, K., Fiorino, F., Meyer-Klaucke, W., Moroder, L., Kretzschmar, H.A. and Parak, F.G. (2007) The configuration of the Cu^{2+} binding region in full-length human prion protein. *European Biophys Journal,* accepted [Epub ahead of print].

- Weiss, A., <u>Del Pino, P.</u>, Bertsch, U., Renner, C., Mentler, M., Grantner, K., Moroder, L., Kretzschmar, H.A. and Parak, F.G. (2007) The configuration of the Cu^{2+} binding region in full-length human prion protein compared with the isolated Octapeptid. *Veterinary Microbiology (Special Issue),* accepted.

Acknowledgment